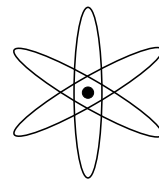


# Electrodisintegration of the Deuteron in Effective Field Theory

diploma thesis by  
STEFAN CHRISTLMEIER

*December 2004*

Technische Universität München  
Physik-Department  
T39 (Prof. Dr. Wolfram Weise)





# Contents

<b>1</b>	<b>Introduction</b>	<b>3</b>
1.1	Effective Field Theories . . . . .	3
1.1.1	General Aspects . . . . .	3
1.1.2	Application to Nuclear Physics . . . . .	4
1.2	About this Work . . . . .	5
<b>2</b>	<b>Theoretical Framework: EFT(<math>\not{\pi}</math>)</b>	<b>7</b>
2.1	Range of Applicability . . . . .	7
2.2	Nucleon-Nucleon Scattering . . . . .	8
2.2.1	Effective Range Theory . . . . .	8
2.2.2	EFT( $\not{\pi}$ ): The Problem of Large Length Scales . . . . .	10
2.2.3	Dibaryon Fields . . . . .	12
2.3	Lagrangian and Power Counting . . . . .	15
<b>3</b>	<b>Applications</b>	<b>18</b>
3.1	Electric Form Factors of the Deuteron . . . . .	18
3.1.1	Elastic Electron-Deuteron Scattering . . . . .	18
3.1.2	Charge Form Factor . . . . .	19
3.1.3	$SD$ Mixing and Quadrupole Form Factor . . . . .	21
3.2	Radiative Capture $np \rightarrow d\gamma$ . . . . .	24
3.2.1	Magnetic Transitions . . . . .	24
3.2.2	Electric Transitions . . . . .	26
3.2.3	Comparison of Individual Contributions . . . . .	27
<b>4</b>	<b>Deuteron-Electrodisintegration</b>	<b>28</b>
4.1	Kinematics and Formalism . . . . .	28
4.1.1	Kinematics . . . . .	28
4.1.2	Formalism . . . . .	32
4.2	Electric Transitions at LO . . . . .	33
4.3	Electric Transitions at NNLO: $SD$ Mixing . . . . .	36
4.4	Magnetic Transitions up to NLO . . . . .	40

4.5	Other Possible Contributions . . . . .	43
<b>5</b>	<b>Results and Discussion</b>	<b>47</b>
5.1	Triple-Differential Cross Section . . . . .	47
5.2	Decomposition into Different Structure Functions . . . . .	55
5.3	Proposed Experiment at Threshold . . . . .	64
<b>6</b>	<b>Summary</b>	<b>69</b>
<b>A</b>	<b>Feynman Rules</b>	<b>71</b>
<b>B</b>	<b>Projection Operators</b>	<b>73</b>
<b>C</b>	<b>Kinematics for the Triple-Differential Cross Section</b>	<b>75</b>
<b>D</b>	<b>Useful Integrals</b>	<b>77</b>

# Chapter 1

## Introduction

### 1.1 Effective Field Theories

#### 1.1.1 General Aspects

In this work, a nuclear process – electrodisintegration of the deuteron – is examined within the framework of Effective Field Theory (EFT). We begin with a short introduction of effective field theories in general and their application to nuclear physics, based on Refs. [1], [2] and [3].

In physics, the situation often arises that there are two (or more) separate energy scales involved in a process. If one is only interested in low-energy observables and the physics at the high-energy (“heavy”) scale is unknown or needlessly complicated, it is useful to construct an equivalent theory written only in terms of the “light” degrees of freedom. In a quantum field theory, this can be formally expressed by looking at the path integral of the full theory

$$Z = \int \mathcal{D}\phi \mathcal{D}\Phi \exp i \int d^4x \mathcal{L}(\phi, \Phi), \quad (1.1)$$

where  $\phi$  and  $\Phi$  represent the “light” and “heavy” fields, respectively. If the “heavy” degrees of freedom are integrated out, we are left with

$$Z = \int \mathcal{D}\phi \exp i \int d^4x \mathcal{L}_{\text{eff}}(\phi). \quad (1.2)$$

The effective Lagrangean  $\mathcal{L}_{\text{eff}}$  comprises only derivatives and powers of  $\phi$  and, in general, an infinite number of constants that incorporate the effects of the “heavy” scale. Such an *effective* field theory still has the symmetries of the underlying theory. Therefore, we can construct  $\mathcal{L}_{\text{eff}}$  also if the integration over  $\Phi$  cannot be explicitly performed: In this case it is written as the most general local Lagrangean that is consistent with these symmetries.

The effective theory can be applied if the two scales associated with  $\Phi$  and  $\phi$ , denoted by  $\Lambda$  and  $Q$  respectively, are widely separated. Then the low-energy observables can be expanded in powers of the small parameter  $Q/\Lambda$ . The low-energy scale  $Q$  is given by typical momenta of the “light” fields, whereas the high-energy scale  $\Lambda$  is set by the masses of the particles that have been integrated out. Only a finite number of parameters enters at a given order in  $Q/\Lambda$ , and these have to be determined by experimental data, or from the underlying theory, whenever possible. This expansion permits an estimation of the theoretical error when leaving out contributions beyond a given order. A critical prerequisite for this estimate is the *naturalness assumption*: The sizes of the coefficients that encode short-distance physics are assumed to be “natural”, i. e. set by the scale  $\Lambda$ . (There are, however, exceptions to this, and we will have to deal with an example in Chapter 2.)

The physical reason why the effective theory works for energies that are much smaller than  $\Lambda$  is that phenomena at low energies (or long wavelength) cannot probe details of the high-energy (or short-distance) physics. There are many examples for such theories. Perhaps the most successful theory in physics, QED, is actually an effective field theory of some unknown fundamental theory. Superconductivity can be described “effectively” by the Ginzburg-Landau Hamiltonian instead of the more complicated BCS theory. A classical effective theory of the scattering of light from atoms (Rayleigh-Scattering) can be constructed. Fermi’s theory of weak interactions is valid at energy scales much below the  $W$  and  $Z$  boson masses; these mediating particles (whose masses set the scale  $\Lambda$ ) cannot be resolved at low energies of order  $Q \ll \Lambda$  and can thus be integrated out; at leading order in  $Q/\Lambda$ , only a contact interaction proportional to one constant (the Fermi constant) remains. This latter example has the closest similarity to the nuclear effective theory used in this work. In the following, we briefly motivate why and how these ideas are applied to nuclear physics.

### 1.1.2 Application to Nuclear Physics

Interactions between protons and neutrons are governed by the strong nuclear force. Quantum Chromodynamics (QCD) describes these interactions in terms of fundamental particles – quarks and gluons. These are asymptotically free in the high-energy regime, which means that the coupling constant  $g_s$  is small at extremely short distances ( $< 0.1$  fm) and perturbation theory can be applied in this regime. However, in a nucleus, the quarks are far from being asymptotically free, and QCD is non-perturbative (with respect to an expansion in  $g_s$ ). Moreover, the small nuclear binding energies result from detailed cancellations between much larger contributions. It is therefore not

surprising that the structure of even the smallest nuclei is out of reach for full QCD calculations.

In spite of this, many phenomena in nuclear physics have been successfully described by the use of models. In particular, deuteron-electrodisintegration has been examined within a potential model calculation, and we will refer to those results in our work. There are, however, some dissatisfying aspects of such models, e. g. their ad hoc nature (i. e. they are not derived from basic principles such as the symmetries of QCD), the large number of parameters involved, ambiguities in treating off-shell effects, and particularly the difficulty of performing reliable error estimates.

This situation is apparently ideal for using effective field theory methods. In low-energy hadronic physics, quarks and gluons are evidently “ineffective” degrees of freedom. Restricting oneself to processes at energy scales below about 1 GeV, only pions and nucleons remain as active degrees of freedom. (Slow nucleons – despite of their large rest mass – are considered as low-energy degrees of freedom because energies are measured relative to the ground state with a given baryon number.) The corresponding theory is known as Chiral Effective Field Theory ( $\chi$ EFT), first developed in the mesonic sector as Chiral Perturbation Theory ( $\chi$ PT). Several versions of  $\chi$ EFT have been applied very successfully in the one- and two-nucleon sectors (see e. g. [4]). The present work is based on a theory without pions which is valid for even lower energies (introduced in the second Chapter). We demonstrate how such a theory applies to two-nucleon processes in an efficient way so that even analytic results can be derived for many observables.

## 1.2 About this Work

The deuteron, as the bound state of a proton and a neutron, is the simplest nucleus, playing the same fundamental role as the hydrogen atom in atomic physics. Any realistic model of NN-interaction must describe the two-nucleon system accurately. Its electromagnetic properties have been studied in great detail both theoretically and experimentally – amongst others in photodisintegration (see [5] and [6] for reviews), and also in electrodisintegration ([7, 8, 9] and references there). The latter process has the advantage to allow an independent variation of energy and momentum transfer.

Most experiments have been performed at high energy transfers and are in good agreement with potential-model calculations. However, one experiment examined the triple-differential cross section for  $d(e, e'p)n$  at low momentum transfer ( $< 60$  MeV/c) and energies close to the breakup threshold, and in particular its decomposition into the contributions of different structure

functions [9]. For the longitudinal-transverse interference cross section, a discrepancy to theoretical predictions by about 30 % was discovered.

In this work, we study this process in the same energy regime within Pionless Effective Field Theory,  $EFT(\pi)$ . This theory is introduced in Chapter 2. After considering NN scattering, we present the Lagrangean relevant for deuteron-electrodisintegration and the power counting rules applied.

This Lagrangean has some unknown coefficients; these are fixed by matching to data in the third Chapter, where we show two applications of  $EFT(\pi)$ : Analytic expressions for the electric form factors of the deuteron and for the cross section of radiative neutron capture by the proton are reproduced. The amplitude for the latter process is very similar to the one for  $ed \rightarrow e'pn$ .

The fourth Chapter presents the calculations of the triple-differential cross section for deuteron-electrodisintegration. First, the necessary kinematic relations and the formalism are introduced, and then we calculate the amplitude for electric transitions up to next-to-next-to-leading order (NNLO), and for magnetic transitions up to NLO.

The results are discussed in Chapter 5. We compare them to a potential-model calculation and to the data mentioned above after pointing out some misconceptions regarding the frame of reference used in [9]. The triple-differential cross section and the contributions of different structure functions are considered.

Finally, a summary and outlook can be found in Chapter 6. The Feynman rules and other details of the calculation are presented in the Appendices.

# Chapter 2

## Theoretical Framework: EFT( $\not{\pi}$ )

In this Chapter, the tools for calculating two-nucleon processes that are examined later in this work are introduced. After specifying the energy regime in which our theory is applicable, we show how low-energy nucleon-nucleon scattering can be described within Pionless Effective Field Theory, denoted by EFT( $\not{\pi}$ ). Finally, interactions with external photons are included, and the power counting rules are summarized.

### 2.1 Range of Applicability

EFT( $\not{\pi}$ ) is a nuclear effective field theory similar to Chiral Effective Field Theory (mentioned in the Introduction). Its advantage is that two-nucleon processes at the lowest energies are easier to calculate. It is limited to processes where the energies and momenta of the scattering nucleons are much lower than  $m_\pi \approx 140$  MeV; in this case, even pions can be integrated out and only nucleons remain as effective degrees of freedom, interacting via contact interactions. This is because the typical Compton wave length of the nucleons is then much larger than the inverse pion mass ( $\approx 1.4$  fm)<sup>1</sup>, which means that the propagating pions cannot be resolved. In other words, even the longest-ranged part of the NN force, that due to one-pion exchange, appears short-ranged [1]. Then the NN potential can be approximated to be of zero range, represented by contact operators in the effective field theory.

In order to perform a sensible perturbative expansion, a small expansion parameter  $Q/\Lambda$  is required (as explained in the Introduction). In EFT( $\not{\pi}$ ),  $\Lambda$  is given by the pion mass and  $Q$  is the scale of the momenta of external nucleons – or photons, since EFT( $\not{\pi}$ ) can be applied to processes including

---

<sup>1</sup>We work in natural units, i. e.  $\hbar = c = 1$ .

external probes<sup>2</sup>, as long as the energy and momentum transferred by the latter are also lower than  $m_\pi$ . In our case, typical momenta are between 30 and 80 MeV; we even calculate cross sections at momenta larger than 100 MeV, although we are aware that this is not very much smaller than  $m_\pi$  and the expansion parameter comes close to unity. In spite of this, we still get sensible results at such high energies (see discussion at the end of Sect. 5.2).

## 2.2 Nucleon-Nucleon Scattering

### 2.2.1 Effective Range Theory

A theory which describes NN scattering in terms of a few parameters was developed more than 50 years ago: Effective Range Theory (ERT) [10] is a low-energy expansion of the scattering amplitude, valid for momenta less than the pion mass. First we repeat the basic features of this theory; then we show how EFT( $\pi$ ) is designed to reproduce ERT results in this sector (see [11] for a review); and in the next section we go beyond ERT by including external electromagnetic fields.

For the scattering of two nucleons in the  $^1S_0$  channel<sup>3</sup> – each with momentum  $p$  in the center-of-mass frame – the scattering matrix can be written as

$$S = e^{2i\delta} = 1 + \frac{2ip}{p \cot \delta - ip} = 1 + i \frac{pM}{2\pi} \mathcal{A}. \quad (2.1)$$

Here  $\delta$  is the S-wave phase shift which determines the asymptotic radial wave function, and  $M = 938.9$  MeV is the isospin-averaged nucleon mass. The analytic function  $p \cot \delta$  is real below the pion threshold  $p < m_\pi$  and can be expanded around  $p = 0$ , with a convergence radius of  $m_\pi/2$  (*effective range expansion*):

$$p \cot \delta = -\frac{1}{a_0} + \frac{1}{2}r_0p^2 + r_1p^4 + \dots \quad (2.2)$$

For proton-neutron scattering, the empirical values of the coefficients are:

$$a_0 = -23.71 \text{ fm}, \quad r_0 = 2.73 \text{ fm}, \quad r_1 = -0.48 \text{ fm}^3. \quad (2.3)$$

The shape parameter  $r_1$  is said to be of “natural size”, i. e. it is given by the range of one-pion exchange  $\sim 1/m_\pi$ . In contrast, the scattering length

---

<sup>2</sup>Only electromagnetic probes are considered in this work, but one can also study weak interactions within EFT( $\pi$ ) (see e. g. [31]).

<sup>3</sup>The notation is  $^{2S+1}L_J$ , with  $S$  the total spin of the NN system,  $L$  its orbital angular momentum and  $J$  its total angular momentum.

$a_0$  is much larger than  $1/m_\pi$ , and this causes a problem we will refer to in the next subsection. The effective range  $r_0$  is a borderline case: Numerically twice as large as  $1/m_\pi$ , it could still be regarded as natural, but in Sect. 2.2.3 we will argue that it is more accurate to assume  $r_0 \sim Q^{-1}$  where  $Q$  is the characteristic low-momentum scale.

Inserting (2.2) into (2.1) and neglecting the shape parameter and higher contributions, the amplitude is

$$i\mathcal{A}^{(1S_0)} = \frac{4\pi}{M} \frac{i}{-\frac{1}{a_0} + \frac{1}{2}r_0p^2 - ip}, \quad (2.4)$$

which will be reproduced in EFT( $\not{\pi}$ ) in the next Subsection.

In the  ${}^3S_1$  channel, the deuteron is present as a bound state of a proton and a neutron, i. e. the amplitude has a pole at  $p = i\gamma$ ; the deuteron binding energy is

$$B = 2.225 \text{ MeV}, \quad (2.5)$$

and the pole position is given by

$$\gamma \equiv \sqrt{MB} = 45.70 \text{ MeV}. \quad (2.6)$$

The quantity  $\gamma$  (sometimes called “binding momentum”) scales as  $Q$  and determines the size of the deuteron:  $1/\gamma \approx 4.3 \text{ fm}$ . This is significantly larger than  $1/m_\pi$ , which is a prerequisite for studying deuteron properties within EFT( $\not{\pi}$ ). Expanding  $p \cot \delta$  in the  ${}^3S_1$  channel around zero momentum would mean that the position of the deuteron pole is reached only perturbatively; it is therefore useful to make the effective range expansion around the pole:

$$p \cot \delta = -\gamma + \frac{1}{2}\rho_d(p^2 + \gamma^2) + w_2(p^2 + \gamma^2)^2 + \dots, \quad (2.7)$$

with

$$\rho_d = 1.764 \text{ fm}, \quad w_2 = 0.389 \text{ fm}. \quad (2.8)$$

This also corresponds to a large scattering length ( $\frac{1}{a({}^3S_1)} \approx \gamma - \frac{\rho_d}{2}\gamma^2$  from comparing (2.7) to (2.2)),  $a({}^3S_1) = 5.42 \text{ fm}$ . Combining (2.1) and (2.7) gives

$$i\mathcal{A}^{(3S_1)} = \frac{4\pi}{M} \frac{i}{-\gamma + \frac{1}{2}\rho_d(p^2 + \gamma^2) - ip}. \quad (2.9)$$

An additional complication in the spin-triplet channel arises from the fact that the NN interaction is not spherically symmetric (as first recognized when the deuteron quadrupole moment was measured [12]). This gives rise to a mixing of the  $S$ -wave- with a small  $D$ -wave component. We will return to this in Sect. 3.1.3.

### 2.2.2 EFT( $\not{k}$ ): The Problem of Large Length Scales

Now we show how the amplitude (2.4) is recovered at leading order (LO) in EFT( $\not{k}$ ), i. e. keeping only the first term in the  $Q$ -expansion. We saw that both in the  $^1S_0$  and in the  $^3S_1$  channels, the amplitude has a pole at unnaturally small momenta whose scale is not set by the range of pion exchange. This can only happen if there is a fine-tuning between long- and short-distance physics; since the effects of short-distance physics are encoded in the coefficients of the EFT, the location of the pole must be an input for EFT( $\not{k}$ ).

There are two equivalent formulations for EFT( $\not{k}$ ). In the next Subsection we introduce the formulation employed in this work, but first we sketch the original version, following mainly [11]; we neglect the effective range for the moment and concentrate on the impact of a large scattering length. Then the LO effective Lagrangean for the scattering of two non-relativistic nucleons reads<sup>4</sup>

$$\mathcal{L} = N^\dagger \left( i\partial_0 + \frac{\nabla^2}{2M} \right) N - C_0 (N^T P_a N)^\dagger (N^T P_a N) + \dots \quad (2.10)$$

Here,  $N = \begin{pmatrix} p \\ n \end{pmatrix}$  is a doublet of spin 1/2 fields representing the positive-frequency nucleon field,  $P_a = \frac{1}{\sqrt{8}} \sigma_2 \tau_2 \tau_a$  is the projector on the  $^1S_0$  channel (where  $\sigma$  and  $\tau$  are Pauli matrices acting on spin and isospin space, respectively, see App. B), and  $C_0$  is the parameter that contains all the information of short-distance physics and must be determined from empirical data. At higher orders, there would be four-nucleon vertices with derivatives of nucleon fields; each term containing an additional derivative is suppressed by one more power of  $p \sim Q$ . Relativistic corrections to the nucleon kinetic energy can also be included perturbatively in an expansion in  $Q/M$ .

The scattering amplitude that follows from (2.10) must describe a quasi-bound state at low energy. (In the  $^3S_1$  channel where there is a real bound state, the argument is the same.) The corresponding diagrams are depicted in Fig. 2.1: the tree-level graph and an infinite series of nucleon bubbles. Since a bound state can never arise at a finite order in perturbation theory, all diagrams in Fig. 2.1 should contribute at the same order. Summing up the infinite series gives the amplitude

$$i\mathcal{A} = -iC_0 - iC_0 I_0 C_0 - iC_0 I_0 C_0 I_0 C_0 + \dots = \frac{-i}{\frac{1}{C_0} - I_0} \quad (2.11)$$

---

<sup>4</sup>For simplicity we consider only the  $^1S_0$  channel here.

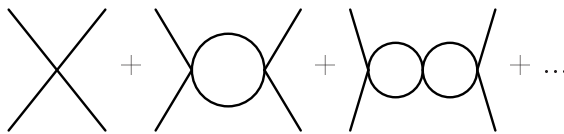


Figure 2.1: Diagrams contributing to the NN scattering amplitude.

The loop integral  $I_0$  is linearly divergent. It is conventionally calculated using dimensional regularization, since this scheme preserves Galilei-invariance, unlike e. g. cut-off regularization.  $I_0$  is therefore multiplied by  $(\frac{\mu}{2})^{3-D}$  so that its dimension stays the same in  $D$  space dimensions:<sup>5</sup>

$$\begin{aligned}
 I_0 &= -i \left(\frac{\mu}{2}\right)^{3-D} \int \frac{d^{(D+1)}l}{(2\pi)^{(D+1)}} \frac{i}{(l_0 - \frac{l^2}{2M} + i\epsilon)} \frac{i}{(E - l_0 - \frac{l^2}{2M} + i\epsilon)} \\
 &= \left(\frac{\mu}{2}\right)^{3-D} M \int \frac{d^D l}{(2\pi)^D} \frac{1}{p^2 - l^2 + i\epsilon} \\
 &= -\left(\frac{\mu}{2}\right)^{3-D} M \frac{i^D}{(2\pi)^D} i\pi^{D/2} \Gamma\left(\frac{2-D}{2}\right) (-p^2 - i\epsilon)^{\frac{D-2}{2}}. \quad (2.12)
 \end{aligned}$$

$E = \frac{\mathbf{p}^2}{M}$  is the total energy in the center-of-mass frame, while  $p = |\mathbf{p}|$  is the nucleon momentum. The infinitesimal imaginary part  $i\epsilon$  is required to shift the pole away from the real axis in the correct direction. Now it depends on the specific regularization scheme how this is evaluated further. In the usual  $\overline{\text{MS}}$  scheme, where only poles in  $D = 3$  dimensions are subtracted,  $I_0$  is independent of  $\mu$ . Inserting the result in (2.11) and matching to the ERT amplitude (2.4), we find that each loop in the bubble sum scales as  $C_0 I_0 \sim a_0 p$ . For a scattering length of natural size, each loop would thus be suppressed by one power of  $Q/\Lambda$ . But since  $1/a_0 = 8$  MeV, the series converges only for very low momenta  $p < 8$  MeV. However, a new subtraction scheme called Power Divergence Subtraction (PDS) was developed [14], where also the  $D = 2$  poles of  $I_0$  are subtracted. This makes  $I_0$  dependent on the scale  $\mu$ :

$$I_0^{\text{PDS}} \equiv -\frac{M}{4\pi}(\mu + ip), \quad (2.13)$$

and the amplitude (2.11) becomes

$$i\mathcal{A} = -\frac{4\pi}{M} \frac{i}{\frac{4\pi}{MC_0} + \mu + ip}. \quad (2.14)$$

<sup>5</sup>The parameter  $\mu$  has the dimension of a mass and denotes the renormalization scale.

This reproduces the ERT result (2.4) if  $C_0$  is chosen such that

$$\frac{4\pi}{MC_0} = \frac{1}{a_0} - \mu. \quad (2.15)$$

What we have achieved by using PDS is that now a fine-tuning between  $C_0$  and the linear divergence in  $I_0$  is possible, because both depend on  $\mu$ . Physically this means that a portion of the attractive potential represented by  $C_0$  cancels against the repulsive effect of the virtual kinetic energy of the nucleons [1]. Finally, a note on power counting should be made: Because of the fine-tuning allowed by PDS it is consistent to assume that  $1/a_0 \sim Q$  although it is numerically smaller than  $p$ , since choosing  $\mu \sim Q$  makes the  $1/a_0$ -dependent quantity  $1/C_0$  scale as  $Q$ . Now  $C_0 I_0 \sim a_0 p \sim Q^0$ , so all diagrams in Fig. 2.1 indeed contribute at the same order.

### 2.2.3 Dibaryon Fields

An equivalent way to deal with the existence of low-energy bound states in the two-nucleon system was suggested in [13]: The inclusion of an explicit dibaryon field that represents a bound state (in the  $^3S_1$  channel) or a quasi-bound state ( $^1S_0$  channel) of two nucleons. This formulation simplifies calculations compared to considering directly contact interactions between four nucleons, as in the previous subsection. Now the effective range must be taken into account: In Sect. 2.2.1, we mentioned that it is not clear a priori how to count  $r_0$  and  $\rho_d$ . We choose them to scale as  $Q^{-1}$ , as justified at the end of this Section.

In the dibaryon formulation, the NN interaction in the  $^1S_0$  channel is described by the following LO Lagrangean:

$$\begin{aligned} \mathcal{L} = & N^\dagger \left( i\partial_0 + \frac{\nabla^2}{2M} \right) N - s_a^\dagger \left( i\partial_0 + \frac{\nabla^2}{4M} - \Delta_s \right) s_a \\ & - y_s \left( s_a^\dagger N^T P_a^{(^1S_0)} N + \text{H.c.} \right). \end{aligned} \quad (2.16)$$

The parameters  $y_s$  and  $\Delta_s$  are fixed by matching the resulting NN scattering amplitude to (2.4), and the dibaryon field is denoted by  $s_a$ , with  $a = 1, 2, 3$  being the isospin index representing the  $I = 1$  state. The unusual sign of the dibaryon term is convention, and H.c. denotes the Hermitean conjugate.

The equivalence of (2.16) and (2.10) can be seen by performing the Gaussian integration over the  $s_a$  field in the path integral [17]. After a field redefinition, (2.10) is recovered and only the combination  $\frac{y_s^2}{4\Delta_s}$  enters, corresponding to the single parameter  $C_0$ .

$$\text{====} = \text{——} + \text{——} \circ \text{——} + \text{——} \circ \circ \text{——} + \dots$$

Figure 2.2: The dressed dibaryon propagator: the double line stands for the sum of diagrams with arbitrary insertions of nucleon bubbles, while the thick line represents the free dibaryon propagator.

In order to derive the amplitude, an expression for the dibaryon propagator is required. The full propagator is dressed with an infinite chain of nucleon bubbles (see Fig. 2.2), all of which contribute at the same order (as in the previous Subsection):

$$iD_s = iD_0 + iD_0ID_0 + iD_0ID_0ID_0 + \dots = \frac{iD_0}{1 - ID_0}. \quad (2.17)$$

The free propagator as a Green's function of  $\left(i\partial_0 + \frac{\nabla^2}{4M} - \Delta_s\right)$  is

$$iD_0 = \frac{-i}{E - \frac{\mathbf{p}_d^2}{4M} - \Delta_s}, \quad (2.18)$$

where  $E$  is the kinetic energy of the dibaryon and  $\mathbf{p}_d$  its momentum, and the loop integral is given by

$$\begin{aligned} I &= i \left(\frac{\mu}{2}\right)^{3-D} \int \frac{d^{(D+1)}l}{(2\pi)^{(D+1)}} \frac{i}{(l_0 - \frac{l^2}{2M} + i\varepsilon)} \frac{i}{(E - l_0 - \frac{(\mathbf{p}_d - l)^2}{2M} + i\varepsilon)} (-iy)^2 \\ &= \frac{y^2 M}{4\pi} \left( \sqrt{\frac{\mathbf{p}_d^2}{4} - EM - i\varepsilon - \mu} \right), \end{aligned} \quad (2.19)$$

where PDS is used to evaluate the divergent integral. Thus we arrive at

$$iD_s = \frac{-i}{E - \frac{\mathbf{p}_d^2}{4M} - \Delta_s + \frac{y^2 M}{4\pi} \sqrt{\frac{\mathbf{p}_d^2}{4} - EM - i\varepsilon - \frac{y^2 M}{4\pi} \mu}}. \quad (2.20)$$

In the center-of-mass (cm) frame ( $E = \frac{p^2}{M}$ ,  $\mathbf{p}_d = 0$ ), the LO NN scattering amplitude is then

$$\begin{aligned} i\mathcal{A} &= (-iy_s)iD_s(-iy_s) \\ &= \frac{iy_s^2}{\frac{p^2}{M} - \Delta_s + \frac{y^2 M}{4\pi}(-ip) - \frac{y^2 M}{4\pi}\mu}. \end{aligned} \quad (2.21)$$

Again comparing to eq. (2.4), we find for the  $^1S_0$  channel:

$$y_s = \frac{\sqrt{8\pi}}{M\sqrt{r_0}}, \quad \Delta_s = \frac{2}{Mr_0} \left( \frac{1}{a_0} - \mu \right). \quad (2.22)$$

Inserting this into (2.20), the deuteron propagator in the cm system becomes

$$iD_s = \frac{Mr_0}{2} \frac{i}{\frac{1}{a_0} - \frac{r_0}{2}EM + i\sqrt{EM}}. \quad (2.23)$$

In the  $^3S_1$  (triplet) channel,  $s_a$  is replaced by the field  $t_i$ , which represents the deuteron (see (2.32) below; the index  $i$  indicates the polarization). Repeating the above steps and matching to (2.9), we get

$$y_t = \frac{\sqrt{8\pi}}{M\sqrt{\rho_d}}, \quad \Delta_t = \frac{2}{M\rho_d} \left( \gamma - \frac{\rho_d}{2}\gamma^2 - \mu \right), \quad (2.24)$$

$$iD_t = \frac{M\rho_d}{2} \frac{i}{\gamma - \frac{\rho_d}{2}(\gamma^2 + EM) + i\sqrt{EM}}. \quad (2.25)$$

For external deuteron fields, we need a wave-function renormalization factor  $Z$  which gives the asymptotic normalization of the deuteron's wave-function tail. It is crucial to reproduce the long-range part of the wave-function (see e. g. [16]),

$$\Psi_{deuteron}(r \rightarrow \infty) = \sqrt{\frac{Z}{2\pi\rho_d}} \frac{e^{-\gamma r}}{r}, \quad (2.26)$$

since it is this quantity that dominates the response to low-energy probes. The rate of exponential fall-off of the wave function is determined by the binding energy, and  $Z$  is given by the residue of the deuteron propagator at the pole:

$$\begin{aligned} \frac{iZ}{E+B} \Big|_{E=-B} &= iD_t|_{E=-B} \\ \Rightarrow \frac{1}{Z} \frac{\partial}{\partial E} (E+B) \Big|_{E=-B} &= \frac{2}{M\rho_d} \frac{\partial}{\partial E} \left( \gamma - \frac{\rho_d}{2}(\gamma^2 + EM) - i\sqrt{-EM - i\varepsilon} \right) \Big|_{E=-B} \\ &\Rightarrow Z = \frac{\gamma\rho_d}{1 - \gamma\rho_d}. \end{aligned} \quad (2.27)$$

Now we come to the question how to count  $\rho_d$  and  $r_0$ . Numerically, they are  $\rho_d = \frac{1}{112 \text{ MeV}}$  and  $r_0 = \frac{1}{72 \text{ MeV}}$ . Originally it was suggested that  $\rho_d \sim r_0 \sim Q^0$ ,

i. e. they are regarded to be of natural size [14]. This would mean that the factor  $Z$  should be expanded in powers of  $\gamma\rho_d \sim Q$ :

$$\begin{aligned} Z &= \gamma\rho_d[1 + \gamma\rho_d + (\gamma\rho_d)^2 + \dots] \\ &= 0.408[1 + 0.408 + 0.166 + 0.068 + \dots]. \end{aligned} \quad (2.28)$$

However, the convergence is rather bad (see [18] for a discussion): The NNLO contribution is still about 17% of the LO one. Thus it seems more accurate to reproduce the correct wave-function tail at LO, taking  $\rho_d \sim Q^{-1}$  (as suggested in [19]) and then, of course, also  $r_0 \sim Q^{-1}$ . We adopt the latter convention. This is consistent with regarding (2.18) as the free propagator at LO, because if  $r_0 \sim Q^0$ , then  $\Delta \sim Q$  and the kinetic term would only be a NLO correction to  $\Delta$  (as in [20]).

So far, we did nothing more than reproduce the results of the traditional ERT. The power of EFT( $\not{x}$ ) lies in the fact that it can be used to calculate processes with external probes like electromagnetic fields, including higher order operators that are not present in ERT. In the next Section this extension is introduced.

## 2.3 Lagrangean and Power Counting

In the following, we write down the Lagrangean that describes all processes examined in this work. Possible higher order terms will be discussed when processes are covered where they might play a role. The interaction of nucleons and dibaryons with an electric field is implemented at LO by gauging the Lagrangean (2.16). For nucleons,  $\partial_\mu \rightarrow D_\mu = \partial_\mu + ieQA_\mu$ , where  $Q = \frac{1}{2}(\mathbb{1} + \tau_3)$  is the charge matrix, whereas for the dibaryon  $D_\mu = \partial_\mu + ieA_\mu$ .<sup>6</sup>

The effective Lagrangean can be written in the form (see [21] for a review)

$$\mathcal{L} = \mathcal{L}_N + \mathcal{L}_s + \mathcal{L}_t + \mathcal{L}_{st}. \quad (2.29)$$

To the order needed in this work, the four parts read

$$\mathcal{L}_N = N^\dagger \left[ iD_0 + \frac{\mathbf{D}^2}{2M} + \frac{e}{2M}(\kappa_0 + \kappa_1\tau_3)\boldsymbol{\sigma} \cdot \mathbf{B} \right] N, \quad (2.30)$$

$$\mathcal{L}_s = -s_a^\dagger \left[ iD_0 + \frac{\mathbf{D}^2}{4M} - \Delta_s \right] s_a - y_s \left[ s_a^\dagger N^T P_a^{(1S_0)} N + \text{H.c.} \right], \quad (2.31)$$

---

<sup>6</sup>This means, of course,  $D_0 = \partial_0 + ieA_0$  and  $\mathbf{D} = \nabla - ie\mathbf{A}$ .

$$\begin{aligned}
\mathcal{L}_t &= -t_i^\dagger \left[ iD_0 + \frac{\mathbf{D}^2}{4M} - \Delta_t \right] t_i - y_t \left[ (t_i^\dagger N^T P_i^{(3S_1)} N + \text{H.c.}) \right. \\
&\quad \left. - \frac{C_{sd}}{\sqrt{M\rho_d}} \mathcal{T}_{ij,xy}^{(sd)} \left[ t_i^\dagger (N^T \mathcal{O}_{xy,j} N) + \text{H.c.} \right] \right. \\
&\quad \left. - \frac{C_Q}{M\rho_d} t_i^\dagger [iD_0, \mathcal{O}_{ij}] t_j, \right. \tag{2.32}
\end{aligned}$$

$$\mathcal{L}_{st} = \frac{eL_1}{M\sqrt{r_0\rho_d}} \left[ t_i^\dagger s_3 B_i + \text{H.c.} \right]. \tag{2.33}$$

The one-nucleon Lagrangean  $\mathcal{L}_N$  contains – aside from the kinetic term – the interaction with a magnetic field  $\mathbf{B} = \nabla \times \mathbf{A}$  via the isoscalar and isovector magnetic moments of the nucleon,

$$\kappa_0 = \frac{1}{2}(\kappa_p + \kappa_n), \quad \kappa_1 = \frac{1}{2}(\kappa_p - \kappa_n), \tag{2.34}$$

where the magnetic moments of proton and neutron in nuclear magnetons are

$$\kappa_p = 2.79, \quad \kappa_n = -1.91. \tag{2.35}$$

$\mathcal{L}_s$  and  $\mathcal{L}_t$  are the Lagrangeans for the dibaryon fields in the  $^1S_0$  and  $^3S_1$  channels,  $s_a$  and  $t_i$ , respectively (the index  $i = 1, 2, 3$  indicates the polarization of the spin-triplet state). The second terms describe the formation and breakup of a dibaryon, where the projection operators are (see App. B for details):

$$P_a^{(1S_0)} = \frac{1}{\sqrt{8}} \sigma_2 \tau_2 \tau_a, \quad P_i^{(3S_1)} = \frac{1}{\sqrt{8}} \sigma_2 \sigma_i \tau_2. \tag{2.36}$$

In the triplet channel, transitions between  $S$ - and  $D$ -wave are covered by the third and fourth terms of  $\mathcal{L}_t$  (2.32). The corresponding operators read

$$\mathcal{T}_{ij,xy}^{(sd)} = \delta_{ix} \delta_{jy} - \frac{1}{3} \delta_{ij} \delta_{xy}, \tag{2.37}$$

$$\mathcal{O}_{ij} = - \left( \mathbf{D}_i \mathbf{D}_j - \frac{1}{3} \delta_{ij} \mathbf{D}^2 \right), \tag{2.38}$$

$$\mathcal{O}_{xy,j} = -\frac{1}{4} \left( \overleftarrow{\mathbf{D}}_x \overleftarrow{\mathbf{D}}_y P_j^{(3S_1)} + P_j^{(3S_1)} \overrightarrow{\mathbf{D}}_x \overrightarrow{\mathbf{D}}_y - \overleftarrow{\mathbf{D}}_x P_j^{(3S_1)} \overrightarrow{\mathbf{D}}_y - \overleftarrow{\mathbf{D}}_y P_j^{(3S_1)} \overrightarrow{\mathbf{D}}_x \right). \tag{2.39}$$

The arrows in (2.39) indicate the direction in which the operators act. All operators are constructed in such a way that gauge invariance is guaranteed. The coefficient  $C_{sd}$  will be determined from the experimental value of the  $SD$  mixing parameter  $\eta_{sd}$ , while  $C_Q$  will be fixed by the quadrupole moment (see Chapter 3.1.3).

$\mathcal{L}_{st}$  accounts for a transition between the  $^1S_0$  and  $^3S_1$  channels caused by a magnetic field acting on a dibaryon. Again there is an unknown coefficient,  $L_1$ , which has to be determined by matching to data. This will be done in Chapter 3.2 by considering the cross section for radiative neutron capture by the proton.

A compilation of the Feynman rules that correspond to the above Lagrangean is given in Appendix A. Most of the power counting rules have already been set up and are now summarized. The basic low-energy quantities scale as follows:

$$|\mathbf{p}| \sim \sqrt{Mp^0} \sim \gamma \sim \frac{1}{\rho_d} \sim \frac{1}{r_0} \sim \frac{1}{a_0} \sim Q. \quad (2.40)$$

Hence the wave function renormalization factor scales as  $Z \sim 1$ . For the nucleon-propagator

$$\frac{1}{q^0 - \frac{q^2}{2M}} \sim Q^{-2}, \quad (2.41)$$

and for the dibaryon propagators (2.23, 2.25)

$$D_s \sim D_t \sim Q^{-2}. \quad (2.42)$$

Each NN-dibaryon vertex – proportional to  $y_{s,t}$  – brings a factor  $Q^{1/2}$  by combining (2.22/2.24) with (2.40).  $SD$  mixing is suppressed by  $Q^2$  with respect to pure  $S$ -wave amplitudes because of the two derivatives in (2.32); thus the coefficient  $\frac{C_{sd}}{\sqrt{M\rho_d}}$  is of the same order as  $y_{s,t} \sim Q^{1/2}$ . The denominators of  $\frac{C_{sd}}{\sqrt{M\rho_d}}$  and  $\frac{C_Q}{M\rho_d}$  are chosen such that  $C_{sd} \sim C_Q \sim 1$  are of natural size. Likewise, the coefficient of  $\mathcal{L}_{st}$  in (2.33) is written in a way that  $L_1$  is also natural. Besides we note that the isovector magnetic moment  $\kappa_1 = 2.35$  is numerically much larger than the isoscalar one  $\kappa_0 = 0.44$ ; the latter is therefore treated as higher order and is neglected in the following (see discussion in Sect. 3.2.3). Since a space (time) derivative of a nucleon or dibaryon field gives  $p \sim Q$  ( $p^0 \sim Q^2$ ), a minimally coupled photon should also scale as

$$\mathbf{A} \sim Q, \quad A^0 \sim Q^2, \quad (2.43)$$

and the corresponding vertices as  $A^0 \sim \mathbf{p} \cdot \mathbf{A} \sim Q^2$ .

Now the tools for calculating the response of a two-nucleon system to an external electromagnetic field are at hand. We discussed NN scattering in some detail and wrote down the terms relevant in the following, where they will be examined further.

# Chapter 3

## Applications

Before we come to the main part of this work, let us consider some applications of EFT( $\not{\pi}$ ), i. e. reproduce some results that have been derived before. This is done for several reasons: to get familiar with the theory by considering relatively simple processes first; to show some of its successes; and – most importantly – to determine some unknown coefficients in the Lagrangean by comparing the results to data. In the following, we calculate the electric form factors of the deuteron, and in Sect. 3.2 the radiative capture process of slow neutrons by protons.

### 3.1 Electric Form Factors of the Deuteron

#### 3.1.1 Elastic Electron-Deuteron Scattering

The differential cross section for elastic electron-deuteron scattering

$$\frac{d\sigma}{d\Omega} = \frac{d\sigma}{d\Omega}\Big|_{\text{Mott}} \left[ A(q) + B(q) \tan\left(\frac{\theta}{2}\right) \right] \quad (3.1)$$

is the Mott cross section (describing electron scattering off a pointlike particle) times a correction given by the form factors  $A(q)$  and  $B(q)$  that can be written in terms of the charge-, magnetic- and quadrupole form factors of the deuteron,  $F_C(q)$ ,  $F_M(q)$  and  $F_Q(q)$ , respectively:

$$A(q) = F_C^2(q) + \frac{2}{3}\eta F_M^2(q) + \frac{8}{9}\eta^2 F_Q^2(q), \quad B(q) = \frac{4}{3}\eta(1 + \eta)F_M^2(q), \quad (3.2)$$

where  $\eta = \frac{q^2}{4M_d^2}$ .

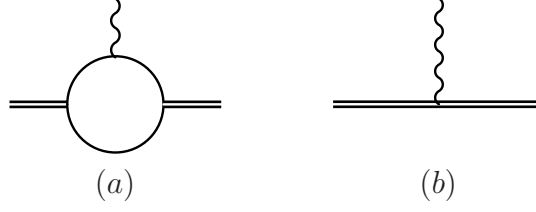


Figure 3.1: LO diagrams contributing to the deuteron charge form factor.

In the following, we reproduce the analytic expressions for the electric form factors as given e. g. in [11]. A deuteron is characterized by its four-momentum  $p^\mu$  and polarization vector  $\epsilon^\mu$  with  $p_\mu \epsilon^\mu = 0$ . The basis of polarization vectors can be chosen so that  $\epsilon_i^\mu = \delta_i^\mu$ . Deuteron states are then denoted by  $|\mathbf{p}, i\rangle \equiv |\mathbf{p}, \epsilon_i^\mu\rangle$  and fulfill the normalization condition  $\langle \mathbf{p}', j | \mathbf{p}, i \rangle = (2\pi)^3 \delta^3(\mathbf{p} - \mathbf{p}') \delta_{ij}$ . In terms of these states, the nonrelativistic expansion of the matrix element of the electromagnetic current up to NNLO is

$$\begin{aligned} \langle \mathbf{p}', j | J_{\text{em}}^0 | \mathbf{p}, i \rangle &= e \left[ F_C(q) \delta_{ij} + \frac{1}{2M_d^2} F_Q(q) \left( \mathbf{q}_i \mathbf{q}_j - \frac{1}{3} q^2 \delta_{ij} \right) \right] \left( \frac{E + E'}{2M_d} \right), \\ \langle \mathbf{p}', j | \mathbf{J}_{\text{em}}^k | \mathbf{p}, i \rangle &= \frac{e}{2M_d} \left[ F_C(q) \delta_{ij} (\mathbf{p} + \mathbf{p}')^k + F_M(q) (\delta_i^k \mathbf{q}_j - \delta_j^k \mathbf{q}_i) \right. \\ &\quad \left. + \frac{1}{2M_d^2} F_Q(q) \left( \mathbf{q}_i \mathbf{q}_j - \frac{1}{3} q^2 \delta_{ij} \right) (\mathbf{p} + \mathbf{p}')^k \right]. \end{aligned} \quad (3.3)$$

### 3.1.2 Charge Form Factor

The LO contributions to the electric charge form factor  $F_C$  of the deuteron are depicted in Fig. 3.1. The matrix elements are (from (A.1) and (A.2))

$$\langle \mathbf{p}', j | J^{0(a)} | \mathbf{p}, i \rangle = eZ \frac{4}{q\rho_d} \arctan \left( \frac{q}{4\gamma} \right) \delta_{ij}, \quad (3.4)$$

$$\langle \mathbf{p}', j | J^{0(b)} | \mathbf{p}, i \rangle = -eZ, \quad (3.5)$$

where the wave-function renormalization factor  $Z$  is given by (2.27). Comparing this to the definition of the charge form factor in (3.3), we find

$$F_C^{LO}(q) = Z \left[ \frac{4}{q\rho_d} \arctan \left( \frac{q}{4\gamma} \right) - 1 \right], \quad (3.6)$$

which fulfills the conventional normalization  $F_C(0) = 1$ .

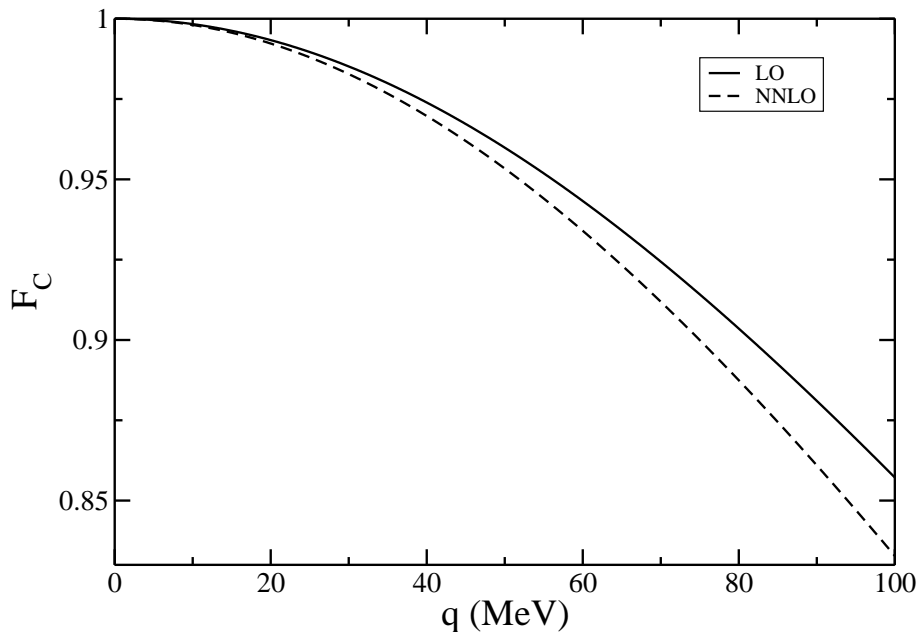


Figure 3.2: Comparison of the charge form factors calculated to LO and NNLO.

It is interesting to compare the LO result to that obtained in the NNLO calculation in [22] (Fig. 3.2).<sup>1</sup> The latter includes the contribution from the nucleon mean-square charge radius  $\langle r_N^2 \rangle$  as well as relativistic corrections. We see that the deviation between the two results indeed becomes very small for low momenta. The good convergence of the theory in this application can also be demonstrated by looking at the mean-square charge radius of the deuteron which is defined via an expansion of  $F_C(q) = 1 - \frac{1}{6}\langle r_d^2 \rangle q^2 + \dots$  in powers of  $q^2$ ,  $\langle r_d^2 \rangle = -6 \frac{dF_C}{dq^2}(q=0)$ . The LO result is

$$\langle r_d^2 \rangle^{LO} = \frac{1}{1 - \gamma \rho_d} \frac{1}{8\gamma^2} = 3.92 \text{ fm}^2, \quad (3.7)$$

while at NNLO one finds

$$\langle r_d^2 \rangle^{NNLO} = \frac{1}{1 - \gamma \rho_d} \frac{1}{8\gamma^2} + \langle r_N^2 \rangle + \frac{1}{32M^2} = 4.55 \text{ fm}^2. \quad (3.8)$$

This is very close to the experimental value  $\langle r_d^2 \rangle = 4.538 \text{ fm}^2$ .

---

<sup>1</sup>Note that in [22] a different power counting scheme is used, in which  $Z$  is not exactly reproduced at LO.

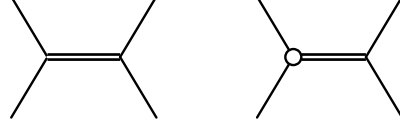


Figure 3.3: Diagrams for the NN scattering amplitudes in the  $S$ -to- $S$ -wave and  $D$ -to- $S$ -wave channels. The open circle denotes the  $D$ -to- $S$  transition and involves two spatial derivatives (see Feynman rule (A.6)).

### 3.1.3 $SD$ Mixing and Quadrupole Form Factor

The deuteron quadrupole form factor is non-zero because the deuteron wave function has a  $D$ -wave contribution, mentioned in Sect. 2.2.1. In the coupled  ${}^3S_1 - {}^3D_1$  channel, the analog to (2.1) is

$$S = 1 + i \frac{pM}{2\pi} \begin{pmatrix} \mathcal{A}_{[SS]} & \mathcal{A}_{[DS]} \\ \mathcal{A}_{[DS]} & \mathcal{A}_{[DD]} \end{pmatrix} = \begin{pmatrix} e^{2i\bar{\delta}_0} \cos 2\bar{\epsilon}_1 & ie^{i(\bar{\delta}_0 + \bar{\delta}_2)} \sin 2\bar{\epsilon}_1 \\ ie^{i(\bar{\delta}_0 + \bar{\delta}_2)} \sin 2\bar{\epsilon}_1 & e^{2i\bar{\delta}_2} \cos 2\bar{\epsilon}_1 \end{pmatrix}, \quad (3.9)$$

where the conventions of the phase shifts are defined in [23]. The Lagrangean that describes the mixing at LO is the third term in  $\mathcal{L}_t$  (2.32), containing the unknown coefficient  $C_{sd}$ , which will now be determined by the empirically well-known quantity  $\eta_{sd} = 0.0254$  [24], the asymptotic ratio of  $D$ - and  $S$ -wave components of the deuteron wave function.

The NN scattering amplitudes for the  $S$ -to- $S$ -wave and  $D$ -to- $S$ -wave channels are represented by the diagrams in Fig. (3.3).  $\mathcal{A}_{[SS]}$  was given in (2.9), while

$$i\mathcal{A}_{[DS]} = i \frac{C_{sd}}{\sqrt{M\rho_d}} \frac{3}{4} \sqrt{\pi\rho_d} \frac{p^2}{-\gamma + \frac{1}{2}\rho_d(p^2 + \gamma^2) - ip}. \quad (3.10)$$

$D$ -to- $D$  transitions – involving four derivatives – are suppressed by two more powers of  $Q$  and can be neglected here. Then the asymptotic  $D$ - $S$  ratio is given by

$$\begin{aligned} \eta_{sd} &= -\frac{1}{2} \frac{\tan 2\bar{\epsilon}_1}{\sin(\bar{\delta}_0 - \bar{\delta}_2)} \Big|_{p=i\gamma} = -\frac{\mathcal{A}_{[DS]}}{\mathcal{A}_{[SS]}} \Big|_{p=i\gamma} \\ &= \frac{C_{sd}}{\sqrt{M\rho_d}} \frac{1}{6\sqrt{\pi}} M \sqrt{\rho_d} \gamma^2, \end{aligned} \quad (3.11)$$

and  $C_{sd}$  is thus fixed:

$$C_{sd} = \frac{6\sqrt{\pi}\eta_{sd}}{\sqrt{M}\gamma^2} = 2.31 \text{ fm}^{5/2}. \quad (3.12)$$

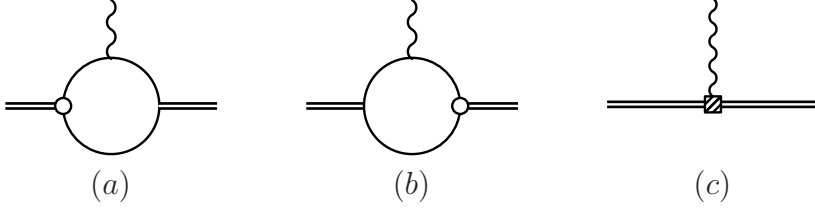


Figure 3.4: Diagrams contributing to the deuteron quadrupole form factor at LO (a,b) and at NLO (c). The shaded square represents the operator proportional to  $C_Q$  (cf. Feynman rule (A.10)).

This is almost equal to  $1/m_\pi^{5/2}$ , i. e. clearly of natural size.

Now that the coefficient for  $SD$  mixing is determined, we can calculate the LO contributions to the quadrupole form factor shown in Fig. 3.4 (a) and (b). The matrix element of the sum of both is

$$\begin{aligned} \langle \mathbf{p}', j | J^{0(a+b)} | \mathbf{p}, i \rangle &= 2eZy_t \frac{C_{sd}}{\sqrt{M\rho_d}} M^2 \int \frac{d^3l}{(2\pi)^3} \frac{\mathbf{l}\mathbf{l}^j - \frac{1}{3}l^2\delta^{ij}}{l^2 + \gamma^2 - i\epsilon} \frac{1}{(\mathbf{1} + \frac{\mathbf{q}}{2})^2 + \gamma^2 - i\epsilon} \\ &= e(\mathbf{q}^i\mathbf{q}^j - \frac{1}{3}q^2\delta^{ij})Zy_t \frac{C_{sd}}{\sqrt{M\rho_d}} \frac{M^2}{32\pi q^3} \\ &\quad \times \left[ -4\gamma q + (16\gamma^2 + 3q^2) \arctan\left(\frac{q}{4\gamma}\right) \right]. \end{aligned} \quad (3.13)$$

The integral is evaluated in the Appendix (D.10).

In addition to that, the quadrupole form factor has a contribution at NLO, arising from the fourth term in  $\mathcal{L}_t$  (2.32) and shown in Fig. 3.4 (c):

$$\langle \mathbf{p}', j | J^{0(c)} | \mathbf{p}, i \rangle = e(\mathbf{q}^i\mathbf{q}^j - \frac{1}{3}q^2\delta^{ij})Z \frac{C_Q}{M\rho_d}. \quad (3.14)$$

EFT( $\not{\pi}$ ) goes beyond ERT here, since this operator is not present in ERT. Combining the LO and NLO results, we find for the quadrupole form factor from (3.3):

$$\frac{F_Q(q)}{2M_d^2} = Z \left\{ y_t \frac{C_{sd}}{\sqrt{M\rho_d}} \frac{M^2}{32\pi q^3} \left[ -4\gamma q + (16\gamma^2 + 3q^2) \arctan\left(\frac{q}{4\gamma}\right) \right] + \frac{C_Q}{M\rho_d} \right\}. \quad (3.15)$$

This reproduces the expression given in [22] (when applying our power counting rules). The usual normalization condition is

$$\frac{1}{M_d^2} F_Q(0) = \mu_Q. \quad (3.16)$$

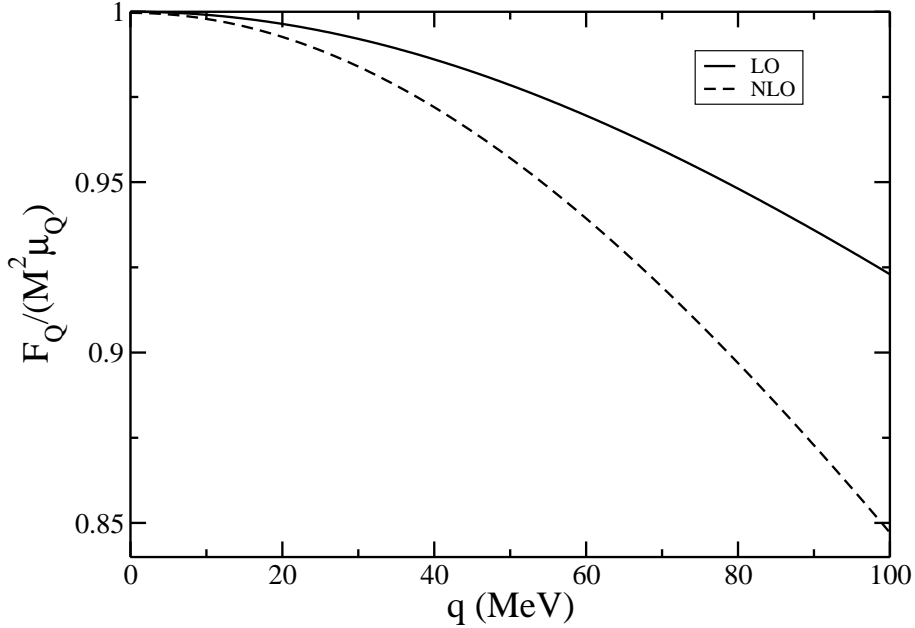


Figure 3.5: The quadrupole form factor, normalized to  $\mu_Q$ : The solid curve is obtained by fitting  $C_{sd}$  to the quadrupole moment at LO, while the dashed curve is the NLO result of (3.15) .

If we fit

$$\frac{1}{M_d^2} F_Q(0) = 2Z \left[ y_t \frac{C_{sd}}{\sqrt{M\rho_d}} \frac{M^2}{32\pi} \frac{2}{3\gamma} + \frac{C_Q}{M\rho_d} \right] \quad (3.17)$$

to the empirical value for the electric quadrupole moment  $\mu_Q = 0.2859 \text{ fm}^2$ , we find  $C_Q = -1.703 \text{ fm}^2$ . This is indeed  $\mathcal{O}(1)$ , i. e. of the order of  $1/m_\pi^2$ , so the naturalness assumption is confirmed.

For the quadrupole moment at leading order, i. e. setting  $C_Q \equiv 0$ , we get  $\mu_Q^{LO} = 0.566 \text{ fm}^2$ . Thus the NLO contribution is about  $-50\%$  of the LO one. One could, however, fit  $C_{sd}$  directly to the quadrupole moment at LO (eq. (3.17) without the  $C_Q$ -term), obtaining  $C_{sd}^{(LO)} = 1.17 \text{ fm}^{5/2}$ ; the resulting quadrupole form factor is plotted in Fig. 3.5, compared to the NLO one of eq. (3.15). We observe a rather large NLO contribution. Therefore, it is more accurate to fit  $C_{sd}$  not to the quadrupole moment but to  $\eta_{sd}$ , and reproduce  $\mu_Q$  at NLO. In calculating the electrodisintegration process, we will use (3.12) for  $C_{sd}$ .

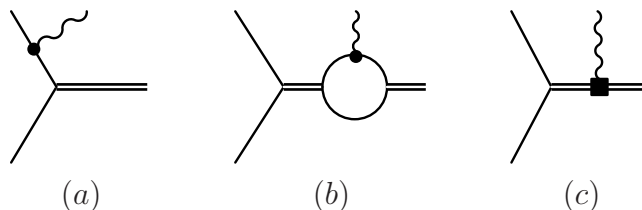


Figure 3.6: Diagrams contributing to the  $M1_V$  amplitude at LO (a,b) and at NLO (c).

## 3.2 Radiative Capture $np \rightarrow d\gamma$

Next we examine the radiative neutron capture by the proton. The cross section for this process at very low energies  $E < 1$  MeV is important for the understanding of big-bang nucleosynthesis, since it is needed as an input for calculations of the abundances of deuterium and other light elements. Therefore it has been studied in great detail within EFT( $\pi$ ) (see [25, 26, 27, 19]). We repeat it here to determine one more parameter,  $L_1$  of eq. (2.33), and because the amplitude is very similar to the one for deuteron electrodisintegration – the reverse process with the real photon being replaced by a virtual one. This gives us an additional criterion (besides power counting) to determine which diagrams are important and which can be neglected in the latter process. In the energy range of interest, the cross section is dominated by isovector magnetic transitions  $M1_V$  and isovector electric transitions  $E1_V$ , which will be calculated in the next two Subsections, followed by a comparison of these two and other possible contributions.

### 3.2.1 Magnetic Transitions

The isovector magnetic transition from the  $^1S_0$  isovector channel<sup>2</sup> to the  $^3S_1$  isoscalar channel at LO is determined by the isovector magnetic moment of the nucleon ( $\kappa_1$ -term in (2.30) and Feynman rule (A.2)). At NLO the operator in (2.33) and (A.11) enters, where a magnetic photon couples to a dibaryon; its coefficient  $L_1$  will be fixed by the experimental value of the  $np \rightarrow d\gamma$  cross section for thermal neutrons. The corresponding diagrams are depicted in Fig. 3.6. In the center-of-mass frame, the incoming nucleons have momenta  $\pm\mathbf{p}$ . Momentum and energy of the outgoing real photon are  $\mathbf{q}$  and  $q_0 = q = |\mathbf{q}|$ , respectively, and we work in Coulomb-gauge, where the polarization vector fulfills  $\mathbf{q} \cdot \epsilon_{(\gamma)}^* = 0$  (besides  $\epsilon_{(\gamma)}^{*0} = 0$ ). The amplitude can

<sup>2</sup>The spin-singlet state  $^1S_0$  must be an isospin-triplet because of the Pauli principle.

then be written as

$$i\mathcal{A} = ie\epsilon^{ijk}\epsilon_{(d)}^{*i}\mathbf{q}^j\epsilon_{(\gamma)}^{*k}(N_n^T\sigma_2N_p)X_{M1_V}, \quad (3.18)$$

where  $N_n$  and  $N_p$  are the neutron and proton spinors<sup>3</sup>. The sum of the diagrams in Fig. 3.6 gives

$$X_{M1_V} = i\frac{2}{M}\sqrt{Z}\frac{1}{-\frac{1}{a} + \frac{1}{2}r_0p^2 - ip}\left[\kappa_1\frac{\gamma - \frac{1}{a} + \frac{1}{2}r_0p^2}{p^2 + \gamma^2} + \frac{L_1}{2}\right] \quad (3.19)$$

which reproduces the expression in [19]. In obtaining this result, the nucleon propagator was approximated as

$$\left(\frac{p^2}{2M} - q - \frac{(\mathbf{p} \pm \mathbf{q})^2}{2M}\right)^{-1} \approx -\frac{1}{q}, \quad (3.20)$$

i. e. we neglected terms that are suppressed by a factor  $Q/M$  (which is even much smaller than the usual expansion parameter  $Q/\Lambda$ ). Besides we applied  $q \approx \frac{p^2 + \gamma^2}{M}$  from energy conservation. In this approximation, the differential cross section is (see e. g. [28])

$$\frac{d\sigma^{(M1_V)}}{d\Omega} = \frac{p^2 + \gamma^2}{16\pi^2 p} \sum_{\text{spin}} |\mathcal{A}|^2, \quad (3.21)$$

with

$$\begin{aligned} \sum_{\text{spin}} |\mathcal{A}|^2 &= e^2\epsilon^{ijk}\epsilon_{(d)}^{*i}\mathbf{q}^j\epsilon^{lmn}\epsilon_{(d)}^l\mathbf{q}^m\frac{1}{4}\text{Tr}[\sigma_2\sigma_2]\left(\delta^{kn} - \frac{\mathbf{q}^k\mathbf{q}^n}{q^2}\right)|X_{M1_V}|^2 \\ &= e^2q^2|X_{M1_V}|^2. \end{aligned} \quad (3.22)$$

The resulting contribution of  $M1_V$  transitions to the total cross section,

$$\sigma^{(M1_V)} = \frac{\alpha(p^2 + \gamma^2)^3}{pM^2}|X_{M1_V}|^2 \quad (3.23)$$

(with the fine structure constant  $\alpha = \frac{e^2}{4\pi}$ ), is now fitted to the experimental value for thermal neutrons  $\sigma(E = \frac{p^2}{M} = 1.264 \cdot 10^{-8} \text{ MeV}) = (334.2 \pm 0.5) \text{ mb}$  [29], fixing the coefficient  $L_1 = -4.41 \text{ fm}$ .<sup>4</sup> The justification for this procedure will be given later, when we will see that at this energy the cross

<sup>3</sup>Because of this specification we drop the  $\tau$ -matrices that would project on the appropriate isospin state of the two nucleons.

<sup>4</sup>This value is bit larger than expected by the naturalness assumption, but we can still treat it as  $\mathcal{O}(1)$ .

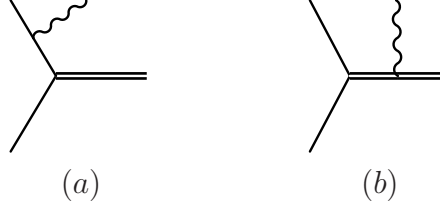


Figure 3.7: Diagram (a) shows the LO contribution to the  $E1_V$  amplitude; diagram (b) vanishes.

section is by far dominated by the  $M1_V$ -amplitude. Again the term arising from a four-nucleon-one-photon operator plays an important role (as for the form factors in the previous section), since the LO terms would give  $\sigma(L_1 = 0) = 501$  fm, which is about 1.5 times larger than the experimental value. We can expect that this NLO term is important for electrodisintegration as well.

### 3.2.2 Electric Transitions

The second important contribution to  $np \rightarrow d\gamma$  comes from isovector electric transitions  $E1_V$  from the isovector P-wave to the  ${}^3S_1$  channel. The only operator that enters at LO is obtained from gauging the kinetic term of the nucleons, and the diagram is depicted in Fig. 3.7 (a). The amplitude corresponding to the second diagram vanishes because it is proportional to  $\mathbf{q} \cdot \epsilon_{(\gamma)}^* = 0$ . Thus the LO amplitude is

$$i\mathcal{A} = e(N_n^T \sigma_2 \sigma \cdot \epsilon_{(d)}^* N_p) \mathbf{p} \cdot \epsilon_{(\gamma)}^* X_{E1_V}, \quad (3.24)$$

where

$$X_{E1_V} = -i \frac{2}{M} \sqrt{Z} \frac{1}{p^2 + \gamma^2}, \quad (3.25)$$

again in accord with [19]. Hence the differential cross section for  $E1_V$  transitions is (from (3.21))

$$\frac{d\sigma^{(E1_V)}}{d\Omega} = \frac{p^2 + \gamma^2}{16\pi^2 p} e^2 |X_{E1_V}|^2 \frac{3}{2} p^2 (1 - \cos^2 \theta), \quad (3.26)$$

where  $\theta$  is the angle between  $\mathbf{p}$  and  $\mathbf{q}$ , and the contribution to the total cross section is

$$\sigma^{(E1_V)} = \alpha p (p^2 + \gamma^2) |X_{E1_V}|^2. \quad (3.27)$$

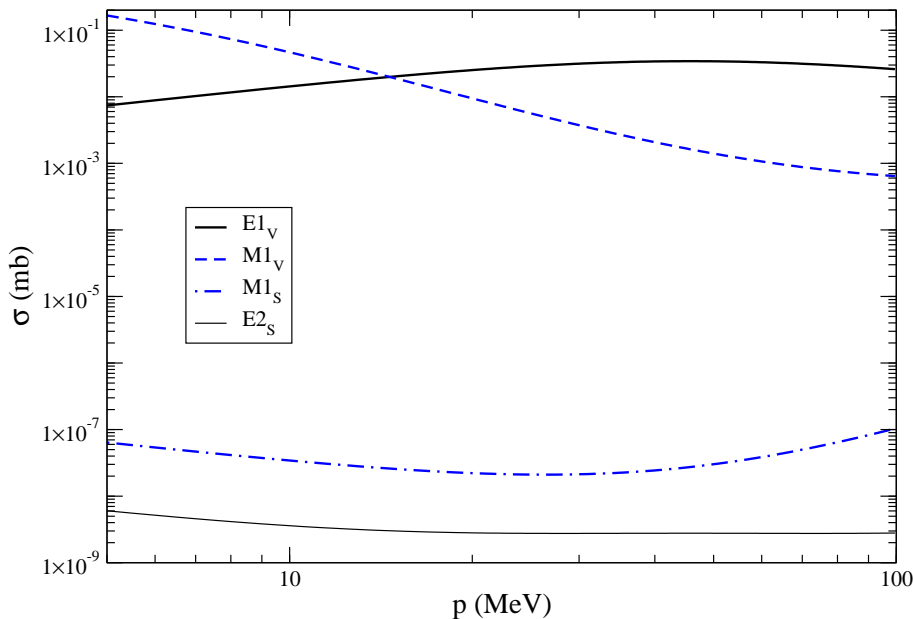


Figure 3.8: Comparison of individual contributions to the  $np \rightarrow d\gamma$  cross section. The  $M1_S$  and  $E2_S$  cross sections are taken from [27].

### 3.2.3 Comparison of Individual Contributions

Comparing the cross sections for  $M1_V$  (3.23) and  $E1_V$  (3.27), we see that at very low energies magnetic transitions dominate over electric ones. For thermal neutrons, the  $E1_V$  cross section is only  $\sigma^{(E1_V)} = 5 \cdot 10^{-6}$  mb, compared to  $\sigma^{(M1_V)} = 334.2$  mb. This justifies that  $L_1$  was fixed by the experimental value of the cross section. With increasing energy, however, electric transitions become more important and eventually dominate by about two orders of magnitude, as can be seen in Fig. 3.8, where the different contributions to the cross section are plotted as functions of the nucleon center-of-mass momentum  $p$ . Apart from the  $M1_V$  and  $E1_V$  parts calculated above, two other contributions are shown: isoscalar magnetic transitions  $M1_S$  and isoscalar electric transitions  $E2_S$  from the  ${}^3S_1$  channel. The corresponding cross sections are taken from [27] and have been included here to show that they are several orders of magnitude smaller than the dominating parts. We can expect this behavior also for deuteron-electrodisintegration, since the amplitude is very similar to that for  $np \rightarrow d\gamma$ .

# Chapter 4

## Deuteron-Electrodisintegration

Now we come to the main part of this work. In this Chapter, the calculation of the cross section of deuteron-electrodisintegration is presented. After introducing the formalism and kinematic relations, we calculate the amplitude for electric transitions at LO, which gives the dominant contribution, as expected from the previous section. Then we consider the major corrections to this, namely  $SD$  mixing which is the only NNLO contribution to electric transitions, and magnetic transitions (up to NLO). We conclude this Chapter with a discussion of possible higher order terms that are left out in the calculation. The results for the cross section will be shown and discussed in the next Chapter.

### 4.1 Kinematics and Formalism

#### 4.1.1 Kinematics

We begin by introducing the kinematic variables that describe the disintegration process  $d(e, e'p)n$  illustrated in Fig. 4.1. There are two frames of reference that are used conventionally: the laboratory frame – identified with the deuteron rest frame – which will have a superscript “lab”, and the center-of-mass frame of the outgoing nucleons (and of photon and deuteron), denoted by “cm”. The transformation between them is given by a boost along the three-momentum transfer  $\mathbf{q}$  by which we define the  $z$ -direction. Another frame of reference is the center-of-mass frame of the whole process, i. e. of the incoming electron and deuteron, where the analysis of the experiment in Ref. [9] is said to be carried out. There are, however, some misconceptions regarding their choice of reference frame; we will come back to this problem at the end of this Subsection. Here we list only the relevant variables in

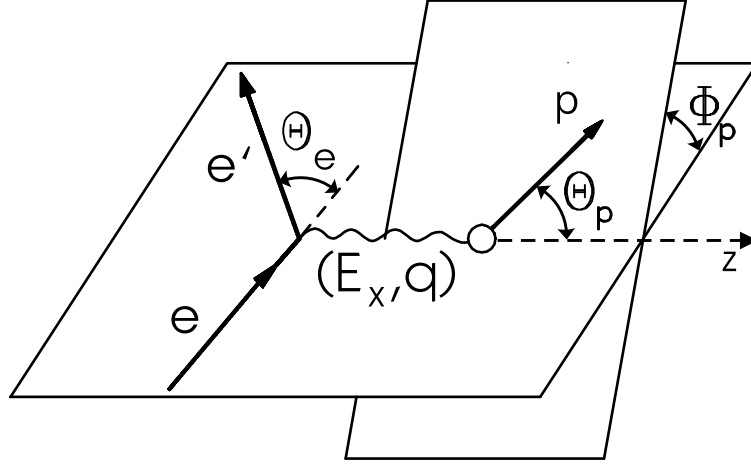


Figure 4.1: An illustration of the deuteron-electrodisintegration process: The electron kinematics refers to the lab frame, while the proton variables are defined in the cm frame of the two-nucleon final state.

the first two reference frames. Thus, “cm frame” will always stand for the proton-neutron cm frame, unless explicitly stated otherwise.

Energies and momenta of the electrons are given in the lab frame as the natural frame for the experimental determination of cross sections:  $(E_0^{\text{lab}}, \mathbf{k}^{\text{lab}})$  for incoming electrons and  $(E_e^{\text{lab}}, \mathbf{k}'^{\text{lab}})$  for outgoing ones. The angle between  $\mathbf{k}^{\text{lab}}$  and  $\mathbf{k}'^{\text{lab}}$  is  $\Theta_e^{\text{lab}}$ . The transferred energy and momentum are then

$$\omega^{\text{lab}} \equiv E_X^{\text{lab}} = E_0^{\text{lab}} - E_e^{\text{lab}}, \quad \mathbf{q}^{\text{lab}} = \mathbf{k}^{\text{lab}} - \mathbf{k}'^{\text{lab}}. \quad (4.1)$$

For the calculation it is convenient to switch to the cm frame. The reason will become clear in the next subsection: The hadronic part of the process,  $\gamma^*d \rightarrow pn$ , can be separated from the leptonic part and is then easier to calculate in its own rest frame. So the outgoing proton (neutron) has momentum  $\mathbf{p} \equiv \mathbf{p}^{\text{cm}}$  ( $-\mathbf{p}$ ) and total energy  $E_{p(n)} \equiv E_{p(n)}^{\text{cm}} = M + \frac{p^2}{2M}$ , since nucleons can always be treated non-relativistically at the energies of interest. (We denote the absolute value of a three-momentum  $|\mathbf{p}| \equiv p$ .) The spherical angles of  $\mathbf{p}$  are  $\Theta_p \equiv \Theta_p^{\text{cm}}$  and  $\Phi_p \equiv \Phi_p^{\text{cm}}$ ,<sup>1</sup> i. e.  $\mathbf{p} \cdot \mathbf{q} = pq \cos \Theta_p$  and  $\mathbf{p} \cdot (\mathbf{q} \times \mathbf{k}) \propto \sin \Phi_p$ .

The boost parameters for the transformation between the two frames are

<sup>1</sup>In the following,  $p$ ,  $\Theta_p$  and  $\Phi_p$  are always meant to be in the cm frame, and we drop the superscript “cm”. Likewise, all other variables without a superscript refer to the cm frame.

given by

$$\beta = \frac{q^{\text{lab}}}{M_d + \omega^{\text{lab}}}, \quad \gamma = \frac{1}{\sqrt{1 - \beta^2}}, \quad (4.2)$$

where  $M_d = 2M - B$  is the deuteron mass. Hence the quantities defined in the lab frame in (4.1) can be transformed to the cm frame as follows:

$$\omega \equiv \omega^{\text{cm}} = \gamma\omega^{\text{lab}} - \beta\gamma q^{\text{lab}}, \quad (4.3)$$

$$q \equiv q^{\text{cm}} = \beta\gamma M_d. \quad (4.4)$$

There are five independent variables for this process. We choose the energies  $E_0^{\text{lab}}$ ,  $E_e^{\text{lab}}$  (or equivalently  $E_X^{\text{lab}} = E_0^{\text{lab}} - E_e^{\text{lab}}$ ) and the scattering angle  $\Theta_e^{\text{lab}}$  of the electrons in the lab frame, and the proton emission angles  $\Theta_p$  and  $\Phi_p$  in the cm frame. The total energy of the deuteron in the cm frame is  $E_d = M_d + \frac{q^2}{2M_d}$ ; thus from energy conservation we can write the proton momentum as

$$p = \sqrt{(\omega - B)M + q^2 \frac{M}{2M_d}}. \quad (4.5)$$

Finally, we write down the involved momentum vectors:

$$\mathbf{k}^{\text{lab}} = (\sin \Theta_{0q}^{\text{lab}}, 0, \cos \Theta_{0q}^{\text{lab}})k^{\text{lab}}, \quad (4.6)$$

$$\mathbf{k}'^{\text{lab}} = (\sin \Theta_{eq}^{\text{lab}}, 0, \cos \Theta_{eq}^{\text{lab}})k'^{\text{lab}}, \quad (4.7)$$

$$\mathbf{q}^{\text{lab}} = (0, 0, 1)q^{\text{lab}}, \quad (4.8)$$

$$\mathbf{q} \equiv \mathbf{q}^{\text{cm}} = (0, 0, 1)q, \quad (4.9)$$

$$\mathbf{p} = (\sin \Theta_p \cos \Phi_p, \sin \Theta_p \sin \Phi_p, \cos \Theta_p)p, \quad (4.10)$$

with

$$\cos \Theta_{0q}^{\text{lab}} = \frac{k^{\text{lab}} - k'^{\text{lab}} \cos \Theta_e^{\text{lab}}}{q^{\text{lab}}}, \quad \cos \Theta_{eq}^{\text{lab}} = \frac{k^{\text{lab}} \cos \Theta_e^{\text{lab}} - k'^{\text{lab}}}{q^{\text{lab}}} \quad (4.11)$$

defining the angles between the electrons (incoming and outgoing respectively) and the photon. The electron momenta are given by  $k^{\text{lab}2} = E_0^{\text{lab}2} - m_e^2$  and  $k'^{\text{lab}2} = E_e^{\text{lab}2} - m_e^2$ , and the electron mass is  $m_e = 0.511$  MeV.

The quantity we want to calculate is the triple-differential cross section

$$\frac{d^3\sigma}{dE_e^{\text{lab}} d\Omega_e^{\text{lab}} d\Omega_p}, \quad (4.12)$$

where the spherical angles are given by  $\Omega_e^{\text{lab}} = (\Theta_e^{\text{lab}}, \Phi_e^{\text{lab}} \equiv 0)$  and  $\Omega_p \equiv \Omega_p^{\text{cm}} = (\Theta_p, \Phi_p)$ . The expression in terms of kinematic factors and the

scattering amplitude differs from the usual single differential cross section for a two-particle-to-two-particle reaction such as the photodisintegration process. In Appendix C we derive

$$\frac{d^3\sigma}{dE_e^{\text{lab}}d\Omega_e^{\text{lab}}d\Omega_p} = \frac{k'^{\text{lab}}pM_dM^2}{8(2\pi)^5(M + \frac{p^2}{2M})\sqrt{(M_dE_0^{\text{lab}} + \mathbf{q}^{\text{lab}} \cdot \mathbf{k}^{\text{lab}})^2 - M_d^2m_e^2}}|\mathcal{A}|^2. \quad (4.13)$$

This cross section can be split into the contributions of different structure functions. This decomposition can be written as

$$\frac{d^3\sigma}{dE_e^{\text{lab}}d\Omega_e^{\text{lab}}d\Omega_p} = \frac{d^3}{dE_e^{\text{lab}}d\Omega_e^{\text{lab}}d\Omega_p}(\sigma_L + \sigma_T + \sigma_{LT} \cos \Phi_p + \sigma_{TT} \cos 2\Phi_p). \quad (4.14)$$

A separation of the longitudinal-plus-transverse cross section  $\sigma_L + \sigma_T$  and the interference terms  $\sigma_{LT}$  and  $\sigma_{TT}$  can simply be made by varying  $\Phi_p$ :

$$\sigma_L + \sigma_T = \frac{1}{2}[\sigma(\Phi_p = 45^\circ) + \sigma(\Phi_p = 135^\circ)], \quad (4.15)$$

$$\sigma_{LT} = \frac{1}{\sqrt{2}}[\sigma(\Phi_p = 45^\circ) - \sigma(\Phi_p = 135^\circ)], \quad (4.16)$$

$$\begin{aligned} \sigma_{TT} &= \frac{1}{2}[\sigma(\Phi_p = 0^\circ) + \sigma(\Phi_p = 180^\circ)] \\ &\quad - \frac{1}{2}[\sigma(\Phi_p = 45^\circ) + \sigma(\Phi_p = 135^\circ)]. \end{aligned} \quad (4.17)$$

The decomposition (4.14) is valid either in the lab- or in the cm frame of the outgoing nucleons; since the transformation between these two frames is given by a boost along  $\mathbf{q}$ , it does not affect the azimuthal angle  $\Phi_p$ . However, in the experiment which we would like to reproduce [9], the proton emission angles  $\Theta_p$  and  $\Phi_p$  are defined in the ‘‘center-of-mass frame’’, which one could interpret as the cm frame of the whole process, i. e. of the incoming electron and deuteron. In this latter system, (4.14) cannot be applied because the transformation to the lab frame is not parallel to  $\mathbf{q}$ , but depends on  $\Phi_p$ . Furthermore, we checked by explicitly calculating the full triple-differential cross section in the electron-deuteron cm frame that a large discrepancy to the data exists, if  $\Theta_p$  and  $\Phi_p$  indeed refer to this frame. Thus, we assume that in [9] the hadronic variables are also defined in the *proton-neutron* cm frame.

Now all relevant kinematic relations have been determined and what remains is to calculate the amplitude  $\mathcal{A}$ .

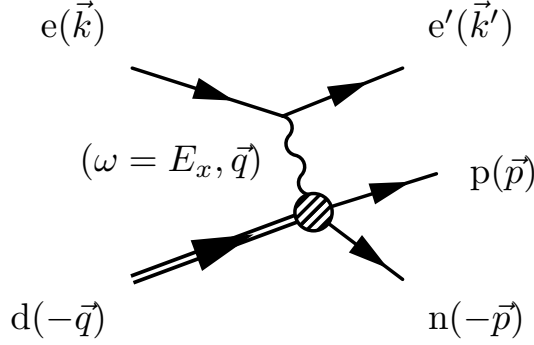


Figure 4.2: Decomposition of the scattering amplitude: The electrons are represented by the leptonic current and will be left out in all following diagrams.

### 4.1.2 Formalism

It is convenient to organize the calculation of the scattering amplitude for  $d(e, e'p)n$  as follows:  $\mathcal{A}$  can be split into a leptonic and a hadronic part (Fig. 4.2). It can be written as (see e. g. [31])

$$\mathcal{A} = l^\mu D_{\mu\nu}^{(\gamma)} J^\nu, \quad (4.18)$$

where  $l^\mu$  and  $J^\nu$  are the leptonic and hadronic currents, respectively,

$$D_{\mu\nu}^{(\gamma)} = \frac{1}{q_\rho q^\rho} \left( g_{\mu\nu} - \frac{q_\mu^{\text{lab}} q_\nu^{\text{lab}}}{q_\rho q^\rho} \right) \quad (4.19)$$

is the photon propagator and  $q_\mu^{\text{lab}} = k_\mu^{\text{lab}} - k'_\mu^{\text{lab}}$  is the transferred four-momentum.

The calculation of the hadronic current  $J^\mu$  will be carried out in the next sections. The absolute square of the amplitude includes the hadronic tensor

$$H^{\mu\nu} = (J^{\mu\dagger} J^\nu)_{\text{avg}}, \quad (4.20)$$

where the subscript “avg” refers to spin-average, and the leptonic tensor

$$L^{\mu\nu} = (l^{\mu\dagger} l^\nu)_{\text{avg}}. \quad (4.21)$$

The latter is the same for every diagram and can be calculated easily: The leptonic current reads in terms of the electron Dirac spinor  $u(\mathbf{k}^{\text{lab}})$  and the electron charge  $-e$ :

$$l^\mu = -e \bar{u}(\mathbf{k}'^{\text{lab}}) \gamma^\mu u(\mathbf{k}^{\text{lab}}). \quad (4.22)$$

It follows that

$$\begin{aligned} L^{\mu\nu} &= e^2 \frac{1}{2} \text{Tr}[\gamma^\mu (\not{k}'^{\text{lab}} + m_e) \gamma^\nu (\not{k}^{\text{lab}} + m_e)] \\ &= 2e^2 (k'^{\mu\text{lab}} k^{\nu\text{lab}} + k'^{\nu\text{lab}} k^{\mu\text{lab}} - g^{\mu\nu} (k_\rho^{\text{lab}} k'^{\rho\text{lab}} - m_e^2)). \end{aligned} \quad (4.23)$$

One can readily check that current conservation is fulfilled:

$$q_\mu^{\text{lab}} L^{\mu\nu} = 0. \quad (4.24)$$

This means that we can replace the photon propagator (4.19) by  $\frac{1}{q_\mu^2} g_{\mu\nu}$ . Hence the amplitude becomes

$$\mathcal{A} = \frac{1}{q_\nu q^\nu} l^\mu J_\mu, \quad (4.25)$$

and

$$\begin{aligned} |\mathcal{A}|^2 &= \frac{1}{(q_\rho q^\rho)^2} L^{\mu\nu} H_{\mu\nu} \\ &= \frac{2e^2}{(\omega^2 - q^2)^2} (k'^{\mu\text{lab}} J_\mu^\dagger k^{\nu\text{lab}} J_\nu + k'^{\nu\text{lab}} J_\nu k^{\mu\text{lab}} J_\mu^\dagger - (k_\mu^{\text{lab}} k'^{\mu\text{lab}} - m_e^2) J_\nu^\dagger J^\nu). \end{aligned} \quad (4.26)$$

Thus the leptonic part of the electrodisintegration process is completed. In the following Sections, the hadronic current will be determined from the various Feynman diagrams up to a given order. The cross section is then given by (4.13) and (4.26).

## 4.2 Electric Transitions at LO

The rules for calculating the hadronic current have already been derived: The Lagrangean is given in (2.29) and the Feynman rules are listed in Appendix A. In Sect. 3.2, the reverse process with a real photon was examined, and we found that for  $p \gtrsim 20$  MeV,  $E1_V$ -transitions give the dominant contribution to the cross section (see Fig. 3.8). Therefore, we first calculate electric transitions at LO.

There are three diagrams contributing at order  $Q^0$  (Fig. 4.3). All hadronic currents for electric transitions have the following structure:

$$J^\mu = ie\sqrt{Z} \frac{1}{\sqrt{8}} (N_p^\dagger \sigma^i \sigma_2 N_n^*) \epsilon_{(d)}^j J_{ij}^\mu, \quad (4.27)$$

where we have specified proton and neutron spinors  $N_{p/n}$  and thus no isospin-projectors (i. e.  $\tau$ - and  $Q$ -matrices present in (2.29)) appear; this has to be

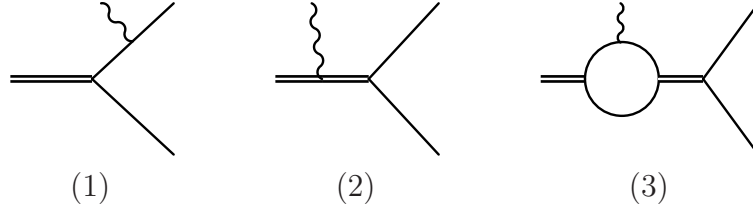


Figure 4.3: LO diagrams for electric transitions. Only the hadronic part is shown.

corrected by identifying the appropriate symmetry factors. For example, diagram (1) has only a symmetry factor 2 instead of 4 because the photon couples only to the proton. (The factor 2 comes from the dNN vertex.) Thus we find

$$J_{ij}^{0(1)} = -2y_t D_p \delta_{ij}, \quad (4.28)$$

$$\mathbf{J}_{ij}^{(1)} = J_0^{(1)} \frac{2\mathbf{p} - \mathbf{q}}{2M}, \quad (4.29)$$

where the proton propagator is given by

$$iD_p = \frac{i}{\frac{p^2}{2M} - \omega - \frac{(\mathbf{p}-\mathbf{q})^2}{2M}} = \frac{i}{-\omega + \frac{\mathbf{p}\cdot\mathbf{q}}{M} - \frac{q^2}{2M}}; \quad (4.30)$$

it should not be approximated as in (3.20) (where  $\omega = q$  for real photons), since now  $\omega$  can be of the same order as  $q^2/M$ . The second diagram gives

$$J_{ij}^{0(2)} = 2y_t D_t \delta_{ij}, \quad (4.31)$$

$$\mathbf{J}_{ij}^{(2)} = -J_0^{(2)} \frac{\mathbf{q}}{4M}, \quad (4.32)$$

with the dibaryon propagator of (2.25),

$$iD_t = \frac{M\rho_d}{2} \frac{i}{\gamma - \frac{\rho_d}{2}(\gamma^2 + p^2) + ip}. \quad (4.33)$$

Diagram (3) contains a nucleon loop, and after integrating over  $l_0$  one finds

$$\begin{aligned} J_{ij}^{0(3)} &= -2y_t D_t y_t^2 M^2 \int \frac{d^3l}{(2\pi)^3} \frac{1}{l^2 + (-p^2)} \frac{1}{(\mathbf{l} + \frac{\mathbf{q}}{2})^2 + \gamma^2} \delta_{ij} \\ &= -2y_t^3 D_t M^2 I_0^{(2)}(-p^2, \gamma^2) \delta_{ij}, \end{aligned} \quad (4.34)$$

$$\begin{aligned} \mathbf{J}_{ij}^{(3)} &= 2y_t D_t y_t^2 \frac{M}{2} \int \frac{d^3l}{(2\pi)^3} \frac{\mathbf{q} + 2\mathbf{l}}{l^2 + (-p^2)} \frac{1}{(\mathbf{l} + \frac{\mathbf{q}}{2})^2 + \gamma^2} \delta_{ij}, \\ &= 2y_t^3 D_t \frac{M}{2} \left( I_0^{(2)}(-p^2, \gamma^2) + \frac{2}{q^2} A_1(-p^2, \gamma^2) \right) \mathbf{q} \delta_{ij}. \end{aligned} \quad (4.35)$$

The integrals in (4.34) and (4.35) can be found in Appendix D (as all other loop integrals used in this work), and  $-p^2$  is understood to be  $-p^2 - i\epsilon$ , i. e.  $\sqrt{-p^2} = -ip$ , where  $p$  is the proton momentum.

To get the spin- and polarization-averaged absolute square of (4.27), we use

$$\sum (N_p^\dagger \sigma^i \sigma_2 N_n^*) (N_n^T \sigma_2 \sigma^j N_p) = \text{Tr}[\sigma^i \sigma_2 \sigma_2 \sigma^j] = 2\delta^{ij}, \quad (4.36)$$

$$\frac{1}{3} \sum \epsilon^i \epsilon^{*j} = \frac{1}{3} \delta^{ij}, \quad (4.37)$$

and find

$$(J_\mu^\dagger J_\nu)_{avg} = e^2 Z \frac{1}{12} J_\mu^{\dagger ij} J_\nu^{ij}. \quad (4.38)$$

Thus (4.26) becomes

$$|\mathcal{A}|^2 = \frac{(4\pi\alpha)^2}{(\omega^2 - q^2)^2} \frac{Z}{6} \times \left( k'^{\mu\text{lab}} J_\mu^{\dagger ij} k^{\nu\text{lab}} J_\nu^{ij} + k'^{\nu\text{lab}} J_\nu^{\dagger ij} k^{\mu\text{lab}} J_\mu^{ij} - (k_\mu^{\text{lab}} k'^{\mu\text{lab}} - m_e^2) J_\nu^{\dagger ij} J^{\nu ij} \right), \quad (4.39)$$

with the fine structure constant  $\alpha = \frac{e^2}{4\pi} \approx \frac{1}{137}$ . The result is plotted as a function of  $\Theta_p$  in Fig. 4.5, compared to the NNLO result derived in the next Section. The dependence on the proton emission angles  $\Theta_p$  and  $\Phi_p$  stems entirely from diagram (1). This diagram is responsible for the non-vanishing  $\sigma_{LT}$ - and  $\sigma_{TT}$  terms (defined in (4.16) and (4.17)) at LO; only diagrams with final-state interaction<sup>2</sup> can influence these interference terms.

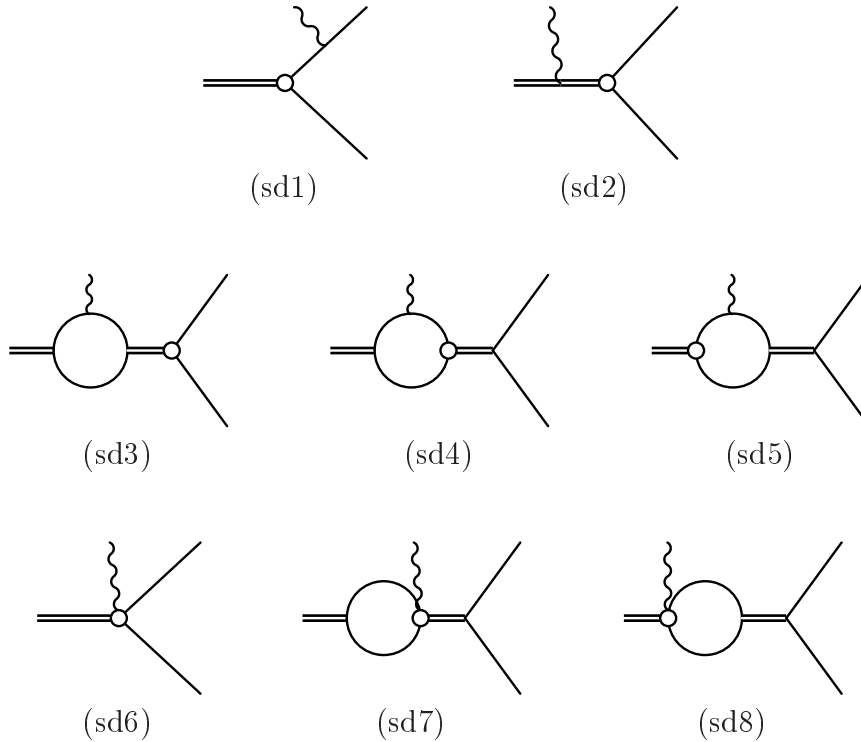
In (4.24), we showed that the leptonic tensor  $L^{\mu\nu}$  is gauge invariant. Since the Lagrangean of EFT( $\not{A}$ ) (2.29) is gauge invariant, the hadronic tensor  $H^{\mu\nu}$  must also have this property; this means that the hadronic current satisfies the continuity equation:

$$q_0^{cm} J_0 - \mathbf{q}^{cm} \cdot \mathbf{J} = 0. \quad (4.40)$$

Thus, we could have specified a certain gauge, e. g.  $\epsilon_{(\gamma)}^0 = 0$ , and calculate the zero-component of the current by employing (4.40). We chose not to use a special gauge condition but calculate  $J_0$  and  $\mathbf{J}$  directly from Feynman diagrams. This allows us to check our results with respect to gauge invariance: (4.40) is indeed fulfilled for the sum of all LO currents.

---

<sup>2</sup>We regard the coupling of a photon to a nucleon after the break-up also as final-state interaction.

Figure 4.4:  $SD$ -mixing diagrams that contribute at order  $Q^2$ .

### 4.3 Electric Transitions at NNLO: $SD$ Mixing

Next we calculate the corrections to the LO ( $Q^0$ ) result. At order  $Q$  there is no diagram; the first correction comes from the third term in the Lagrangean (2.32), which includes two derivatives and is therefore suppressed by two powers of  $Q$ . The coefficient of this term that is responsible for  $SD$  mixing has been determined in (3.12), and the corresponding Feynman rules are given in (A.6)-(A.9). Figure 4.4 shows the diagrams that contribute to the disintegration process. By simply counting powers of  $Q$ , one can estimate the size of the NNLO contribution: If  $Q/\Lambda \approx \frac{1}{3}$ , then  $SD$  mixing should contribute about  $(\frac{1}{3})^2 \approx 11\%$  of the LO terms. The error one makes by truncating the series at this order should be  $(\frac{1}{3})^3 \approx 4\%$ .

The hadronic current is again given by (4.27), with  $J_\mu$  being the sum of

the following contributions:

$$J_{ij}^{0(sd1)} = -\frac{1}{2} \frac{C_{sd}}{\sqrt{M\rho_d}} D_p \left( \mathbf{r}_i \mathbf{r}_j - \frac{1}{3} \mathbf{r}^2 \right), \quad (4.41)$$

$$\mathbf{J}_{ij}^{(sd1)} = J_0^{(sd1)} \frac{\mathbf{r}}{2M}, \quad (4.42)$$

where we have defined  $\mathbf{r} \equiv 2\mathbf{p} - \mathbf{q}$ ;

$$J_{ij}^{0(sd2)} = 2 \frac{C_{sd}}{\sqrt{M\rho_d}} D_t \left( \mathbf{p}_i \mathbf{p}_j - \frac{1}{3} \mathbf{p}^2 \right), \quad (4.43)$$

$$\mathbf{J}_{ij}^{(sd2)} = -J_0^{(sd2)} \frac{\mathbf{q}}{4M}. \quad (4.44)$$

The loop integrals in diagram (sd3) are the same as in diagram (3) of Fig. 4.3:

$$J_{ij}^{0(sd3)} = -2 \frac{C_{sd}}{\sqrt{M\rho_d}} D_t y_t^2 M^2 I_0^{(2)}(-p^2, \gamma^2) \left( \mathbf{p}_i \mathbf{p}_j - \frac{1}{3} \mathbf{p}^2 \delta_{ij} \right), \quad (4.45)$$

$$\begin{aligned} \mathbf{J}_{ij}^{(sd3)} &= 2 \frac{C_{sd}}{\sqrt{M\rho_d}} D_t y_t^2 \frac{M}{2} \left( I_0^{(2)}(-p^2, \gamma^2) + \frac{2}{q^2} A_1(-p^2, \gamma^2) \right) \\ &\quad \times \left( \mathbf{p}_i \mathbf{p}_j - \frac{1}{3} \mathbf{p}^2 \delta_{ij} \right) \mathbf{q}. \end{aligned} \quad (4.46)$$

The combination of the next two diagrams is

$$\begin{aligned} J_{ij}^{0(sd4+sd5)} &= -2 \frac{C_{sd}}{\sqrt{M\rho_d}} D_t y_t^2 M^2 \\ &\quad \times \int \frac{d^3 l}{(2\pi)^3} \left[ \frac{1}{l^2 - p^2} \frac{1}{(1 + \frac{\mathbf{q}}{2})^2 + \gamma^2} + \frac{1}{l^2 + \gamma^2} \frac{1}{(1 + \frac{\mathbf{q}}{2})^2 - p^2} \right] \\ &\quad \times \left( \mathbf{l}_i \mathbf{l}_j - \frac{1}{3} \mathbf{l}^2 \delta_{ij} \right) \\ &= -2 \frac{C_{sd}}{\sqrt{M\rho_d}} D_t y_t^2 M^2 [B_2(-p^2, \gamma^2) + B_2(\gamma^2, -p^2)] \\ &\quad \times \left( \mathbf{q}_i \mathbf{q}_j - \frac{1}{3} \mathbf{q}^2 \delta_{ij} \right), \end{aligned} \quad (4.47)$$

$$\begin{aligned}
\mathbf{J}_{ij}^{(sd4+sd5)} &= -2 \frac{C_{sd}}{\sqrt{M\rho_d}} D_t y_t^2 M^2 \frac{1}{2M} \\
&\quad \times \int \frac{d^3l}{(2\pi)^3} \left[ \frac{\mathbf{l}_i \mathbf{l}_j - \frac{1}{3} \mathbf{l}^2 \delta_{ij}}{l^2 - p^2} \frac{-\mathbf{q} - 2\mathbf{l}}{\left(1 + \frac{\mathbf{q}}{2}\right)^2 + \gamma^2} + \frac{\mathbf{l}_i \mathbf{l}_j - \frac{1}{3} \mathbf{l}^2 \delta_{ij}}{\left(1 + \frac{\mathbf{q}}{2}\right)^2 - p^2} \frac{2\mathbf{l}}{l^2 + \gamma^2} \right] \\
&= 2 \frac{C_{sd}}{\sqrt{M\rho_d}} D_t y_t^2 M \left[ \frac{1}{2} B_2(-p^2, \gamma^2) \left( \mathbf{q}_i \mathbf{q}_j - \frac{1}{3} \mathbf{q}^2 \delta_{ij} \right) \mathbf{q} \right. \\
&\quad + [A_3(-p^2, \gamma^2) - A_3(\gamma^2, -p^2)] \left( \mathbf{q}^i \delta^{jk} + \mathbf{q}^j \delta^{ik} - \frac{2}{3} \mathbf{q}^k \delta^{ij} \right) \\
&\quad \left. + [B_3(-p^2, \gamma^2) - B_3(\gamma^2, -p^2)] \left( \mathbf{q}^i \mathbf{q}^j \mathbf{q}^k - \frac{1}{3} \mathbf{q}^2 \mathbf{q}^k \delta^{ij} \right) \right]. \quad (4.48)
\end{aligned}$$

The functions  $B_2(a, b)$ ,  $A_3(a, b)$  and  $B_3(a, b)$  are defined in (D.9), (D.12) and (D.13), where the loop integrals are evaluated. Here we set  $D = 3$  because in the final result all  $\mu$ -dependence (stemming from  $D = 2$ ) drops out. The last three diagrams contribute only to the vector-component of the current:

$$\mathbf{J}_{ij,k}^{(sd6)} = \frac{C_{sd}}{\sqrt{M\rho_d}} \left( -\mathbf{p}_i \delta_{jk} + \left( -\mathbf{p}_j + \frac{1}{2} \mathbf{q}_j \right) \delta_{ik} + \frac{2}{3} \left( \mathbf{p}_k - \frac{1}{4} \mathbf{q}_k \right) \delta_{ij} \right), \quad (4.49)$$

$$\mathbf{J}_{ij,k}^{(sd7+sd8)} = \frac{C_{sd}}{\sqrt{M\rho_d}} D_t y_t^2 \frac{M}{2} [I_0^{(1)}(\gamma^2) - I_0^{(1)}(-p^2)] \left( \frac{1}{2} \mathbf{q}_j \delta_{ik} + \frac{1}{2} \mathbf{q}_i \delta_{jk} - \frac{1}{3} \mathbf{q}_k \delta_{ij} \right). \quad (4.50)$$

Again, we find that (4.40) is fulfilled, so that the NNLO amplitude is also gauge invariant. Figure 4.5 shows a comparison of the LO and NNLO results for the squared amplitude. We see that only around  $\Theta_p \approx 70^\circ$  does the NNLO amplitude differ significantly from the LO one, which becomes very small in this angular range. The smallness of the NNLO contribution is rather surprising (note that the proton momentum is as large as 78 MeV for the kinematics chosen). This means that the convergence is better than estimated and corrections beyond  $\mathcal{O}(Q^2)$  can be neglected to a good approximation.

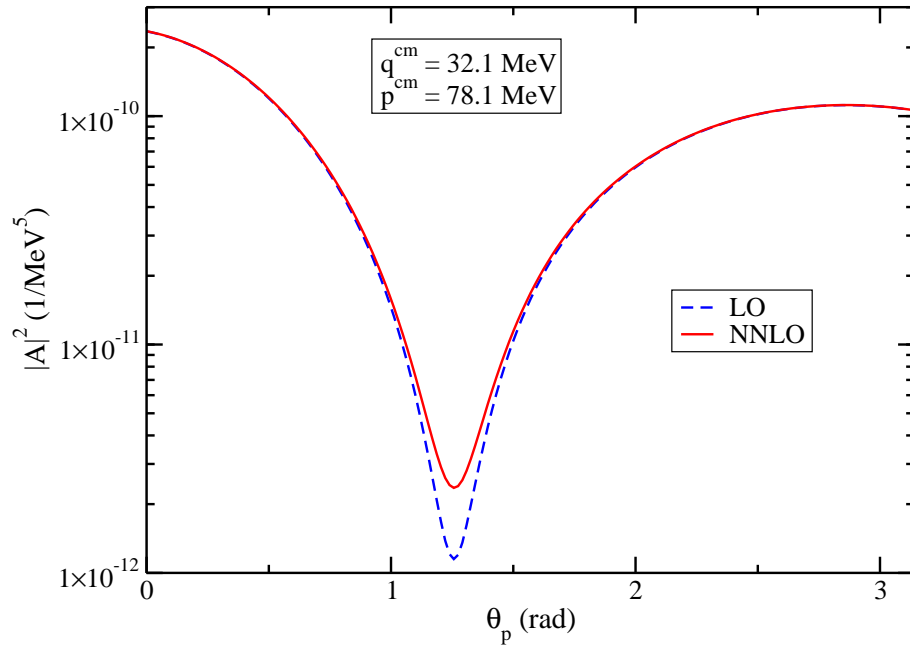


Figure 4.5: Logarithmic plot of the squared amplitude for deuteron-electrodisintegration at LO and up to NNLO, calculated at  $E_0^{\text{lab}} = 50$  MeV,  $E_e^{\text{lab}} = 41$  MeV,  $\Theta_e^{\text{lab}} = 40^\circ$ ,  $\Phi_p = 45^\circ$ .

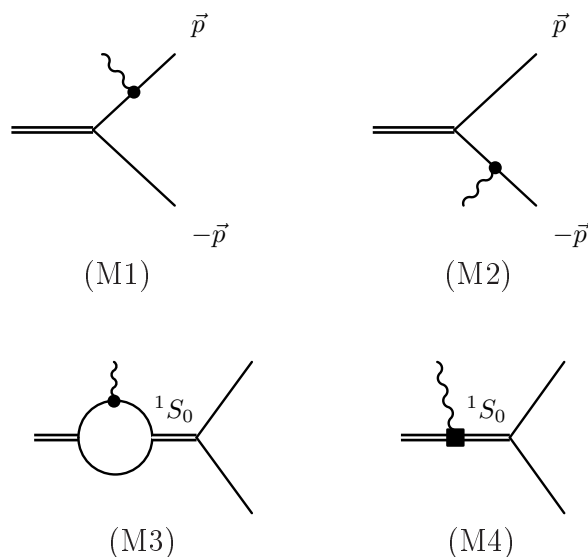


Figure 4.6: Diagrams for magnetic transitions at LO (M1-M3) and NLO (M4).

## 4.4 Magnetic Transitions up to NLO

In Sect. 3.2, magnetic transitions were found to give a significant contribution to the cross section for  $np \rightarrow d\gamma$  at very low energies. Now the corresponding amplitude for the disintegration process is calculated. The relevant parts of the Lagrangean are given in (2.30) and (2.33), and the Feynman rules in (A.2) and (A.11). The LO and NLO diagrams are depicted in Fig. 4.6.

The hadronic currents for these diagrams can be written in the form

$$J^k = e\sqrt{Z}\epsilon^{ijk}\epsilon_{(d)}^i\frac{1}{\sqrt{8}}(N_p^\dagger\sigma_2N_n^*)J^j. \quad (4.51)$$

Thus, averaging over the deuteron polarizations and summing over the nucleon spins gives

$$\begin{aligned} \left(J_k^\dagger J_n\right)_{\text{avg}} &= \frac{1}{3}\sum e^2\frac{Z}{8}\epsilon^{ijk}\epsilon_{(d)}^{*i}(N_n^T\sigma_2N_p)J^{\dagger j}\epsilon^{lmn}\epsilon_{(d)}^l(N_p^\dagger\sigma_2N_n^*)J^m \\ &= e^2\frac{Z}{12}(\delta^{jm}\delta^{kn}-\delta^{km}\delta^{jn})J^{\dagger j}J^m, \end{aligned} \quad (4.52)$$

and the squared amplitude is

$$|\mathcal{A}|^2 = \frac{(4\pi\alpha)^2}{(\omega^2 - q^2)^2} \frac{Z}{6} (\delta^{jm}\delta^{kn} - \delta^{km}\delta^{jn}) \\ \times \left( \mathbf{k}^{n\text{lab}} J^{\dagger j} \mathbf{k}^{k\text{lab}} J^m + \mathbf{k}^{k\text{lab}} J^m \mathbf{k}^{n\text{lab}} J^{\dagger j} + (k_\mu^{\text{lab}} k'^{\mu\text{lab}} - m_e^2) J^{\dagger j} J^m \delta^{kn} \right). \quad (4.53)$$

For the LO diagrams we find

$$J^{j(M1)} = -y_t D_p \frac{\kappa_1}{M} \mathbf{q}^j, \quad (4.54)$$

$$J^{j(M2)} = -y_t D_n \frac{\kappa_1}{M} \mathbf{q}^j, \quad (4.55)$$

$$J^{j(M3)} = -2y_t D_s y_s^2 \kappa_1 M I_0^{(2)}(-p^2, \gamma^2) \mathbf{q}^j. \quad (4.56)$$

The propagator for the neutron (with momentum  $-\mathbf{p}$ ),

$$iD_n = \frac{i}{-\omega - \frac{\mathbf{p}\cdot\mathbf{q}}{M} - \frac{q^2}{2M}}, \quad (4.57)$$

differs from  $D_p$  defined in (4.30) by a minus-sign in the denominator, and the dibaryon in the intermediate state is now in the  ${}^1S_0$  state, with the propagator  $D_s$  given by (2.23):

$$iD_s = \frac{Mr_0}{2} \frac{i}{\frac{1}{a_0} - \frac{r_0}{2} p^2 + ip}. \quad (4.58)$$

The loop integral  $I_0^{(2)}(a, b)$  is calculated in (D.2).

The only NLO contribution is proportional to  $L_1$ , which was determined in Sect. 3.2.1. The corresponding current is

$$J^{j(M4)} = -2y_s D_s \frac{L_1}{M\sqrt{r_0\rho_d}} \mathbf{q}^j. \quad (4.59)$$

In Fig. 4.7 we show  $|\mathcal{A}|^2$  for magnetic transitions at LO and NLO. We discover the same feature as for the neutron capture: The vertex where a magnetic photon couples to a dibaryon reduces the amplitude largely, although it is formally NLO. Compared to the electric amplitude (Fig. 4.5), the magnetic one is much smaller (except for the vicinity of  $\Theta_p = 70^\circ$ ) in this energy regime. At smaller energies, magnetic transitions become dominant (as demonstrated in Fig. 4.8). This is what we expected from the  $np \rightarrow d\gamma$  process. It is important to note that the only angular dependence in the magnetic amplitude comes from the  $\mathbf{p}\cdot\mathbf{q}$ -terms in the nucleon propagators. Thus there is no  $\Phi_p$ -dependence, and therefore magnetic transitions at this order do not contribute to the  $\sigma_{LT}$  and  $\sigma_{TT}$  interference terms defined in (4.16) and (4.17) (see also Sect. 5.2).

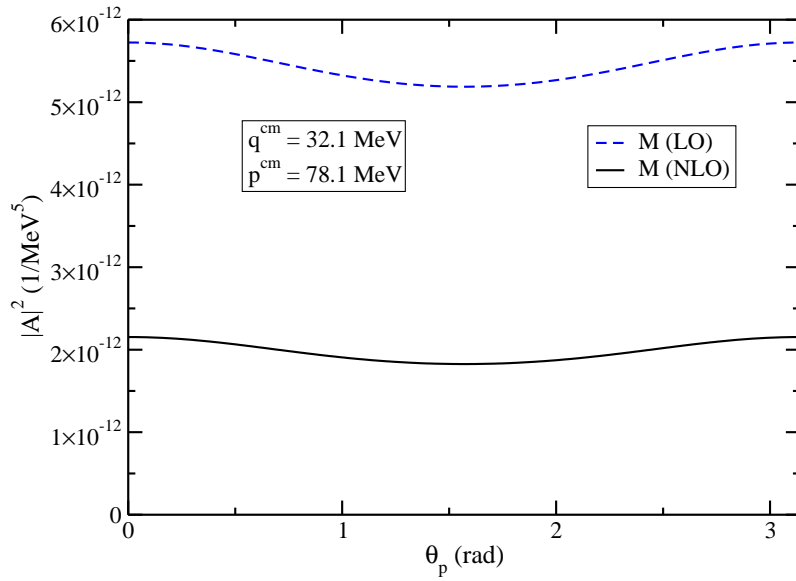


Figure 4.7:  $\Theta_p$ -dependence of  $|\mathcal{A}|^2$  for magnetic transitions at LO and NLO for  $E_0^{\text{lab}} = 50$  MeV,  $E_e^{\text{lab}} = 41$  MeV,  $\Theta_e^{\text{lab}} = 40^\circ$ ,  $\Phi_p = 45^\circ$ .

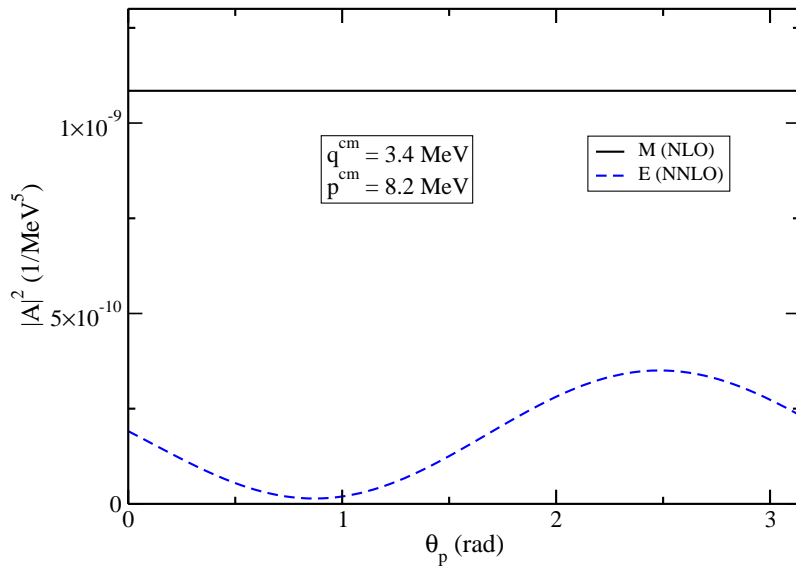


Figure 4.8: Comparison of magnetic and electric contributions at very low energies:  $E_0^{\text{lab}} = 5$  MeV,  $E_e^{\text{lab}} = 2.7$  MeV,  $\Theta_e^{\text{lab}} = 40^\circ$ ,  $\Phi_p = 45^\circ$ .

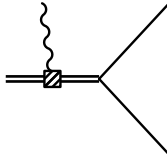


Figure 4.9: One of the  $N^3\text{LO}$  diagrams: The shaded square represents the operator proportional to  $C_Q$  (Feynman rule (A.10)).

## 4.5 Other Possible Contributions

The cross section for deuteron-electrodisintegration has been calculated in the previous sections up to NNLO for electric transitions, and up to NLO for magnetic transitions. The estimated error is about 4 % and 11 %, respectively, of the LO contributions. This should be sufficiently accurate for a meaningful comparison to data (see Chapter 5). What is more, the convergence for electric transitions seems to be even better than estimated, because the  $SD$  mixing terms (NNLO) were found to give a very small contribution even at relatively high momentum transfers. For magnetic transitions there is a large contribution at NLO; but since we are mainly interested in the intermediate momentum range between 30 and 100 MeV where electric transitions are dominant, we can neglect higher order terms here as well.

Nonetheless, we briefly discuss some higher-order contributions to show that they are indeed negligible. First, one might think of the  $C_Q$ -term (2.32) which was found to have a considerable impact on the quadrupole form factor (see Sect. 3.1.3). It enters at  $N^3\text{LO}$ , and the corresponding diagram is shown in Fig. 4.9. The current that is included in (4.27) is

$$J_{ij}^0 = -2y_t D_t \frac{C_Q}{M\rho_d} \left( \mathbf{q}_i \mathbf{q}_j - \frac{1}{3} \mathbf{q}^2 \delta_{ij} \right). \quad (4.60)$$

However, it turns out that its contribution to the cross section is negligible. For example, for the kinematics chosen in Fig. 4.5, the difference between the NNLO result and the one including (4.60) is less than 0.5 % even at the minimum around  $\Theta_p = 70^\circ$ . The reason why this term is important for the quadrupole form factor but not for  $e + d \rightarrow e' + p + n$  is that in the latter process, there are not only two  $SD$  mixing diagrams (sd4 and sd5 in Fig. 4.4) as for  $F_Q$  (Fig. 3.4 a,b), but several other diagrams that give a larger contribution. Not only is the full triple-differential cross section practically unchanged by including (4.60), but its contribution to the interference terms  $\sigma_{LT}$  and  $\sigma_{TT}$  is even vanishing, since (4.60) is independent of  $\Phi_p$ .

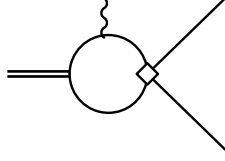


Figure 4.10: An example for a diagram including  $P$ -wave final state interaction. The square denotes a  $P$ -wave operator of (4.61).

Another set of diagrams contributing to electric transitions includes  $P$ -wave nucleon-nucleon final state interactions, described by the Lagrangean [25]

$$\begin{aligned} \mathcal{L}_P = & \left( C^{(^3P_0)} \delta^{xy} \delta^{wz} + C^{(^3P_1)} [\delta^{xw} \delta^{yz} - \delta^{xz} \delta^{yw}] \right. \\ & \left. + C^{(^3P_2)} [2\delta^{xw} \delta^{yz} + 2\delta^{xz} \delta^{yw} - \frac{4}{3} \delta^{xy} \delta^{wz}] \right) \\ & \times (N^T \mathcal{O}_{xy}^{(P)} N)^\dagger (N^T \mathcal{O}_{wz}^{(P)} N), \end{aligned} \quad (4.61)$$

with

$$\mathcal{O}_{ij}^{(P)} = \overleftarrow{\mathbf{D}}_i P_j^{(P)} - P_j^{(P)} \overrightarrow{\mathbf{D}}_i, \quad (4.62)$$

and the projector on the iso-triplet, spin-triplet channel is

$$P_i^{(P)} = \frac{1}{\sqrt{8}} \sigma_2 \sigma_i \tau_2 \tau_3. \quad (4.63)$$

One example of a diagram arising from  $\mathcal{L}_P$  (4.61) is depicted in Fig. 4.10. Although there are only two derivatives involved (like in the  $SD$  diagrams of Fig. 4.4), it enters at order  $Q^3$ . The reason is that there are no fine-tuned high-energy scales in the  $P$ -channel, so the naturalness assumption tells us that the coefficients  $C^{(^3P_i)}$  scale as  $Q^0$ . This was confirmed in Ref. [25] by matching the  $P$ -wave phase shifts for NN scattering to the values given by the Nijmegen phase shift analysis. In contrast, the presence of an unnaturally large length scale must be taken into account for  $S$ -channel scattering (Chapter 2).  $SD$  mixing therefore enters at a lower order than  $P$ -wave interactions, although both involve two derivatives of nucleon fields. Thus we do not calculate the  $P$ -wave diagrams explicitly but trust our power counting estimation which states that they contribute even less than  $SD$  mixing.

An example for a relativistic effect neglected in our calculation is the

“spin-orbit” interaction, represented by the following Lagrangean [35]:

$$\begin{aligned} \mathcal{L}_{so} = & N^\dagger i \left[ \left( 2\kappa_0 - \frac{1}{2} \right) + \left( 2\kappa_1 - \frac{1}{2} \right) \tau_3 \right] \\ & \times \frac{e}{8M^2} \boldsymbol{\sigma} \cdot (\mathbf{D} \times \mathbf{E} - \mathbf{E} \times \mathbf{D}) N, \end{aligned} \quad (4.64)$$

where  $\mathbf{E} = -\nabla A_0 - \partial_0 \mathbf{A}$  is the electric field. This term is suppressed by  $Q/M$  relative to the magnetic-field term in  $\mathcal{L}_N$  (2.30). The corresponding Feynman rule (neglecting the  $\kappa_0$ -term) is:

$$\begin{aligned} \text{---} \overset{p^q}{\circlearrowleft} \text{---} \overset{p'}{\circlearrowleft} \text{---} = & - \left( 2\kappa_1 - \frac{1}{2} \right) \tau_3 \frac{e}{8M^2} \epsilon^{ijk} \sigma^i (\mathbf{p} + \mathbf{p}')^j \mathbf{q}^k A_0 \\ & + \left( 2\kappa_1 - \frac{1}{2} \right) \tau_3 \frac{e}{8M^2} \epsilon^{ijk} \sigma^i (\mathbf{p} + \mathbf{p}')^j \omega A^k. \end{aligned} \quad (4.65)$$

The diagrams for the spin-orbit interaction are similar to the ones for magnetic transitions (Fig. 4.6), with only the photon-nucleon vertex given by (4.65). They are depicted in Fig. 4.11. The vector-component of the hadronic current has the same structure as (4.51), and the zero-component can be written as

$$J^0 = e\sqrt{Z} \epsilon^{ijk} \epsilon_{(d)}^i \frac{1}{\sqrt{8}} (N_p^\dagger \sigma_2 N_n^*) J^{jk}. \quad (4.66)$$

The contributions of the different diagrams are:

$$J_{jk}^{0(so1)} = -y_t D_p \frac{2\kappa_1 - \frac{1}{2}}{4M^2} (2\mathbf{p} - \mathbf{q})^j \mathbf{q}^k, \quad (4.67)$$

$$J_j^{(so1)} = y_t D_p \frac{2\kappa_1 - \frac{1}{2}}{4M^2} (2\mathbf{p} - \mathbf{q})^j \omega, \quad (4.68)$$

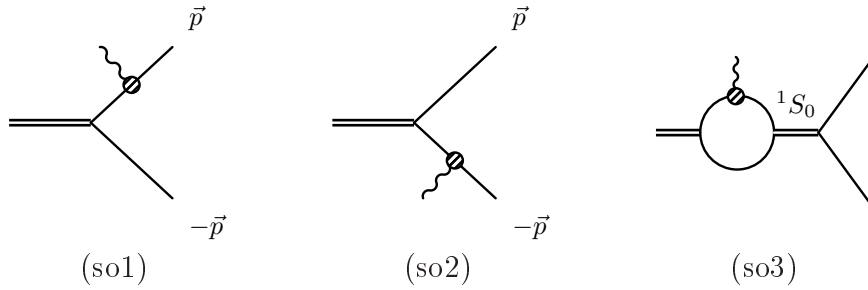
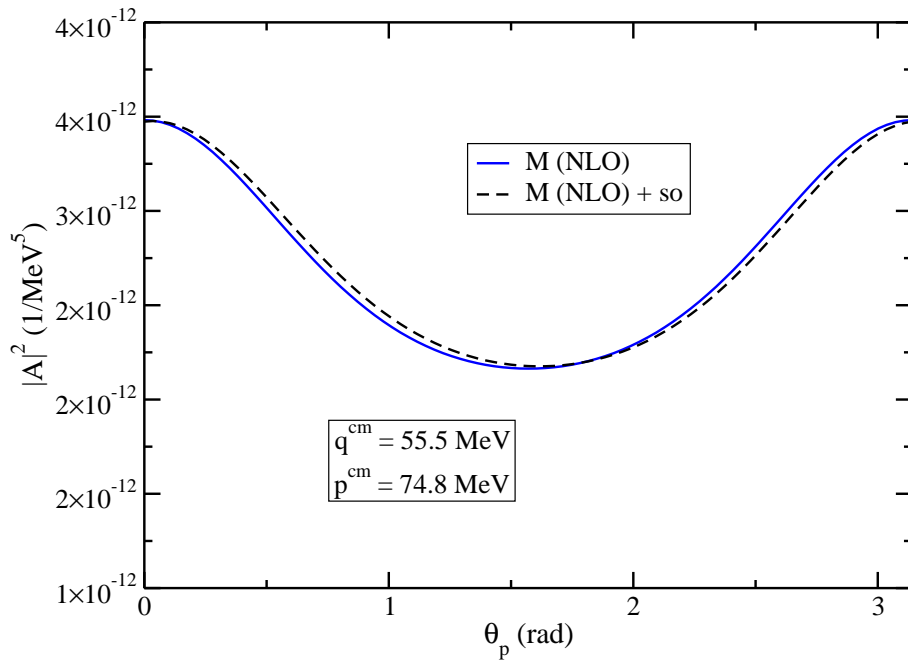
$$J_{jk}^{0(so2)} = -y_t D_n \frac{2\kappa_1 - \frac{1}{2}}{4M^2} (-2\mathbf{p} - \mathbf{q})^j \mathbf{q}^k, \quad (4.69)$$

$$J_j^{(so2)} = y_t D_n \frac{2\kappa_1 - \frac{1}{2}}{4M^2} (-2\mathbf{p} - \mathbf{q})^j \omega, \quad (4.70)$$

$$J_{jk}^{0(so3)} = 2y_t D_s y_s^2 \frac{2\kappa_1 - \frac{1}{2}}{4} \left( I_0^{(2)}(-p^2, \gamma^2) + \frac{2}{q^2} A_1(-p^2, \gamma^2) \right) \mathbf{q}^j \mathbf{q}^k, \quad (4.71)$$

$$J_j^{(so3)} = -2y_t D_s y_s^2 \frac{2\kappa_1 - \frac{1}{2}}{4} \left( I_0^{(2)}(-p^2, \gamma^2) + \frac{2}{q^2} A_1(-p^2, \gamma^2) \right) \mathbf{q}^j \omega. \quad (4.72)$$

In Fig. 4.12 we see that these terms give only a small correction to the NLO result for magnetic transitions, as expected. Although the spin-orbit terms are  $\Phi_p$ -dependent, they are so small in the energy range of interest (note that magnetic transitions themselves are very small here) that their contribution to the  $LT$  interference term is definitely negligible.

Figure 4.11: Diagrams representing the spin-orbit interaction given by  $\mathcal{L}_{so}$ .Figure 4.12: Correction to the NLO magnetic transitions from spin-orbit coupling for  $E_0^{\text{lab}} = 85$  MeV,  $E_e^{\text{lab}} = 76$  MeV,  $\Theta_e^{\text{lab}} = 40^\circ$ ,  $\Phi_p = 45^\circ$ .

# Chapter 5

## Results and Discussion

The calculation of the triple-differential cross section for deuteron-electrodisintegration was carried out in the previous Chapter. Now we compare the results to data taken at S-DALINAC [9, 36] and to potential model calculations. The latter have been performed by H. Arenhövel et al., using a Bonn  $r$ -space potential and including meson exchange currents, isobar configurations, and (in our case negligible) relativistic effects [8, 36, 37]. First, we look at the energy- and angular dependence of the triple differential cross section, and then at its decomposition into different structure functions, where a discrepancy between model calculations and data was reported.

### 5.1 Triple-Differential Cross Section

First, a few notes on the kinematics used in [9] should be made. At the end of Sect. 4.1.1, we already argued that the “center-of-mass” frame to which the hadronic variables refer should be the cm frame of the outgoing proton and neutron, and not that of the whole  $e+d \rightarrow e'+p+n$  process. Another question occurred regarding the frame in which the transferred energy  $E_X$  is defined in the experiment. In [9],  $E_X$  is said to be obtained “after transformation to the center-of-mass system”, but we are in continuing discussions with the authors about this. To motivate this issue, the triple-differential cross section as a function of  $\Theta_p$  is shown in Fig. 5.1 (this quantity will be discussed in more detail below). Good agreement with data and with the result of the potential-model calculation mentioned above is observed only if  $E_X$  refers to the lab frame;  $E_X^{\text{cm}} = 9$  MeV would correspond to  $E_X^{\text{lab}} = 10.6$  MeV (where the cross section is smaller, see below), and the resulting curve would deviate largely from the data. We therefore interpret  $E_X$  in [9] as  $E_X^{\text{lab}}$ , defined in the rest frame of the target deuteron.

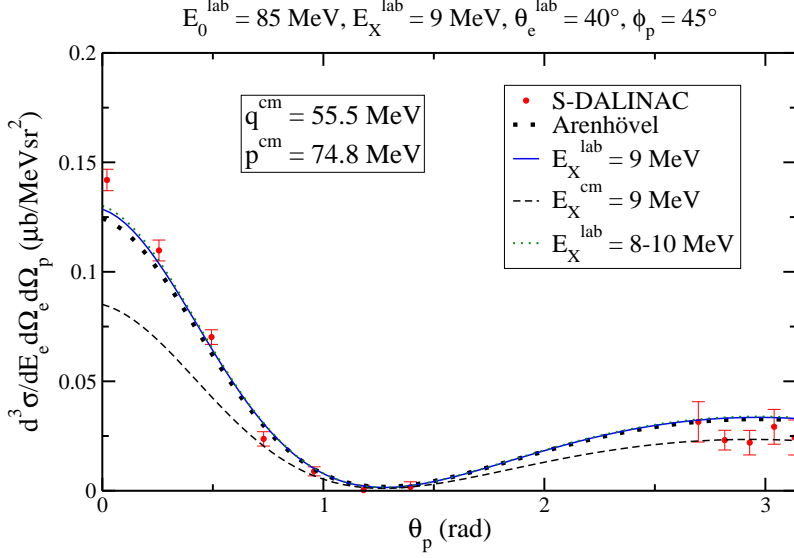


Figure 5.1: The triple-differential cross section for different values of  $E_X$ , compared to data and to Arenhövel’s result: The solid line is the result for  $E_X^{\text{lab}} = 9 \text{ MeV}$ , while dashed line refers to  $E_X^{\text{cm}} = 9 \text{ MeV}$  (which corresponds to  $E_X^{\text{lab}} = 10.6 \text{ MeV}$ ). The dotted curve is the double-differential cross section per MeV, obtained by integrating between  $E_X^{\text{lab}} = 8$  and  $10 \text{ MeV}$ ; the difference to the solid line is almost not visible. The other kinematic parameters are:  $E_0^{\text{lab}} = 85 \text{ MeV}$ ,  $\Theta_e^{\text{lab}} = 40^\circ$ ,  $\Phi_p = 45^\circ$ .

A second issue is demonstrated in Fig. 5.1: In the experiment, the double-differential cross section, integrated over an  $E_X$ -range of 2 MeV, was measured. Since the result should be twice as large as the calculated triple-differential one, we assume that the data have been divided by a factor of two; thus we compare the triple-differential cross section for a fixed value of  $E_X^{\text{lab}}$  to the double-differential one *per MeV*. The difference between integrating over the 2 MeV-range and taking the mean value of  $E_X^{\text{lab}}$  is irrelevant, as shown in the plot, and will be neglected in the following.

Now we examine the energy dependence of the triple-differential cross section for fixed angles. In Fig. 5.2, it is shown as a function of the transferred energy  $E_X^{\text{lab}}$  for two different incoming electron energies  $E_0^{\text{lab}}$ . Of course,  $E_X^{\text{lab}}$  must exceed a certain threshold energy, so that the deuteron can break up into two nucleons. This minimal value is formally determined by the

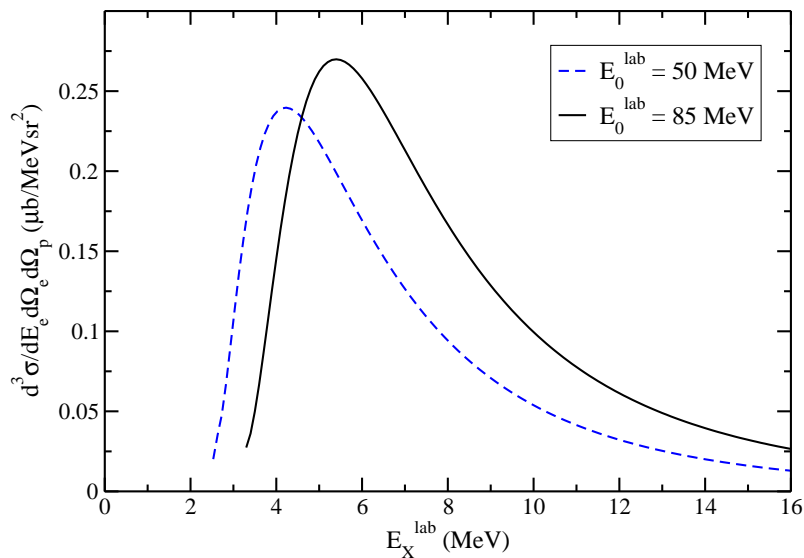


Figure 5.2: Energy dependence of the triple-differential cross section for fixed angles  $\Theta_e^{\text{lab}} = 40^\circ$  and  $\Theta_p = 0^\circ$ .

requirement that the proton momentum  $p^{\text{cm}}$  (4.5) is real, i. e.

$$(\omega - B)M + q^2 \frac{M}{2M_d} \geq 0. \quad (5.1)$$

This is fulfilled for  $E_X^{\text{lab}} \geq 2.53$  MeV at  $E_0^{\text{lab}} = 50$  MeV, and for  $E_X^{\text{lab}} \geq 3.10$  MeV at  $E_0^{\text{lab}} = 85$  MeV. Above the threshold, the cross section increases rapidly and reaches a maximum whose location is shifted to higher  $E_X^{\text{lab}}$  at growing  $E_0^{\text{lab}}$ . In the energy range of interest,  $E_X^{\text{lab}} > 8$  MeV, both curves in Fig. 5.2 fall monotonically and can be approximated by a straight line within a 2 MeV interval. (This is, of course, the reason why integrating over the interval and multiplying by the mean value gives practically the same result.)

A comparison of our results to the data and to the potential model calculation mentioned above is shown in the first part of Fig. 5.3 for  $E_0^{\text{lab}} = 50$  MeV and  $E_X^{\text{lab}} = 9$  MeV (all measurements were carried out at an electron scattering angle  $\Theta_e^{\text{lab}} = 40^\circ$ ). The curve denoted by “EFT” is the sum of the contributions of electric transitions up to NNLO and magnetic transitions up to NLO, as calculated in the previous chapter. The EFT( $\not{\pi}$ ) result agrees with H. Arenhövel’s very well. Moreover, the data are reproduced reasonably well.

In the second graph of Fig. 5.3, a decomposition of the different contributions is shown. The LO electric transitions are dominant for almost all values

of  $\Theta_p$ ; only in the region around the minimum at about  $\Theta_p = 70^\circ$ , NNLO contributions and magnetic transitions play a significant role (cf. Fig. 4.5). The fact that the LO calculation reproduces both data and potential model results so well is very interesting: It means that by taking into account only minimal coupling of photons to nucleon- and dibaryon fields, the disintegration process can be described highly accurately within EFT( $\not{\pi}$ ). The reason is that SD mixing, being the only correction up to NNLO, contributes less than estimated by naive power counting, as discussed already in Sect. 4.3. This good convergence allows us to be confident that our results are reliable, since less well-known short-distance contributions play a very minor role.

The corresponding plots for  $E_0^{\text{lab}} = 85$  MeV are depicted in Fig. 5.4. Here additional data at large  $\Theta_p$  are available; a small deviation from the theoretical predictions is not very significant since the curves lie more or less within the error bars. Again EFT( $\not{\pi}$ ) and potential model results match very well, and the LO contribution dominates to the same extent as in Fig. 5.3. This is not surprising, because the size of the  $SD$  diagrams in Sect. 4.3 is governed by the proton momentum  $p^{\text{cm}}$  (since it is larger than  $q^{\text{cm}}$ ), which is even smaller for  $E_0^{\text{lab}} = 85$  MeV (see insets in Figs. 5.3 and 5.4).

Even at a relatively large energy transfer of  $E_X^{\text{lab}} = 15$  MeV, the accord of our results with Arenhövel's and with data is rather good (Fig. 5.5). This is astonishing, as for external momenta as large as  $p^{\text{cm}} = 106$  MeV, our theory should reach the limit of applicability. However, it demonstrates once again that the NNLO terms are smaller than estimated. The good convergence in EFT( $\not{\pi}$ ) – even for momenta close to the breakdown scale – was found also in other applications, e. g. in the three-nucleon sector (see [18]).

If one takes a closer look at Fig. 5.5, one sees both a slightly more pronounced deviation from the potential model result (especially at large  $\Theta_p$ ), and a larger NNLO contribution around  $\Theta_p = 70^\circ$ , compared to Fig. 5.4. This is what one expects qualitatively, but not to such a small degree. Additional plots for  $E_0^{\text{lab}} = 85$  MeV and  $E_X^{\text{lab}} = 11$  and 13 MeV are presented in Fig. 5.6; the agreement is as good as in the plots shown above.

So far, we observed relatively good agreement of EFT( $\not{\pi}$ ) predictions and data, but a closer look at the presented plots already reveals some discrepancies. These are elaborated in the more detailed analysis of the next Section.

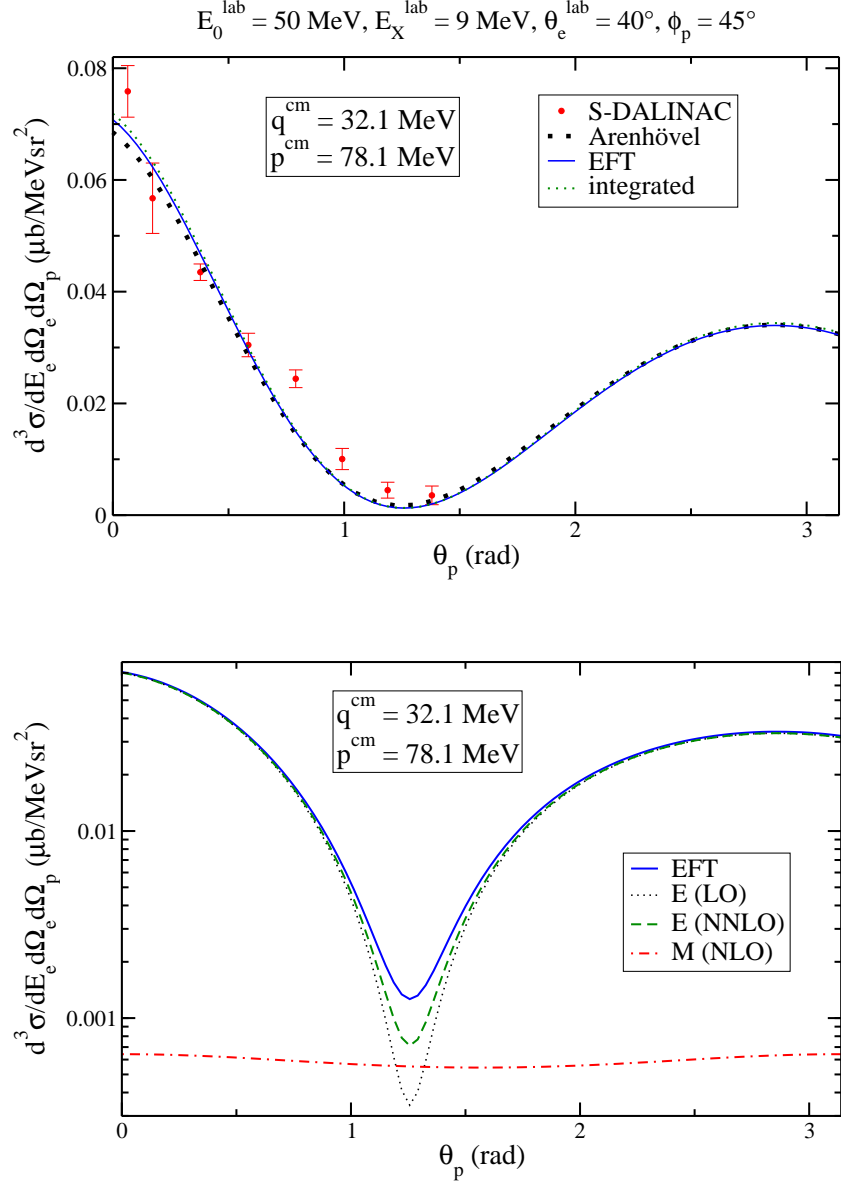


Figure 5.3: In the upper part, the result calculated in the previous Chapter (denoted by EFT) is compared to data and to H. Arenhövel's calculations. The lower graph compares the different contributions in our calculation: electric transitions up to LO and NNLO respectively, and magnetic transitions up to NLO.

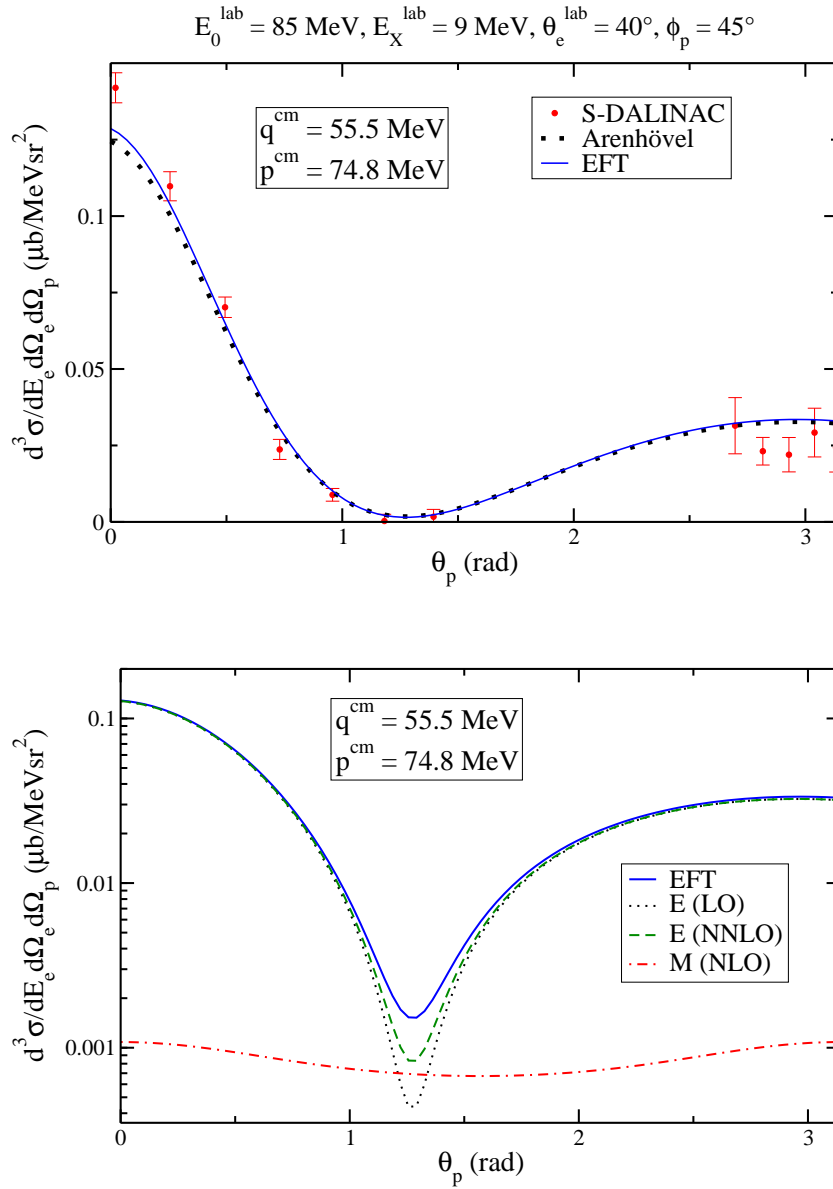


Figure 5.4: Comparison of our result to H. Arenhövel's and to data (upper graph), and the decomposition into the different contributions (lower graph), now for a higher electron energy than in Fig. 5.3.

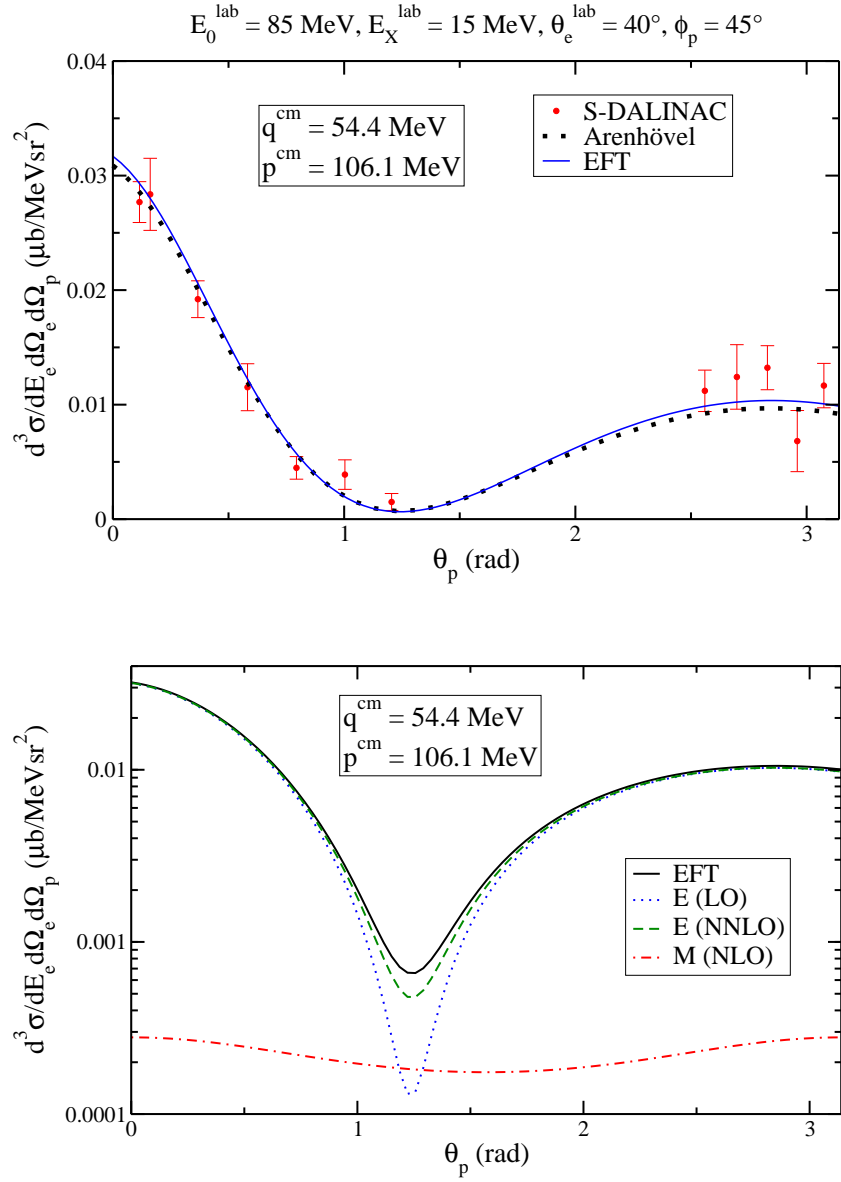


Figure 5.5: The same plots as in Fig. 5.4, but for a higher energy transfer  $E_X^{\text{lab}} = 15 \text{ MeV}$ .

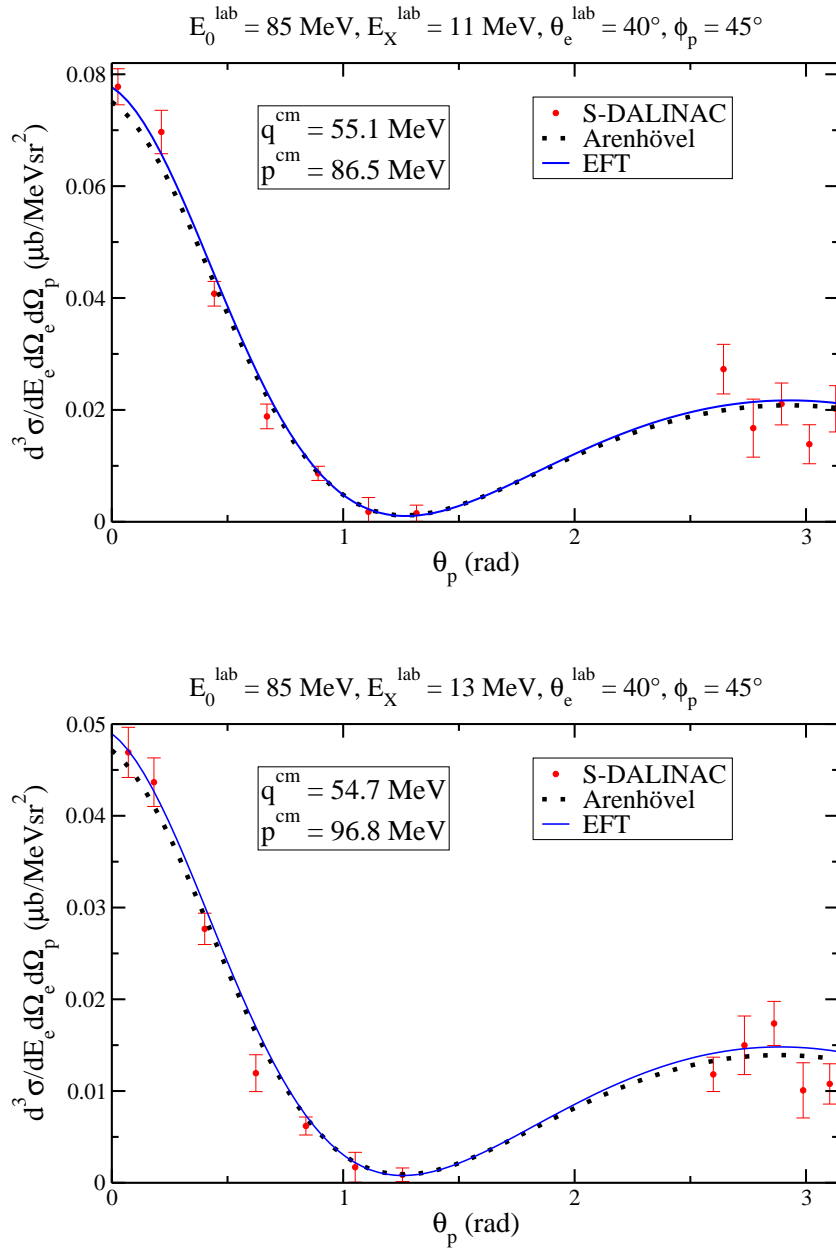


Figure 5.6: The same plots as in the upper parts of Figs. 5.4 and 5.5, but for  $E_X^{\text{lab}} = 11$  and  $13$  MeV, respectively.

## 5.2 Decomposition into Different Structure Functions

The main goal of the experiment [9] was a decomposition of the contributions of different structure functions, introduced in (4.14)-(4.17): the longitudinal-plus-transverse (L+T) cross section and the LT- and TT-interference parts. However,  $\sigma_{TT}$  is obtained by a subtraction of large numbers measured at different  $\Phi_p$  (see (4.17)); the uncertainties of the data turned out to be too large for a meaningful comparison to theory. Studying the interference terms provides information about the impact of final-state interaction, since only diagrams with final-state interaction can be  $\Phi_p$ -dependent. The contributions of the L+T, LT and TT terms are shown separately in Figs. 5.7 - 5.10, again compared to data (available only for  $\sigma_{L+T}$  and  $\sigma_{LT}$ ) and to the potential-model result, for  $E_0^{\text{lab}} = 85$  MeV and four different values of  $E_X^{\text{lab}}$ .

All curves and data are normalized to  $d^3(\sigma_L + \sigma_T)/(dE_e d\Omega_e d\Omega_p)$  at  $\Theta_p = 0^\circ$  to make the comparison independent of the absolute normalization of the data.<sup>1</sup> A general observation is that  $\sigma_L + \sigma_T$  is the dominant part, whereas  $\sigma_{LT}$  and  $\sigma_{TT}$  are one and two orders of magnitude smaller, respectively. However, the interference terms become more relevant with increasing energy transfer; this reflects the growing impact of final-state interaction.

The results of taking into account only LO electric transitions are also shown in each diagram. The degree to which they dominate over other contributions – already discussed in the previous Section – is even more striking for  $\sigma_{LT}$ . Magnetic transitions do not contribute at all to the interference cross sections, since the amplitude calculated in Sect. 4.4 is independent of  $\Phi_p$  (see discussion in Sect. 4.4). The impact of  $SD$  mixing is slightly increasing with  $E_X^{\text{lab}}$ , but small for  $\sigma_L + \sigma_T$  and  $\sigma_{TT}$  and almost negligible for  $\sigma_{LT}$ .

Generally speaking, our results are again in good agreement with those of H. Arenhövel; especially  $\sigma_{LT}$  is essentially identical in both calculations. Only in the very small quantity  $\sigma_{TT}$  can a significant deviation be detected. The accordance of  $\sigma_{LT}$  with the data, however, is considerably worse; this is examined in more detail in the following.

---

<sup>1</sup>The error of the value to which the data are normalized has been taken into account in all error bars.

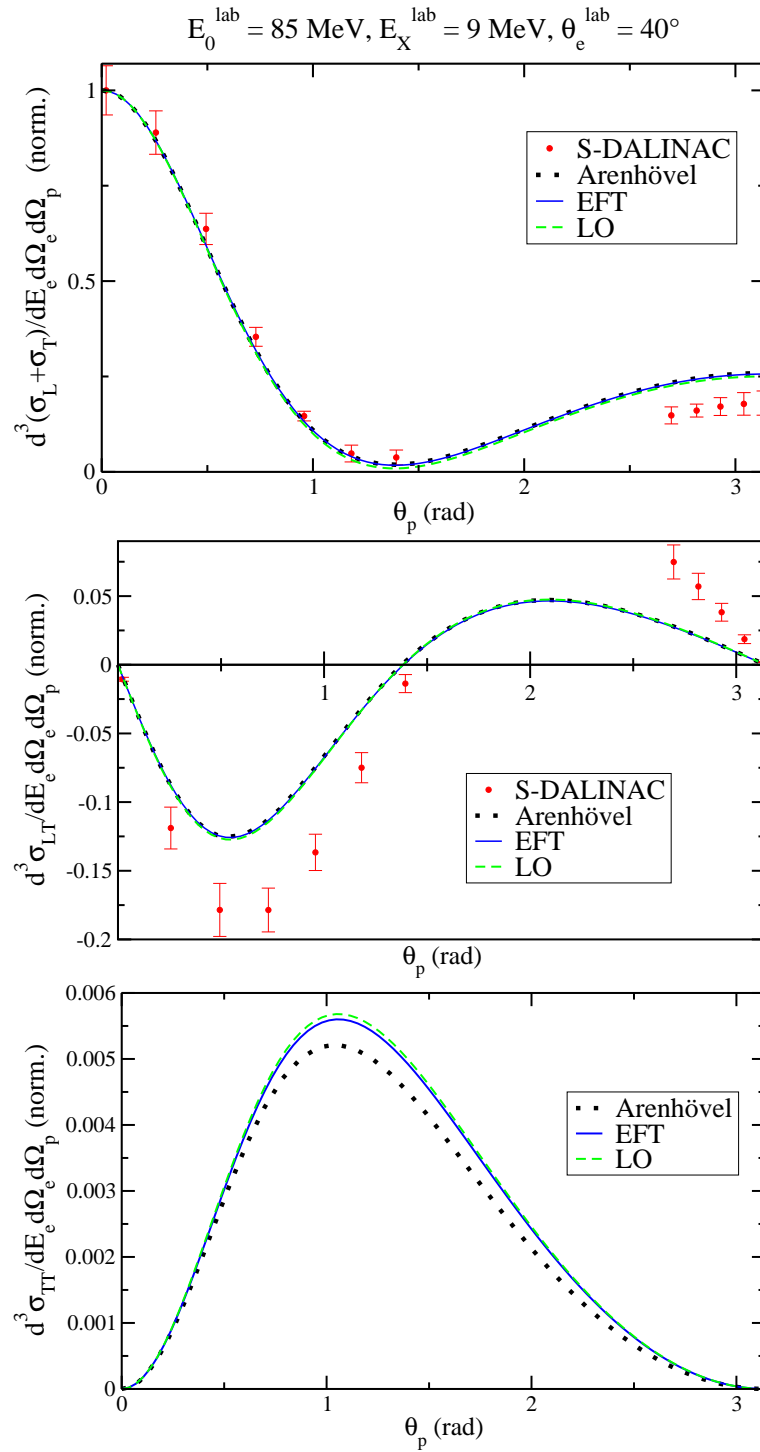
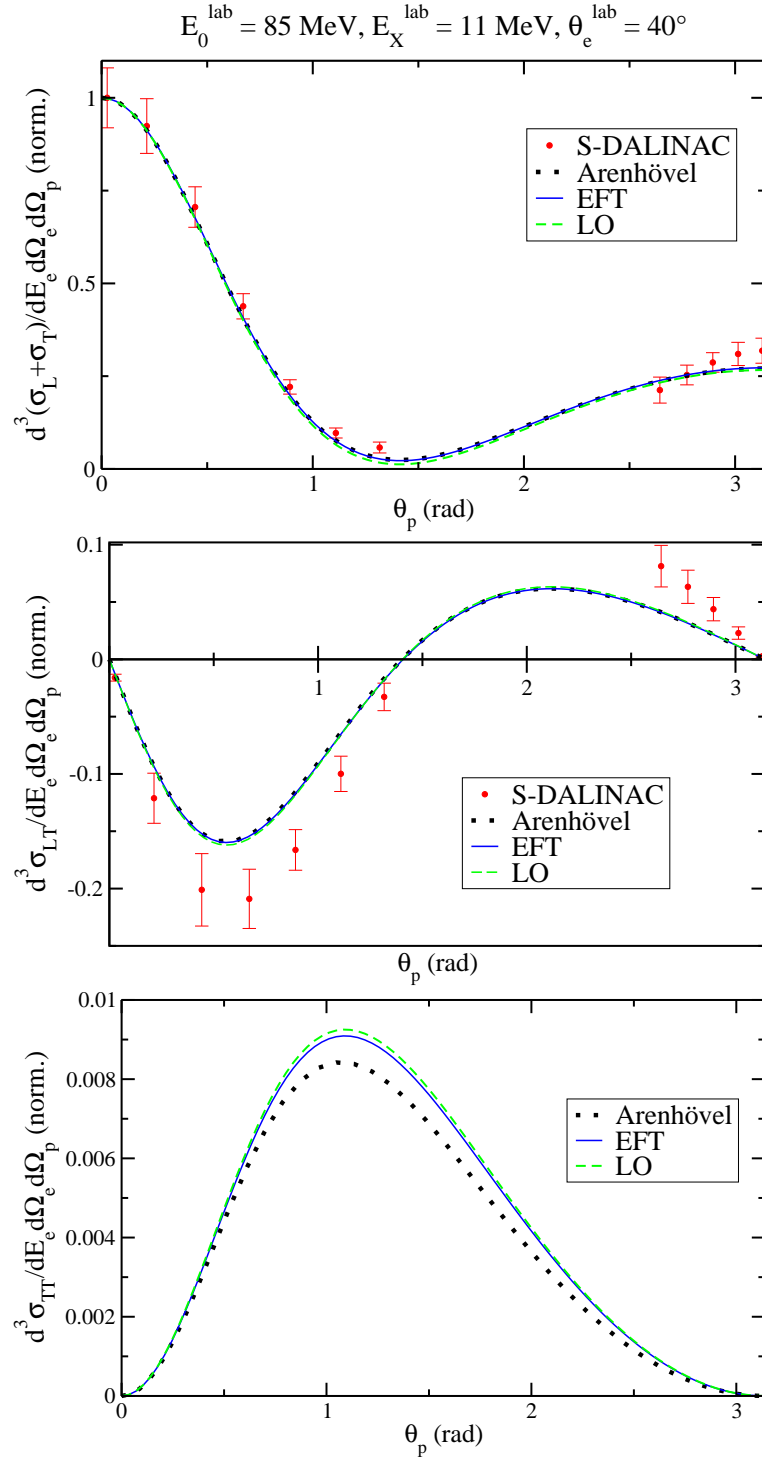


Figure 5.7: Decomposition of the triple-differential cross section into longitudinal-plus-transverse (L+T), LT and TT parts for  $E_X^{\text{lab}} = 9 \text{ MeV}$ . For the TT interference cross section, no data are available.

Figure 5.8: The same plots as in Fig. 5.7, but for  $E_X^{\text{lab}} = 11 \text{ MeV}$ .

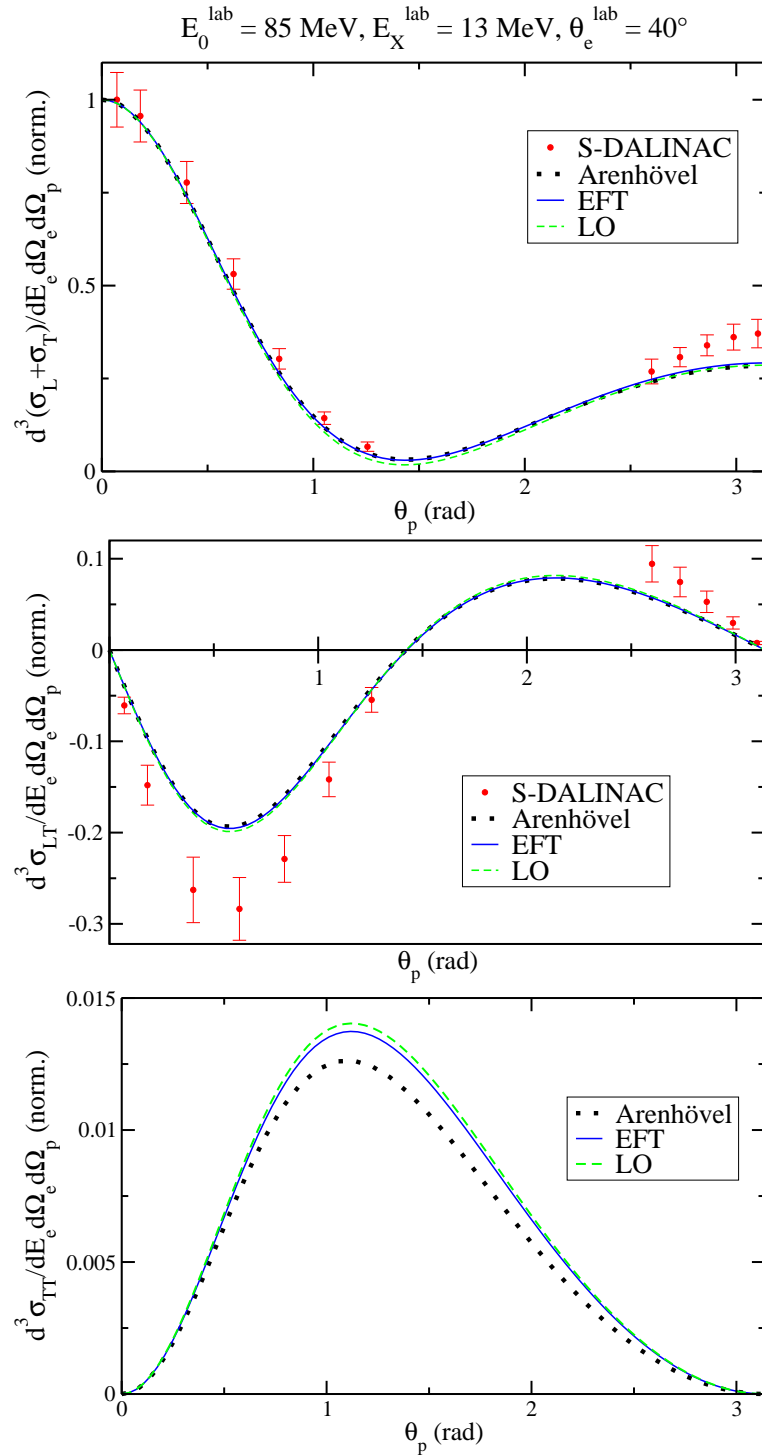
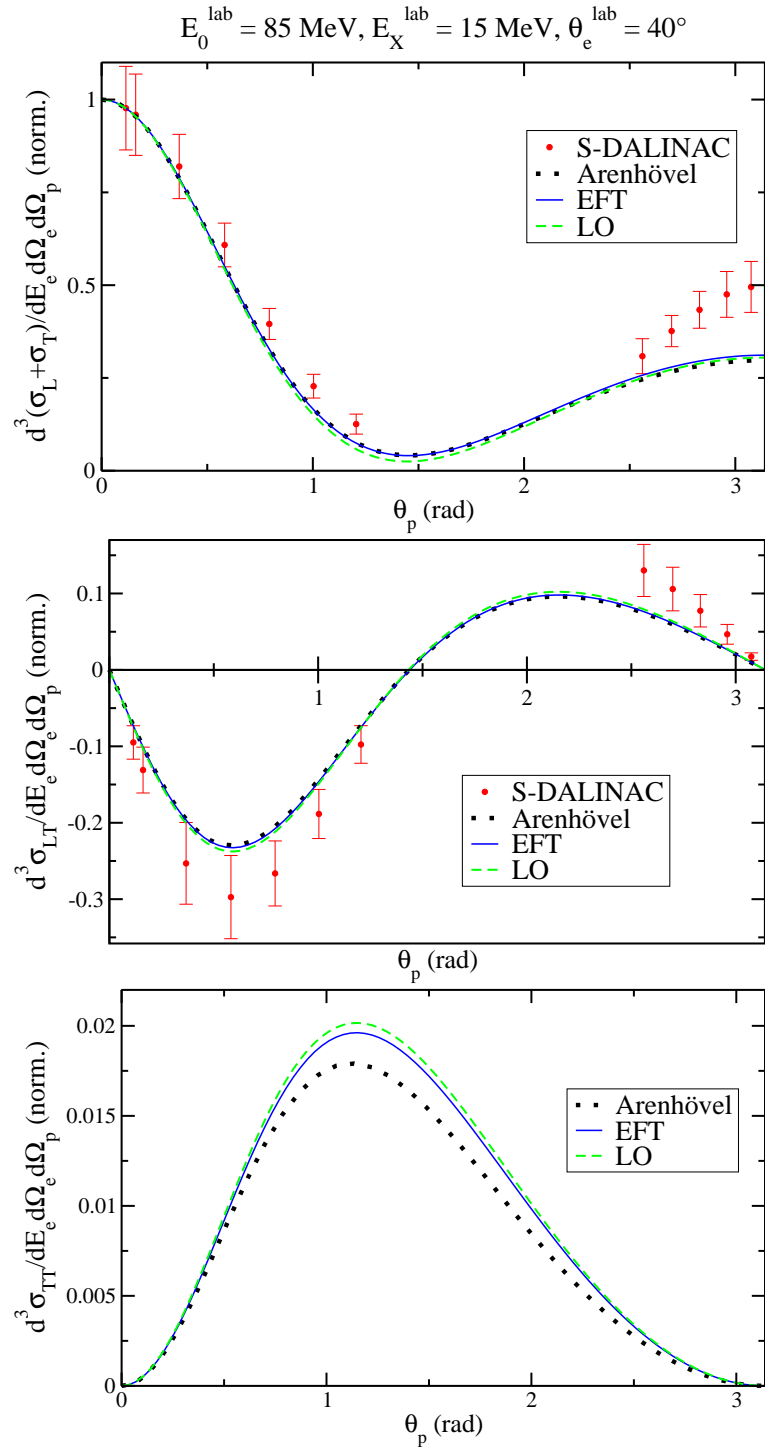


Figure 5.9: The same plots as in Fig. 5.7, but for  $E_X^{\text{lab}} = 13 \text{ MeV}$ .

Figure 5.10: The same plots as in Fig. 5.7, but for  $E_X^{\text{lab}} = 15 \text{ MeV}$ .

Not only the calculated longitudinal-transverse interference cross section deviates by about 30% from the measured one (as pointed out in [9]), but also  $\sigma_L + \sigma_T$  at large  $\Theta_p$ . In particular, it is remarkable that the latter is over-predicted at  $E_X^{\text{lab}} = 9$  MeV, but under-predicted at  $E_X^{\text{lab}} = 15$  MeV. Therefore, we look at the energy dependence of  $\sigma_L + \sigma_T$  at  $\Theta_p = 180^\circ$  in Fig. 5.11. The upper diagram shows the normalized values (as in Figs. 5.7 - 5.10). The discrepancy is very striking: The larger  $E_X^{\text{lab}}$ , the more we under-predict the data. However, if one does not normalize the values, it looks much less dramatic (see Fig. 5.11 in the middle). Thus, normalizing to  $\Theta_p = 0^\circ$  seems to deteriorate the accord of calculations and data – although it avoids accounting for the absolute normalization of data. The reason for this can be seen by comparing the second and third plots in Fig. 5.11 (the latter shows the values to which we normalize). Both display a relatively small deviation, which go, however, in different directions: The theoretical result e. g. at  $E_X^{\text{lab}} = 15$  MeV is a bit too small for  $\Theta_p = 180^\circ$ , but too large for  $\Theta_p = 0^\circ$ ; in dividing these two values, the discrepancy increases, of course. In any case, there is a significant difference in  $\sigma_L + \sigma_T$  between data on the one hand, and the agreeing theoretical predictions of EFT( $\vec{\pi}$ ) and Arenhövel on the other hand.

Now we turn to the longitudinal-transverse interference cross section  $\sigma_{LT}$ . In Figs. 5.7 - 5.10, we see that the angular dependence of the normalized values is reproduced qualitatively, but there is a discrepancy of about 30% (or even more at  $E_X^{\text{lab}} = 9$  MeV). We examine the energy dependence like for  $\sigma_L + \sigma_T$ ; in Fig. 5.12,  $\sigma_{LT}$  at the minimum around  $\Theta_p = 35^\circ$  is plotted as a function of  $E_X^{\text{lab}}$ .

The upper graph shows the values normalized to  $\sigma_L + \sigma_T$  at  $\Theta_p = 0^\circ$ . We observe that they are systematically overestimated by 30%. Again, the situation becomes slightly better when looking at the absolute values (lower plot in Fig. 5.12). However, a clear deviation remains, and surprisingly becomes larger at decreasing  $E_X^{\text{lab}}$ .

In Sect. 4.5, we discussed some short-distance contributions entering at higher orders and found that they can be neglected to a very good approximation. If, in spite of that, some higher order contributions (like e. g. from the  $P$ -wave) were important for  $\sigma_{LT}$ , they would contribute more at higher energies, so that this would not explain the behavior seen in Fig. 5.12. Furthermore – as mentioned above – magnetic transitions have at this order no impact on  $\sigma_{LT}$ ; thus corrections to them which are independent of  $\Phi_p$  cannot be responsible either. Thence EFT( $\vec{\pi}$ ) offers no explanation for the observed discrepancies in comparison with the data. Moreover, we would like to point out once again that calculations within the different framework of a potential model yield essentially the same results as EFT( $\vec{\pi}$ ), especially for  $\sigma_{LT}$ .

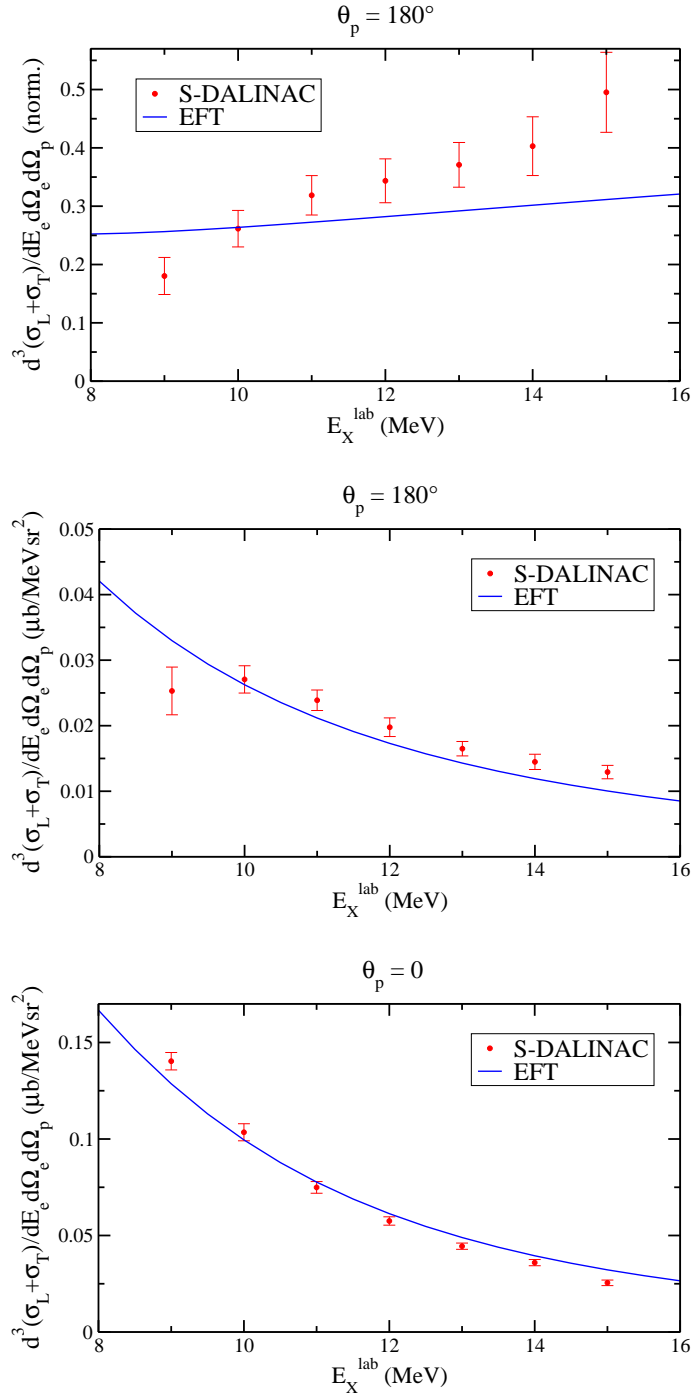


Figure 5.11:  $E_X^{\text{lab}}$ -dependence of  $\sigma_L + \sigma_T$  at  $\Theta_p = 180^\circ$ , normalized to  $\Theta_p = 0^\circ$  (top), and the absolute values (middle). Bottom:  $\sigma_L + \sigma_T$  at  $\Theta_p = 0^\circ$  (to which other values are normalized). All graphs refer to  $E_0^{\text{lab}} = 85$  MeV,  $\Theta_e^{\text{lab}} = 40^\circ$ .

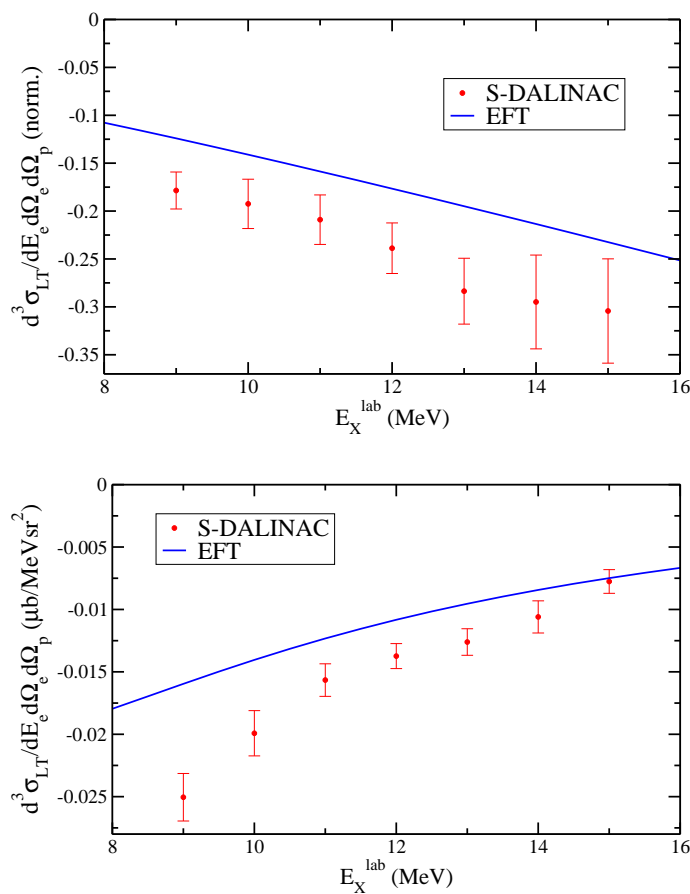


Figure 5.12:  $E_X^{\text{lab}}$ -dependence of  $\sigma_{LT}$  at the minimum around  $\Theta_p = 35^\circ$ , normalized (top) and absolute values (bottom), both for  $E_0^{\text{lab}} = 85$  MeV,  $\Theta_e^{\text{lab}} = 40^\circ$ .

The disagreements with data remain as an open question and suggest a re-analysis of the experiment [38]. If the discrepancies are confirmed, this would pose a non-trivial problem to nuclear theory. It would be interesting to have more data for the deuteron-electrodisintegration process near threshold and at low momentum transfers, particularly concerning the decomposition into the contributions of different structure functions.

One earlier experiment examined this at a slightly higher momentum transfer [39]. There, good accord between data and a potential model calculation was reported, also for the normalized  $\sigma_{LT}$ .<sup>2</sup> We compare therefore

<sup>2</sup>Those calculations were also performed by H. Arenhövel et al., using a Paris potential; the difference to the Bonn potential we are referring to should not be relevant here.

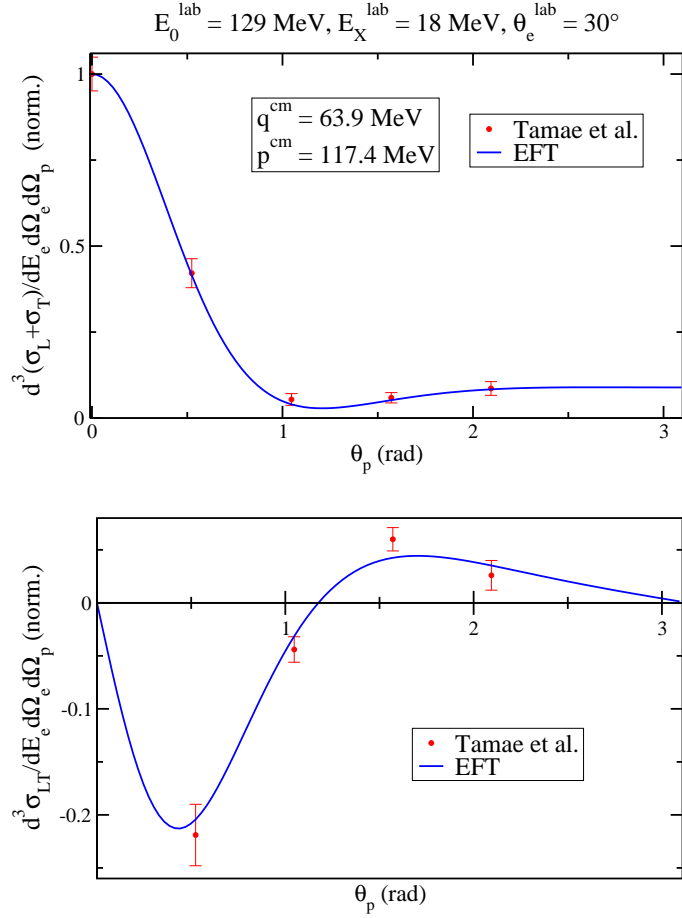


Figure 5.13: Comparison to the data of Ref. [39] for the L+T and LT parts of the triple-differential cross section, both obtained in the *lab* frame (also for the hadronic variables!) and normalized to  $\sigma_{L+T}$  at  $\Theta_p = 0$ .

the EFT( $\vec{k}$ ) result to these data, although the involved proton momentum  $p^{\text{cm}} = 117 \text{ MeV}$  is near the breakdown scale of this theory; we are encouraged by the good agreement with Arenhövel's results at momenta that are not much smaller (e. g. Fig. 5.5). In Fig. 5.13, we observe a very good agreement for the normalized values of  $\sigma_{L+T}$  and  $\sigma_{LT}$ . It is remarkable that our result reproduces the data so well at such a high momentum transfer, but deviates significantly from the more recent data at lower momenta.

### 5.3 Proposed Experiment at Threshold

A deuteron-electrodisintegration experiment directly above threshold is planned at S-DALINAC, where the electron scattering angle is almost  $180^\circ$ . It is important to get experimental information about  $d(e, e'p)n$  at very low nucleon momenta, since from that one can infer the cross section for  $np \rightarrow d\gamma$ . This is a crucial input for calculations concerning big-bang nucleosynthesis (as mentioned in Sect. 3.2) and is not well-known experimentally in this energy regime. H. Arenhövel et al. have again provided theoretical predictions based on the Bonn-potential model for the proposed experiment. We want to compare the EFT( $\pi$ ) result to these predictions.

The experiment will be carried out at incoming electron energies between  $E_0^{\text{lab}} = 20$  and 30 MeV, scattering angle  $\Theta_e^{\text{lab}} = 178.5^\circ$  and transferred energies starting from the value at threshold, which is  $E_X^{\text{lab}} = 2.6$  MeV for  $E_0^{\text{lab}} = 20$  MeV. At the very low momentum transfers corresponding to these values, magnetic transitions are expected to give the dominant contributions. Unfortunately, no azimuthal dependence can be measured for this kinematics, since the coincidence cross sections are too small [40].

At these low energies, it is important to take the non-vanishing electron mass into account; its effect has been negligible at the energies relevant in the previous Sections. In Figs. 5.14 and 5.15, the  $\Theta_p$ -dependence of the triple-differential cross section is shown for  $E_0^{\text{lab}} = 20$  MeV and four different values of  $E_X^{\text{lab}}$ : Directly above threshold, it is practically constant for all  $\Theta_p$ , and electric transitions are suppressed by about four orders of magnitude. For  $E_X^{\text{lab}} = 3$  MeV, a small  $\Theta_p$ -dependence is observed, and magnetic transitions are still largely dominant. For  $E_X^{\text{lab}} = 7.6$  MeV, magnetic and electric contributions are of comparable size, while the latter are dominant for  $E_X^{\text{lab}} = 12.6$  MeV.

The agreement with the potential model result is reasonably good in all graphs; magnetic transitions have been calculated only up to NLO, so one cannot expect a better accordance. Future work will improve the accuracy of the EFT( $\pi$ ) result.

The  $E_X^{\text{lab}}$ -dependence for two different values of  $\Theta_p$  is plotted in Fig. 5.16. For  $\Theta_p = 90^\circ$ , we observe an almost perfect agreement with Arenhövel's result. Furthermore, the energy-dependent contribution of magnetic transitions can be seen clearly: They dominate only below about  $E_X^{\text{lab}} = 5$  MeV for this kinematics. We detect a larger deviation for  $\Theta_p = 0^\circ$ , where electric transitions are negligible over the whole energy-range shown (cf. Fig. 5.15).

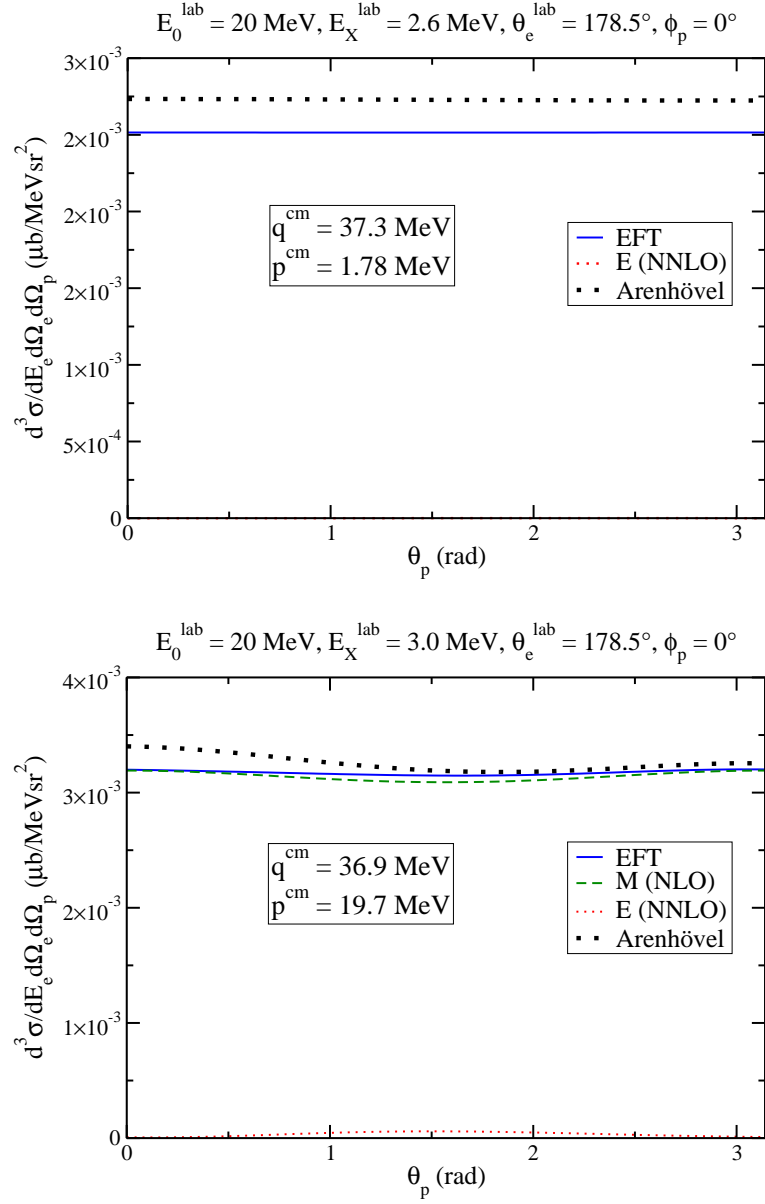


Figure 5.14: Comparison of EFT( $\pi$ )- and potential model results, directly above and close to threshold, respectively.

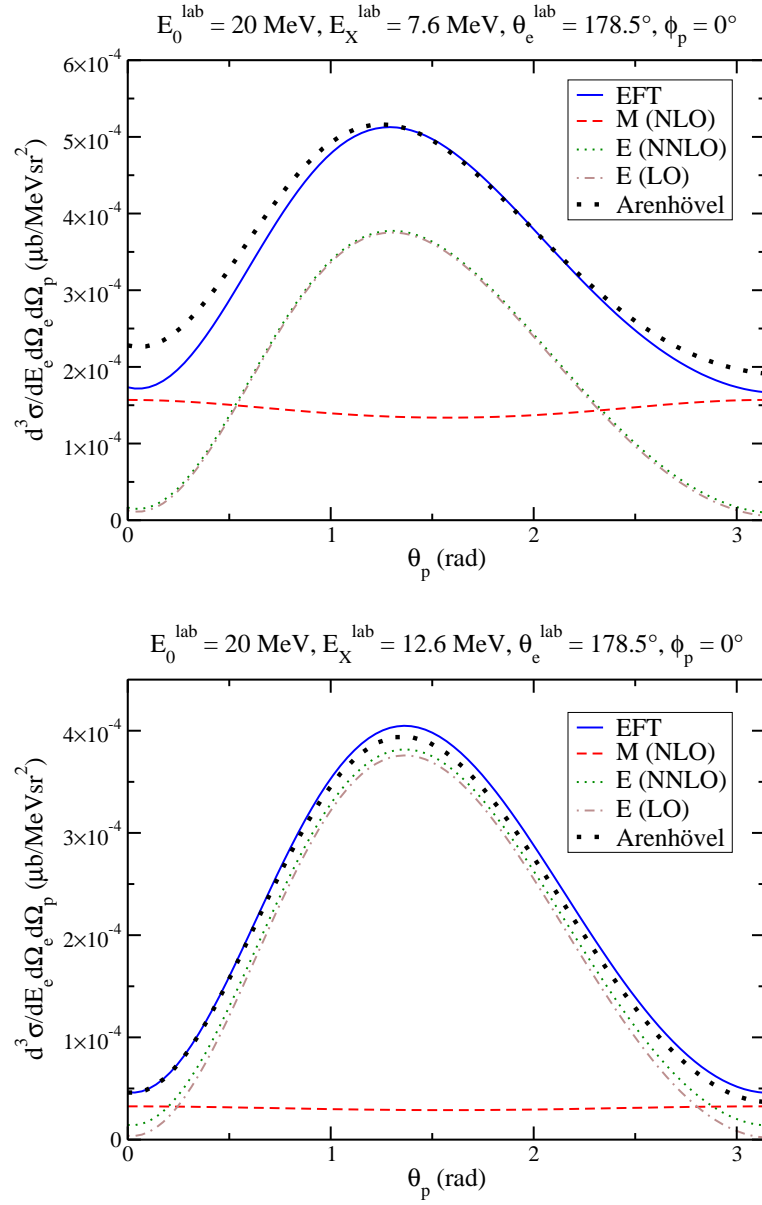


Figure 5.15: Comparison of EFT( $\not{\pi}$ )- and potential model results, for  $E_X^{\text{lab}} = 7.6 \text{ MeV}$  and  $E_X^{\text{lab}} = 12.6$ , respectively.

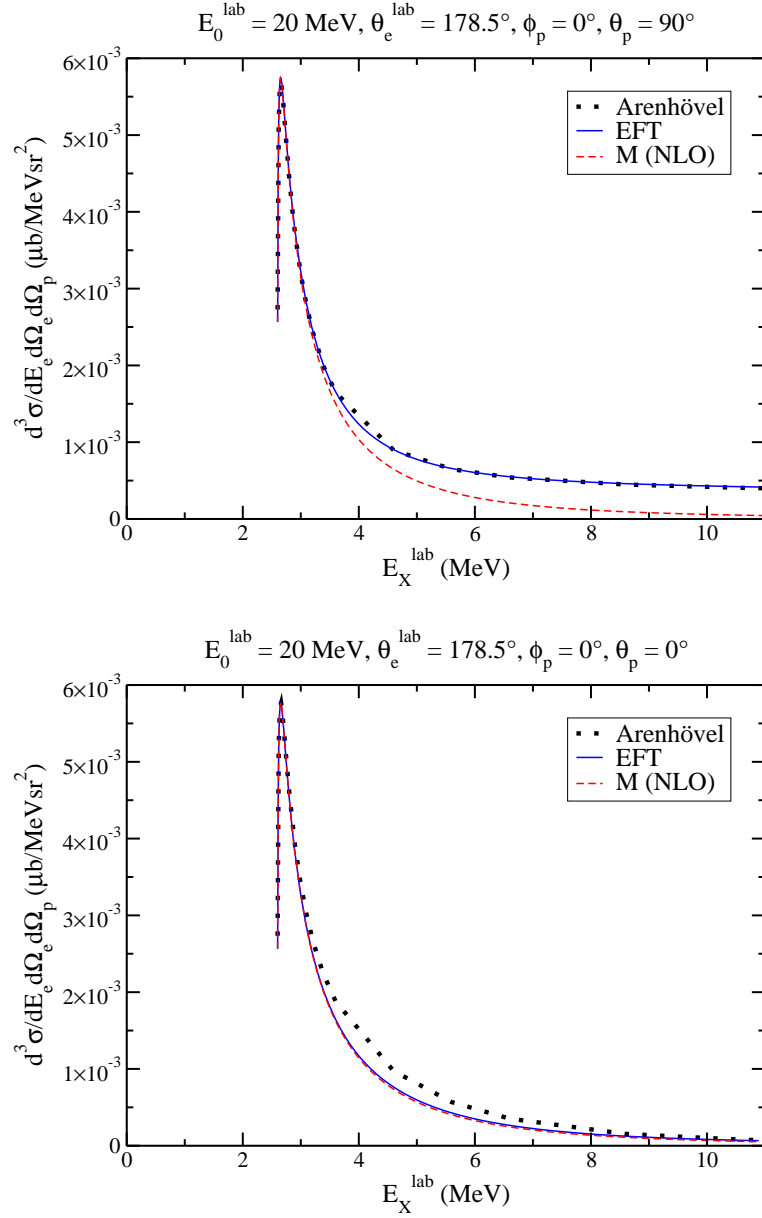


Figure 5.16:  $E_X^{\text{lab}}$ -dependence for  $\Theta_p = 90^\circ$  and  $\Theta_p = 0^\circ$ , respectively. The contribution of magnetic transitions alone is also shown.

The proposed experiment is interesting particularly because it is sensitive to magnetic contributions which are almost negligible for the kinematics used in [9]. We are looking forward to see whether the predictions of EFT( $\not{\pi}$ ) will be confirmed in this sector. Besides we hope that the contributions of the different structure functions will be re-examined experimentally in the future. A discrepancy as large as the one discussed in the previous Section should give rise to more effort both from the experimental and from the theoretical side; after all, it concerns a quantity of rather fundamental importance – the response of the nucleon-nucleon system to electromagnetic probes.

# Chapter 6

## Summary

In this work, the triple-differential cross section for deuteron-electrodisintegration at low energies has been calculated. We have employed an effective field theory (EFT( $\not{\pi}$ )) that was constructed to describe few-nucleon systems at energies below the pion mass ([22] and references there), as an extension of Effective Range Theory [10]. The existence of unnaturally large length scales in the two-nucleon sector requires a modification of the naive power counting scheme [15]. Nucleon-nucleon interactions are conveniently described by introducing explicit dibaryon fields [13] in the Lagrangean of EFT( $\not{\pi}$ ). This Lagrangean is considered up to NNLO for electric transitions and up to NLO for magnetic ones. The unknown coefficients that enter at these orders are determined by examining the electric form factors of the deuteron and the cross section for the radiative capture of thermal neutrons by protons (see [11] for a review of these applications).

The LO electric transitions give the dominant contributions to the cross section for  $d(e, e'p)n$  at moderate energy- and momentum transfer. The first corrections arise from the mixing of  $S$ - and  $D$ -states and enter at NNLO; their contribution is smaller than estimated by power counting. This means that minimal coupling describes the process highly accurately. The impact of magnetic transitions is also small in this energy regime; it becomes more important with decreasing momentum transfer.

Compared to a potential-model calculation [8], the EFT( $\not{\pi}$ ) result is in very good agreement. Data taken at S-DALINAC [9] are also reproduced rather well for the full triple-differential cross section, but for its decomposition into the contributions of different structure functions, we observe some discrepancies. This is remarkable, since not only do the potential-model predictions agree with our result but also an earlier experiment [39] carried out at a slightly higher momentum transfer.

We also compared the EFT( $\not{\pi}$ ) prediction to the one of a potential model

for a proposed experiment directly above the breakup threshold, where magnetic transitions are dominant. Relatively good agreement is found again. It will be interesting to see the results of this experiment, although it will not be able to resolve the contributions of the different structure functions. This latter issue – where there are significant discrepancies between calculations and data – should be re-examined by future experiments. If the existing data are confirmed, this would pose a non-trivial problem to nuclear theory, concerning a very fundamental sector, the two-nucleon system.

# Appendix A

## Feynman Rules

In this Chapter, all Feynman rules applied in this work are summarized. They follow from the Lagrangean (2.29).

$\mathcal{L}_N$  (2.30) yields the following two  $NN\gamma$  vertices:

$$\underbrace{\left. \begin{array}{l} p \\ \phantom{p} \\ p' \end{array} \right\}} = -ieQA^0 + i\frac{e}{2M}Q(\mathbf{p} + \mathbf{p}') \cdot \mathbf{A} \quad (\text{A.1})$$

simply from minimal substitution, and

$$\underbrace{\left. \begin{array}{l} q \\ \bullet \end{array} \right\}} = \pm \frac{e}{2M} \kappa_1 \tau_3 \epsilon^{ijk} \sigma^i q^j A^k; \quad (\text{A.2})$$

only the isovector magnetic coupling proportional to  $\kappa_1$  is shown here, represented by the solid circle. The  $\kappa_0$ -term is left out because it is numerically much smaller ( $\kappa_0 = 0.44 \ll \kappa_1 = 2.35$ ). The plus- and minus-signs refer to an outgoing and incoming photon, respectively.

The NN-dibaryon vertices for the  $^1S_0$  and  $^3S_1$  channels read

$$\begin{array}{c} \text{\scriptsize } ^1S_0 \\ \text{---} \text{---} \text{---} \end{array} \begin{array}{l} \diagup \\ \diagdown \end{array} = -iy_s P_a^{(^1S_0)} \epsilon_I^a, \quad (\text{A.3})$$

$$\begin{array}{c} \text{\scriptsize } ^3S_1 \\ \text{=} \text{=} \text{---} \end{array} \begin{array}{l} \diagup \\ \diagdown \end{array} = -iy_t P_i^{(^3S_1)} \epsilon^i. \quad (\text{A.4})$$

$\epsilon_I^a$  characterizes the isovector state of  $s_a$ , while  $\epsilon^i$  is the polarization vector of the  $^3S_1$ -dibaryon. Minimal coupling in both channels gives the dibaryon-photon vertex

$$\underline{\underline{\left. \begin{array}{l} p \\ \phantom{p} \\ p' \end{array} \right\}}} = ieA^0 - i\frac{e}{4M}(\mathbf{p} + \mathbf{p}') \cdot \mathbf{A}. \quad (\text{A.5})$$

The following four vertices represent sd-mixing:

$$\begin{aligned}
 \text{Diagram 1} &= -i \frac{C_{sd}}{4\sqrt{M\rho_d}} \\
 &\times \left\{ \mathbf{P}^\dagger \cdot (\mathbf{p}_\alpha - \mathbf{p}_\beta)(p_\alpha^i - p_\beta^i) - \frac{1}{3} P_i^\dagger (\mathbf{p}_\alpha - \mathbf{p}_\beta)^2 \right\} \epsilon^i, \quad (\text{A.6})
 \end{aligned}$$

$$\begin{aligned}
 \text{Diagram 2} &= -i \frac{C_{sd}}{4\sqrt{M\rho_d}} \\
 &\times \left\{ \mathbf{P} \cdot (\mathbf{p}_\alpha - \mathbf{p}_\beta)(p_\alpha^i - p_\beta^i) - \frac{1}{3} P_i (\mathbf{p}_\alpha - \mathbf{p}_\beta)^2 \right\} \epsilon^{*i}, \quad (\text{A.7})
 \end{aligned}$$

$$\begin{aligned}
 \text{Diagram 3} &= -ie \frac{C_{sd}}{4\sqrt{M\rho_d}} \left\{ (-\mathbf{p}_\alpha + \mathbf{p}_\beta - \frac{1}{2}\mathbf{q}) \cdot [Q, \mathbf{P}^\dagger] \delta_{ik} \right. \\
 &+ (-p_\alpha^i + p_\beta^i + \frac{1}{2}q^i)[Q, P^{\dagger k}] + \frac{1}{2}\mathbf{q} \cdot \mathbf{P}^\dagger \delta_{ik} + \frac{1}{2}q^i P^{\dagger k} \\
 &\left. - \frac{2}{3}(-p_\alpha^k + p_\beta^k)[Q, P^{\dagger i}] - \frac{1}{3}q^k P^{\dagger i} \right\} \epsilon^i A^k, \quad (\text{A.8})
 \end{aligned}$$

$$\begin{aligned}
 \text{Diagram 4} &= ie \frac{C_{sd}}{4\sqrt{M\rho_d}} \left\{ (\mathbf{p}_\alpha - \mathbf{p}_\beta + \frac{1}{2}\mathbf{q}) \cdot [Q, \mathbf{P}^\dagger] \delta_{ik} \right. \\
 &+ (p_\alpha^i - p_\beta^i - \frac{1}{2}q^i)[Q, P^{\dagger k}] + \frac{1}{2}\mathbf{q} \cdot \mathbf{P}^\dagger \delta_{ik} + \frac{1}{2}q^i P^{\dagger k} \\
 &\left. - \frac{2}{3}(p_\alpha^k - p_\beta^k)[Q, P^{\dagger i}] - \frac{1}{3}q^k P^{\dagger i} \right\} \epsilon^{*i} A^k. \quad (\text{A.9})
 \end{aligned}$$

The open circle indicates the coupling of a deuteron to two nucleons in a d-wave. The operator  $P_i$  is understood to project on the  ${}^3S_1$ -channel:  $P_i \equiv P_i^{({}^3S_1)}$ . (A.8) and (A.9) are the vertices for incoming photons. The last term in (2.32) gives rise to the vertex

$$\text{Diagram 5} = -ie \frac{C_Q}{M\rho_d} \left( q^i q^j - \frac{1}{3} \delta^{ij} \right) A^0. \quad (\text{A.10})$$

Finally, the coupling of a  ${}^1S_0$  and a  ${}^3S_1$  dibaryon to a magnetic photon (2.33) is denoted by

$$\text{Diagram 6} = \pm \frac{eL_1}{M\sqrt{r_0\rho_d}} \epsilon^{ijk} \epsilon^i q^j A^k, \quad (\text{A.11})$$

where the plus (minus) sign again corresponds to an incoming (outgoing) photon.

# Appendix B

## Projection Operators

To project onto a given spin-isospin state of the two-nucleon system we have used the operators defined in (2.36),

$$P_a^{(1S_0)} = \frac{1}{\sqrt{8}}\sigma_2\tau_2\tau_a, \quad P_i^{(3S_1)} = \frac{1}{\sqrt{8}}\sigma_2\sigma_i\tau_2, \quad (\text{B.1})$$

where the Pauli matrices  $\sigma$  and  $\tau$  act on spin- and isospin space, respectively, and read in the standard representation:

$$\tau_1 = \begin{pmatrix} 0 & 1 \\ 1 & 0 \end{pmatrix}, \quad \tau_2 = \begin{pmatrix} 0 & -i \\ i & 0 \end{pmatrix}, \quad \tau_3 = \begin{pmatrix} 1 & 0 \\ 0 & -1 \end{pmatrix}. \quad (\text{B.2})$$

The projectors in (B.1) differ from the “traditional” ones composed of the operators

$$P_S = \frac{1}{4}(1 - \tau^{(1)} \cdot \tau^{(2)}), \quad P_T = \frac{1}{4}(3 + \tau^{(1)} \cdot \tau^{(2)}) \quad (\text{B.3})$$

which project onto singlet- and triplet states, respectively. The isospin of particle  $i$  is  $\mathbf{t}^{(i)} = \frac{1}{2}\tau^{(i)}$ , and that of the two-nucleon system is  $\mathbf{T} = \mathbf{t}^{(1)} + \mathbf{t}^{(2)}$  with  $\mathbf{T}^2 = T(T+1) = 0$  for the singlet and  $\mathbf{T}^2 = 1$  for the triplet.

In the following, we show that the operators in (B.1) also project onto the correct states, i. e. that  $N^T P_a^{(1S_0)} N$  represents two nucleons in a spin-singlet and isospin-triplet state (and vice versa for  $N^T P_i^{(3S_1)} N$ ). This can be easily seen by computing

$$N^T \tau_2 N = (p, n)\tau_2 \begin{pmatrix} p \\ n \end{pmatrix} = i(np - pn) \quad (\text{B.4})$$

which corresponds to the isospin-singlet, and

$$N^T \tau_2 \tau_3 N = (p, n)\tau_2 \tau_3 \begin{pmatrix} p \\ n \end{pmatrix} = i(np + pn) \quad (\text{B.5})$$

which is the proton-neutron state in the isospin-triplet. Linear combinations of  $N^T \tau_2 \tau_1 N$  and  $N^T \tau_2 \tau_2 N$  represent the proton-proton- and neutron-neutron states. Analogously,  $\sigma_2$  projects on the spin-singlet and  $\sigma_2 \sigma_i$  on the spin-triplet.

Now we still have to motivate the normalization of  $P_a^{(1S_0)}$  and  $P_i^{(3S_1)}$ . This is carried out in [41]: To consider the scattering of two nucleons with momenta  $\mathbf{k}/2 \pm \mathbf{p}$  in the center-of-mass frame, we define two-nucleon states by

$$|NN(s; \mathbf{k}, p)\rangle = \frac{p}{\sqrt{4\pi}} \frac{1}{(2\pi)^3} \int d\Omega_{\mathbf{p}} [N^T(\mathbf{k}/2 + \mathbf{p}) P^{(s)} N(\mathbf{k}/2 - \mathbf{p})]^\dagger |0\rangle, \quad (\text{B.6})$$

where  $s = {}^{2S+1}L_J$ . These states are normalized such that averaging over polarizations gives

$$\sum_{\text{pol. avg.}} \langle NN(s'; \mathbf{k}', p') | NN(s; \mathbf{k}, p) \rangle = \delta^3(\mathbf{k}' - \mathbf{k}) \delta(p' - p) \delta^{s's}. \quad (\text{B.7})$$

This is fulfilled if the projection matrices satisfy

$$\sum_{\text{pol. avg.}} \text{Tr}[P^{(s)} P^{(s)\dagger}] = \frac{1}{2}, \quad (\text{B.8})$$

which is true for the normalization used in (B.1).

# Appendix C

## Kinematics for the Triple-Differential Cross Section

In the following, we derive the expression (4.13) for the triple-differential cross section  $\frac{d^3\sigma}{dE_e^{\text{lab}}d\Omega_e^{\text{lab}}d\Omega_p}$ , where all variables concerning electrons are defined in the lab frame, while the quantities of the final  $np$ -state refer to the final-state center-of-mass frame. The initial state consists of an electron with four-momentum  $k^{\mu\text{lab}} = (E_0^{\text{lab}}, \mathbf{k}^{\text{lab}})$  and a deuteron with  $p_d^{\mu\text{lab}} = (E_d^{\text{lab}}, -\mathbf{q}^{\text{lab}})$ , and in the final state we have an electron with  $k'^{\mu\text{lab}} = (E_e^{\text{lab}}, \mathbf{k}'^{\text{lab}})$ , a proton with  $p_p^\mu = (E_p, \mathbf{p})$  and a neutron with  $p_n^\mu = (E_n, -\mathbf{p})$ . The five independent variables that describe the kinematics completely are  $E_0^{\text{lab}}$ ,  $E_e^{\text{lab}}$ , the electron scattering angle  $\Theta_e^{\text{lab}}$  and the angle between proton and photon momenta  $\Theta_p$  and  $\Phi_p$ .

We start with the well-known formula for a multiple differential cross section found e. g. in [30], which in our case reads:

$$d\sigma = \frac{1}{4\sqrt{(k^{\mu\text{lab}} p_{d\mu}^{\text{lab}})^2 - M_d^2 m_e^2}} |\mathcal{A}|^2 \frac{d^3 k'^{\text{lab}}}{(2\pi)^3 2E_e^{\text{lab}}} \frac{d^3 p_p}{(2\pi)^3 2E_p} \frac{d^3 p_n}{(2\pi)^3 2E_n} \times (2\pi)^4 \delta^4(k'^{\mu\text{lab}} + p_p^\mu + p_n^\mu - k^{\mu\text{lab}} - p_d^{\mu\text{lab}}) (2M_d)(2M)^2. \quad (\text{C.1})$$

Integrating over the neutron three-momentum gives

$$d\sigma = \frac{1}{4\sqrt{(E_d^{\text{lab}} E_0^{\text{lab}} + \mathbf{q}^{\text{lab}} \cdot \mathbf{k}^{\text{lab}})^2 - M_d^2 m_e^2}} |\mathcal{A}|^2 \frac{d^3 k'^{\text{lab}} d^3 p_p}{(2\pi)^5 8E_e^{\text{lab}} E_p E_n} \times \delta(E_e^{\text{lab}} + E_p + E_n - E_d^{\text{lab}} - E_0^{\text{lab}}) 8M_d M^2. \quad (\text{C.2})$$

Then we apply  $d^3 k' = k'^2 dk' d\Omega_e = k' E_e dE_e d\Omega_e$  and  $d^3 p_p = p_p E_p dE_p d\Omega_p$ , and

rewrite the  $\delta$ -function as

$$\delta(f(E_p)) = \frac{1}{|f'(E_p^0)|} \delta(E_p - E_p^0), \quad (\text{C.3})$$

whose argument is  $f(E_p) = 2E_p + E_e^{\text{lab}} - E_d^{\text{lab}} - E_0^{\text{lab}}$  (since  $E_n = E_p = M + \frac{p^2}{2M}$ ) and becomes zero at  $E_p^0 = \frac{1}{2}(E_d^{\text{lab}} + E_0^{\text{lab}} - E_e^{\text{lab}})$ . Thus we get

$$\begin{aligned} d\sigma &= \frac{1}{4\sqrt{(E_d^{\text{lab}} E_0^{\text{lab}} + \mathbf{q}^{\text{lab}} \cdot \mathbf{k}^{\text{lab}})^2 - M_d^2 m_e^2}} |\mathcal{A}|^2 \frac{k'^{\text{lab}} dE_e^{\text{lab}} d\Omega_e^{\text{lab}} p dE_p d\Omega_p}{(2\pi)^5 E_n} \\ &\quad \times M_d M^2 \frac{1}{2} \delta(E_p - E_p^0), \end{aligned} \quad (\text{C.4})$$

and after the  $E_p$ -integration we arrive at (4.13)

$$\frac{d^3\sigma}{dE_e^{\text{lab}} d\Omega_e^{\text{lab}} d\Omega_p} = \frac{k'^{\text{lab}} p M_d M^2}{8(2\pi)^5 (M + \frac{p^2}{2M}) \sqrt{(M_d E_0^{\text{lab}} + \mathbf{q}^{\text{lab}} \cdot \mathbf{k}^{\text{lab}})^2 - M_d^2 m_e^2}} |\mathcal{A}|^2. \quad (\text{C.5})$$

# Appendix D

## Useful Integrals

In this Appendix, all loop integrals used are calculated. The integration over the zero-component of the loop four-momentum  $l_\mu$  is not shown here; divergent integrals are evaluated in  $D$  space-dimensions and regularized in the PDS scheme (Sect. 2.2.2).

In (2.12) we already employed the following result:

$$\begin{aligned}
 I_0^{(1)}(a) &= \left(\frac{\mu}{2}\right)^{3-D} \int \frac{d^D l}{(2\pi)^D} \frac{1}{(\mathbf{1} + \frac{\mathbf{q}}{2})^2 + a} \\
 &= \left(\frac{\mu}{2}\right)^{3-D} (4\pi)^{-D/2} \Gamma\left(\frac{2-D}{2}\right) a^{\frac{D-2}{2}} \\
 &\stackrel{\text{PDS}}{=} \frac{1}{4\pi} (\mu - \sqrt{a})
 \end{aligned} \tag{D.1}$$

(see [1], or [32] for a detailed derivation). We often needed (e.g. in (3.4)) the integral (see e. g. [33])

$$\begin{aligned}
 I_0^{(2)}(a, b) &= \int \frac{d^3 l}{(2\pi)^3} \frac{1}{l^2 + a} \frac{1}{(\mathbf{1} + \frac{\mathbf{q}}{2})^2 + b} \\
 &= \frac{1}{2\pi q} \arctan\left(\frac{q}{2(\sqrt{a} + \sqrt{b})}\right).
 \end{aligned} \tag{D.2}$$

The following more complicated integrals can be expressed in terms of (D.1) and (D.2), using the method of tensorial reduction:

$$\begin{aligned}
 I_1^{(1)i}(a) &= \int \frac{d^D l}{(2\pi)^D} \frac{\mathbf{l}^i}{(\mathbf{1} + \frac{\mathbf{q}}{2})^2 + a} \\
 &= -\frac{\mathbf{q}^i}{2} I_0^{(1)}(a);
 \end{aligned} \tag{D.3}$$

$$\begin{aligned}
I_2^{(1)ij}(a) &= \int \frac{d^D l}{(2\pi)^D} \frac{\mathbf{l}^i \mathbf{l}^j}{(\mathbf{1} + \frac{\mathbf{q}}{2})^2 + a} \\
&= \int \frac{d^D l}{(2\pi)^D} \frac{(\mathbf{l}^i - \frac{\mathbf{q}^i}{2})(\mathbf{l}^j - \frac{\mathbf{q}^j}{2})}{l^2 + a} \\
&= \int \frac{d^D l}{(2\pi)^D} \frac{\mathbf{l}^i \mathbf{l}^j + \frac{\mathbf{q}^i \mathbf{q}^j}{4}}{l^2 + a} \\
&= -\frac{1}{D} a I_0^{(1)}(a) \delta^{ij} + \frac{1}{4} I_0^{(1)}(a) \mathbf{q}^i \mathbf{q}^j \tag{D.4}
\end{aligned}$$

(for the last step, see e. g. [34]), which implies

$$\int \frac{d^D l}{(2\pi)^D} \frac{(\mathbf{q} \cdot \mathbf{l})^2}{(\mathbf{1} + \frac{\mathbf{q}}{2})^2 + a} = \left( \frac{q^4}{4} - \frac{a q^2}{D} \right) I_0^{(1)}(a).$$

Furthermore,

$$\begin{aligned}
I_1^{(2)i}(a, b) &= \int \frac{d^D l}{(2\pi)^D} \frac{\mathbf{l}^i}{l^2 + a} \frac{1}{(\mathbf{1} + \frac{\mathbf{q}}{2})^2 + b} \\
&= A_1(a, b) \frac{\mathbf{q}^i}{q^2} \tag{D.5}
\end{aligned}$$

with

$$\begin{aligned}
A_1(a, b) &= \int \frac{d^D l}{(2\pi)^D} \frac{\mathbf{l} \cdot \mathbf{q}}{l^2 + a} \frac{1}{(\mathbf{1} + \frac{\mathbf{q}}{2})^2 + b} \\
&= \int \frac{d^D l}{(2\pi)^D} \frac{1}{l^2 + a} \left[ 1 - \frac{l^2 + \frac{q^2}{4} + b}{(\mathbf{1} + \frac{\mathbf{q}}{2})^2 + b} \right] \\
&= I_0^{(1)}(a) - I_0^{(1)}(b) - \left( \frac{q^2}{4} + b - a \right) I_0^{(2)}(a, b). \tag{D.6}
\end{aligned}$$

With two loop-momenta in the numerator:

$$\begin{aligned}
I_2^{(2)ij}(a, b) &= \int \frac{d^D l}{(2\pi)^D} \frac{\mathbf{l}^i \mathbf{l}^j}{l^2 + a} \frac{1}{(\mathbf{1} + \frac{\mathbf{q}}{2})^2 + b} \\
&= A_2(a, b) \delta^{ij} + B_2(a, b) \mathbf{q}^i \mathbf{q}^j, \tag{D.7}
\end{aligned}$$

where

$$\begin{aligned}
A_2(a, b) &= \frac{1}{D-1} \left[ \delta_{ij} - \frac{\mathbf{q}_i \mathbf{q}_j}{q^2} \right] \int \frac{d^D l}{(2\pi)^D} \frac{\mathbf{l}^i \mathbf{l}^j}{l^2 + a} \frac{1}{(\mathbf{1} + \frac{\mathbf{q}}{2})^2 + b} \\
&= \frac{1}{D-1} \int \frac{d^D l}{(2\pi)^D} \frac{l^2 - \frac{(\mathbf{1} \cdot \mathbf{q})^2}{q^2}}{l^2 + a} \frac{1}{(\mathbf{1} + \frac{\mathbf{q}}{2})^2 + b} \\
&= \frac{1}{D-1} \int \frac{d^D l}{(2\pi)^D} \left[ \left( 1 - \frac{a}{l^2 + a} \right) \frac{1}{(\mathbf{1} + \frac{\mathbf{q}}{2})^2 + b} \right. \\
&\quad \left. + \frac{\mathbf{1} \cdot \mathbf{q}}{q^2} \left( 1 + \frac{\frac{q^2}{4} + b - a}{l^2 + a} \right) \frac{1}{(\mathbf{1} + \frac{\mathbf{q}}{2})^2 + b} \right] \\
&= \frac{1}{D-1} \left[ \frac{1}{2} I_0^{(1)}(b) - a I_0^{(2)}(a, b) + \frac{\frac{q^2}{4} + b - a}{q^2} A_1(a, b) \right], \quad (\text{D.8})
\end{aligned}$$

$$\begin{aligned}
B_2(a, b) &= \frac{1}{1-D} \frac{1}{q^2} \left[ \delta_{ij} - D \frac{\mathbf{q}_i \mathbf{q}_j}{q^2} \right] \int \frac{d^D l}{(2\pi)^D} \frac{\mathbf{l}^i \mathbf{l}^j}{l^2 + a} \frac{1}{(\mathbf{1} + \frac{\mathbf{q}}{2})^2 + b} \\
&= \frac{1}{1-D} \frac{1}{q^2} \int \frac{d^D l}{(2\pi)^D} \frac{l^2 - D \frac{(\mathbf{1} \cdot \mathbf{q})^2}{q^2}}{l^2 + a} \frac{1}{(\mathbf{1} + \frac{\mathbf{q}}{2})^2 + b} \\
&= \frac{1}{1-D} \frac{1}{q^2} \left[ \frac{2-D}{2} I_0^{(1)}(b) - a I_0^{(2)}(a, b) + D \frac{\frac{q^2}{4} + b - a}{q^2} A_1(a, b) \right]. \quad (\text{D.9})
\end{aligned}$$

It follows from (D.7) that

$$\int \frac{d^D l}{(2\pi)^D} \frac{\mathbf{l}^i \mathbf{l}^j - \frac{1}{D} l^2 \delta^{ij}}{l^2 + a} \frac{1}{(\mathbf{1} + \frac{\mathbf{q}}{2})^2 + b} = B_2(a, b) \left( \mathbf{q}^i \mathbf{q}^j - \frac{1}{D} q^2 \delta^{ij} \right). \quad (\text{D.10})$$

Finally, we find for three loop-momenta in the numerator:

$$\begin{aligned}
I_3^{(2)ijk}(a, b) &= \int \frac{d^D l}{(2\pi)^D} \frac{\mathbf{l}^i \mathbf{l}^j \mathbf{l}^k}{l^2 + a} \frac{1}{(\mathbf{1} + \frac{\mathbf{q}}{2})^2 + b} \\
&= A_3(a, b) (\mathbf{q}^i \delta^{jk} + \mathbf{q}^j \delta^{ik} + \mathbf{q}^k \delta^{ij}) + B_3(a, b) \mathbf{q}^i \mathbf{q}^j \mathbf{q}^k \quad (\text{D.11})
\end{aligned}$$

with

$$\begin{aligned}
A_3(a, b) &= \frac{1}{3(D-1)q^2} \left[ \mathbf{q}^i \delta^{jk} + \mathbf{q}^j \delta^{ik} + \mathbf{q}^k \delta^{ij} - \frac{3}{q^2} \mathbf{q}^i \mathbf{q}^j \mathbf{q}^k \right] I_3^{(2)ijk}(a, b) \\
&= \frac{1}{3(D-1)q^2} \int \frac{d^D l}{(2\pi)^D} \frac{1}{l^2 + a} \frac{1}{\left(1 + \frac{\mathbf{q}}{2}\right)^2 + b} \left[ 3(\mathbf{q} \cdot \mathbf{l}) l^2 - \frac{3}{q^2} (\mathbf{q} \cdot \mathbf{l})^3 \right] \\
&= \frac{1}{(D-1)q^2} \left[ \int \frac{d^D l}{(2\pi)^D} \frac{\mathbf{q} \cdot \mathbf{l}}{\left(1 + \frac{\mathbf{q}}{2}\right)^2 + b} \left(1 - \frac{a}{l^2 + a}\right) \right. \\
&\quad \left. - \frac{1}{q^2} \int \frac{d^D l}{(2\pi)^D} \frac{(\mathbf{q} \cdot \mathbf{l})^3}{l^2 + a} \frac{1}{\left(1 + \frac{\mathbf{q}}{2}\right)^2 + b} \right] \\
&= \frac{1}{(D-1)q^2} \left[ -\frac{q^2}{2} I_0^{(1)}(b) - a A_1(a, b) - \frac{1}{q^2} \hat{A}_3(a, b) \right], \quad (\text{D.12})
\end{aligned}$$

$$\begin{aligned}
B_3(a, b) &= \frac{D+2}{D-1} \frac{1}{q^6} \left[ \mathbf{q}^i \mathbf{q}^j \mathbf{q}^k - \frac{1}{D+2} q^2 (\mathbf{q}^i \delta^{jk} + \mathbf{q}^j \delta^{ik} + \mathbf{q}^k \delta^{ij}) \right] I_3^{(2)ijk}(a, b) \\
&= \frac{D+2}{D-1} \frac{1}{q^6} \int \frac{d^D l}{(2\pi)^D} \frac{1}{l^2 + a} \frac{1}{\left(1 + \frac{\mathbf{q}}{2}\right)^2 + b} \left[ (\mathbf{q} \cdot \mathbf{l})^3 - \frac{3q^2}{D+2} (\mathbf{q} \cdot \mathbf{l}) l^2 \right] \\
&= \frac{D+2}{D-1} \frac{1}{q^6} \left[ \hat{A}_3(a, b) - \frac{3q^2}{D+2} \left( -\frac{q^2}{2} I_0^{(1)}(b) - a A_1(a, b) \right) \right], \quad (\text{D.13})
\end{aligned}$$

$$\begin{aligned}
\hat{A}_3(a, b) &= \int \frac{d^D l}{(2\pi)^D} \frac{(\mathbf{q} \cdot \mathbf{l})^3}{l^2 + a} \frac{1}{\left(1 + \frac{\mathbf{q}}{2}\right)^2 + b} \\
&= \int \frac{d^D l}{(2\pi)^D} \frac{(\mathbf{q} \cdot \mathbf{l})^2}{l^2 + a} \left( 1 - \frac{l^2 + \frac{q^2}{4} + b}{\left(1 + \frac{\mathbf{q}}{2}\right)^2 + b} \right) \\
&= -\frac{aq^2}{D} I_0^{(1)}(a) - \int \frac{d^D l}{(2\pi)^D} \frac{(\mathbf{q} \cdot \mathbf{l})^2}{\left(1 + \frac{\mathbf{q}}{2}\right)^2 + b} \left( 1 + \frac{\frac{q^2}{4} + b - a}{l^2 + a} \right) \\
&= -\frac{aq^2}{D} I_0^{(1)}(a) - \left( \frac{q^4}{4} - \frac{bq^2}{D} \right) I_0^{(1)}(b) \\
&\quad + \left( \frac{q^2}{4} + b - a \right) \frac{d^D l}{(2\pi)^D} \frac{(\mathbf{q} \cdot \mathbf{l})}{\left(1 + \frac{\mathbf{q}}{2}\right)^2 + b} \left( 1 + \frac{\frac{q^2}{4} + b - a}{l^2 + a} \right) \\
&= -\frac{aq^2}{D} I_0^{(1)}(a) - \left( \frac{q^4}{4} - \frac{bq^2}{D} \right) I_0^{(1)}(b) \\
&\quad + \left( \frac{q^2}{4} + b - a \right) \left[ -\frac{q^2}{2} I_0^{(1)}(b) + \left( \frac{q^2}{4} + b - a \right) A_1(a, b) \right]. \quad (\text{D.14})
\end{aligned}$$

We see from (D.11) that

$$\begin{aligned}
& \int \frac{d^3 l}{(2\pi)^3} \frac{1}{l^2 + a} \frac{1}{(1 + \frac{\mathbf{a}}{2})^2 + b} \left( \mathbf{l}^i \mathbf{l}^j \mathbf{l}^k - \frac{1}{D} l^2 \mathbf{l}^k \delta^{ij} \right) \\
&= A_3(a, b) \left[ \mathbf{q}^i \delta^{jk} + \mathbf{q}^j \delta^{ik} + \mathbf{q}^k \delta^{ij} - \frac{D+2}{D} \mathbf{q}^k \delta^{ij} \right] \\
&+ B_3(a, b) \left[ \mathbf{q}^i \mathbf{q}^j \mathbf{q}^k - \frac{1}{D} q^2 \mathbf{q}^k \delta^{ij} \right]. \tag{D.15}
\end{aligned}$$

# Bibliography

- [1] D. R. Phillips, Czech. J. Phys. **52**, B49 (2002), nucl-th/0203040.
- [2] B. R. Holstein, hep-ph/0010033.
- [3] P. F. Bedaque and U. van Kolck, Annu. Rev. Nucl. Part. Sci. **52**, 339 (2002).
- [4] V. Bernard, N. Kaiser and U.-G. Meißner, Int. J. Mod. Phys. **E 4**, 193 (1995); E. Epelbaum, Nucl. Phys. **A 737**, 43 (2004) and references therein.
- [5] H. Arenhövel and M. Sanzone, Few-Body Syst. Suppl. 3, 1 (1991).
- [6] R. Gilman and F. Gross, J. Phys. **G 28**, R37 (2002).
- [7] W. Fabian and H. Arenhövel, Nucl. Phys. **A 314**, 253 (1979).
- [8] H. Arenhövel, W. Leidemann and E. L. Tomusiak, nucl-th/0407053.
- [9] P. von Neumann-Cosel et al., Phys. Rev. Lett. **88**, 202304 (2002).
- [10] J. Schwinger, hectographed notes on nuclear physics, Harvard University 1947; G. F. Chew and M. L. Goldberger, Phys. Rev. 75, 1637 (1949); F. C. Barker and R. E. Peierls, Phys. Rev. 75, 3122 (1949); H. A. Bethe, Phys. Rev. **76**, 38 (1949); H. A. Bethe and C. Longmire, Phys. Rev. **77**, 647 (1950).
- [11] S. R. Beane et al., in (ed.) M. Shifman, At the frontier of particle physics, Vol.1 133, World Scientific, Singapore (2001), nucl-th/0008064.
- [12] J. M. B. Kellog et al., Phys. Rev. **55**, 318 (1939).
- [13] D. B. Kaplan, Nucl. Phys. **B 494**, 471 (1997).
- [14] D. B. Kaplan, M. J. Savage and M. B. Wise, Phys. Lett. **B 424**, 390 (1998).

- [15] D. B. Kaplan, M. J. Savage and M. B. Wise, Nucl. Phys. **B 534**, 329 (1998).
- [16] D. R. Phillips, G. Rupak and M. J. Savage, Phys. Lett. **B 473**, 209 (2000).
- [17] P. F. Bedaque and H. W. Griesshammer, Nucl. Phys. **A 671**, 357 (2000).
- [18] H. W. Griesshammer, Nucl. Phys. **A 744**, 192 (2004).
- [19] S. R. Beane and M. J. Savage, Nucl. Phys. **A 694**, 511 (2001).
- [20] P. F. Bedaque, G. Rupak, H. W. Griesshammer and H.-W. Hammer, Nucl. Phys. **A 714**, 589 (2003).
- [21] S. Ando and C. H. Hyun, nucl-th/0407103.
- [22] J.-W. Chen, G. Rupak and M. J. Savage, Nucl. Phys. **A 653**, 386 (1999).
- [23] H. P. Stapp, T. J. Ypsilantis and N. Metropolis, Phys. Rev. **105**, 302 (1957).
- [24] V. G. J. Stoks, R. A. M. Klomp, C. P. F. Terheggen and J. J. de Swart, Phys. Rev. **C 49**, 2950 (1994).
- [25] J.-W. Chen and M. J. Savage, Phys. Rev. **C 60**, 065205 (1999).
- [26] J.-W. Chen, G. Rupak and M. J. Savage, Phys. Lett. **B 464**, 1 (1999).
- [27] G. Rupak, Nucl. Phys. **A 678**, 405 (2000).
- [28] M. P. Peskin, D. V. Schroeder, An Introduction to Quantum Field Theory, Addison-Wesley, New York (1995).
- [29] A. E. Cox, S. A. R. Wynchank and C. H. Collie, Nucl. Phys. **74**, 497 (1965).
- [30] C. Itzykson and J.-B. Zuber, Quantum Field Theory, McGraw-Hill, New York (1980).
- [31] J. A. Grifols, E. Massó and S. Mohanty, Phys. Lett. **B 587**, 184 (2004).
- [32] L. H. Ryder, Quantum Field Theory, 2<sup>nd</sup> ed., Cambridge University Press, Cambridge (1996).
- [33] M. J. Savage and R. P. Springer, Nucl. Phys. **A 686**, 413 (2001).

- [34] P. Ramond, *Field Theory*, 2<sup>nd</sup> ed., Addison-Wesley, Redwood City (1989).
- [35] J.-W. Chen, X. Ji and Y. Li, nucl-th/0407019.
- [36] [http://qclam.ikp.physik.tu-darmstadt.de/eng/exp\\_deep.htm](http://qclam.ikp.physik.tu-darmstadt.de/eng/exp_deep.htm).
- [37] H. Arenhövel, private communication.
- [38] A. Shevchenko, private communication.
- [39] T. Tamae et al., *Phys. Rev. Lett.* **59**, 2919 (1987).
- [40] P. von Neumann-Cosel, private communication.
- [41] S. Fleming, T. Mehen and I. W. Stewart, *Nucl. Phys. A* **677**, 313 (2000).

# Danksagung

Hiermit möchte ich mich bei allen herzlich bedanken, die mich bei dieser Arbeit unterstützt haben, insbesondere bei

- \* Prof. Wolfram Weise dafür, dass er mir die Möglichkeit gegeben hat, meine Diplomarbeit an seinem Lehrstuhl durchzuführen, sowie für das Korrekturlesen dieser Arbeit.
- \* Dr. Harald Griefshammer, der mir dieses interessante Thema vorgeschlagen hat und mich mit großer Geduld und Hilfsbereitschaft hervorragend betreut hat.
- \* Prof. Hartmuth Arenhövel, der die Ergebnisse seiner Berechnungen zur Verfügung stellte, und damit wichtige Anhaltspunkte lieferte.
- \* Stefan Fritsch und Michael Thaler für die wertvolle Hilfe bei Computerproblemen.
- \* Tobias Gail und Robert Hildebrandt für viele hilfreiche Diskussionen.
- \* Ralph Bundschuh für das Korrekturlesen.
- \* allen Mitarbeitern am Lehrstuhl T39 für die freundliche Aufnahme, das gute Arbeitsklima und zahlreiche willkommene Abwechslungen (Schafkopfen, Filmabende, ...).
- \* meinen Eltern und Großeltern für die Unterstützung während des ganzen Studiums.